NASA Technical Memorandum 4302

Preliminary Subsonic Aerodynamic Model for Simulation Studies of the HL-20 Lifting Body

E. Bruce Jackson and Christopher I. Cruz
Langley Research Center
Hampton, Virginia

NASA
National Aeronautics and
Space Administration
Office of Management
Scientific and Technical
Information Program
1992

Summary

A nonlinear, six-degree-of-freedom aerodynamic model for an early version of the HL-20 lifting body is described and compared with wind tunnel data upon which it is based. Polynomial functions describing most of the aerodynamic parameters are given and tables of these functions are presented. Techniques used to arrive at these functions are described.

Basic aerodynamic coefficients were modeled as functions of angles of attack and sideslip with vehicle lateral symmetry assumed and compressibility (Mach) effects ignored. Control effectiveness was assumed to vary linearly with angle of deflection and was assumed to be invariant with angle of sideslip. Dynamic derivatives were obtained from predictive aerodynamic codes. Landing-gear and ground effects were scaled from Space Shuttle data.

The model described is provided to support pilot-in-the-loop simulation studies of the HL-20. By providing the data in tabular format, the model is suitable for the data interpolation architecture of many existing engineering simulation facilities. Because of the preliminary nature of the data, however, this model is not recommended for study of absolute performance of the HL-20.

Introduction

The HL-20 lifting body (fig. 1) has been designed as a component of the proposed personnel launch system (PLS). This vehicle would be launched into orbit by a booster rocket or carried within the payload bay of the Space Shuttle orbiter. The vehicle would then deorbit by using an on-board propulsion system and perform a nose-first reentry and horizontal, possibly unpowered, landing as described in reference 1.

The HL-20 lifting body has been designed to carry up to 10 people and very little cargo. New construction techniques will facilitate maintenance of the vehicle and permit rapid turnaround between landing and launching.

A lifting-body concept has been suggested for the PLS to provide sufficient cross-range capability to allow for a higher number of landing opportunities while keeping aerodynamic heating at acceptable levels during reentry.

This report describes a preliminary subsonic aerodynamic model of an early slab-wing version of the HL-20 vehicle with a maximum lift-to-drag ratio of 3.2. The model was developed to provide an early real-time simulation of the vehicle in the approach and landing phases of flight. The simulation was used from February to October of 1990 to support development of preliminary guidance algorithms, pilot displays, manual and automatic flight control systems, and evaluations of handling qualities and proposed configuration changes.

The model is based upon measurements of the aerodynamic characteristics of scaled models, except where noted. These measurements were obtained in the Langley 30- by 60-Foot Tunnel and in the Calspan 8-Foot Transonic Wind Tunnel at Mach numbers of 0.08 and 0.6, respectively.

The wind tunnel data, in original form, are unsuitable for use in piloted simulations for several reasons. Data obtained in different wind tunnels with different scale models of the same vehicle are not always consistent. In the HL-20 example, different sets of control-surface combinations were tested in the two tunnels. Fitting a smooth function through the wind tunnel data results in smooth derivatives of those data. The smooth derivatives are important in performing stability analyses.

This report outlines the technique used to blend force and moment data from the two wind tunnel facilities into a single aerodynamic model. Algorithms that were used for smoothing the wind tunnel data are referenced. The resulting mathematical descriptions of the aerodynamic functions are given. For comparison purposes, plots of wind tunnel data and these model data are shown. Landing-gear, ground effects, and dynamic derivatives are given in tabular format.

Most of the functions of nondimensional aerodynamic coefficients functions documented in the appendix of this report are described both mathematically and in tabular format. These tables of coefficients describe the variation of vehicle aerodynamic characteristics with respect to angles of attack and sideslip and, in some cases, height above ground and landing-gear position. The values given in these tables are equivalent to the values obtained by using the equations; however, because many real-time simulation facilities presently use function-table lookup techniques, tables are provided.

In developing this model, compressibility (Mach) effects were ignored. Lateral symmetry was assumed. Data for the vehicle with no control-surface deflection (hereinafter referred to as *basic*) were assumed to vary with angles of attack and sideslip. Control-surface effects were assumed to vary nonlinearly with angle of attack and linearly with angle of deflection. No dependence upon angle of sideslip for control effects was modeled.

Although general trends in the dynamic characteristics of the HL-20 vehicle should be adequately represented by this model, the model is not intended for obtaining quantitative values of the performance of the HL-20. Predictions of aircraft performance should be made after more complete aerodynamic data are available.

Dynamic derivatives were obtained from predictive aerodynamic codes. Landing-gear and ground effects were scaled from Space Shuttle data.

Symbols

All forces and moments are referred to the body axis system. See figures 2 and 3 for body and axis sign conventions and control-surface nomenclature, respectively.

b	reference span, ft
$\bar{c}$	reference length, ft
C_A	axial-force coefficient (+ indicates force in aft direction)
C_l	rolling-moment coefficient
C_m	pitching-moment coefficient
C_N	normal-force coefficient (+ indicates force in up direction)
C_n	yawing-moment coefficient
C_X	axial-force coefficient (+ indicates force in forward direction)
C_Y	side-force coefficient
C_Z	normal-force coefficient (+ indicates force in down direction)
F_X, F_Y, F_Z	aerodynamic force in X, Y, and Z direction, respectively
h	height of center of gravity above ground, ft
M	Mach number
M_X, M_Y, M_Z	moment about X, Y, and Z axis, respectively
$\mathbf{P}_j$	curve-fit polynomial coefficient vector
p, q, r	roll, pitch, and yaw rate, respectively
S	reference area, ft^2
α	angle of attack, deg (+ indicates aircraft nose up)
β	angle of sideslip, deg (+ indicates aircraft nose left)
δ_a	aileron deflection, deg (+ indicates right wing down)
δ_e	elevator deflection, deg (+ indicates trailing edge down)
δ_{f+}	positive flap deflection, deg (+ indicates trailing edge down)
δ_{f-}	negative flap deflection, deg (+ indicates trailing edge down)
$\delta_{bf_{ll}}$	lower left body-flap deflection, deg (+ indicates trailing edge down)
$\delta_{bf_{lr}}$	lower right body-flap deflection, deg (+ indicates trailing edge down)
$\delta_{bf_{ul}}$	upper left body-flap deflection, deg (+ indicates trailing edge down)
$\delta_{bf_{ur}}$	upper right body-flap deflection, deg (+ indicates trailing edge down)
δ_{lg}	landing-gear position, deg (0 = up, 98 = down)
δ_r	rudder deflection, deg (+ indicates trailing edge left)
δ_{wf_l}	left wing-flap deflection, deg (+ indicates trailing edge down)
δ_{wf_r}	right wing-flap deflection, deg (+ indicates trailing edge down)
$\delta_{\Delta f}$	differential body-flap deflection, deg (+ indicates right wing down)

Subscripts:

o	basic configuration
GE	ground effect

Abbreviations:

ANL	aircraft nose left
ANR	aircraft nose right
ANU	aircraft nose up
RWD	right wing down
TED	trailing edge down
TEL	trailing edge left
TEU	trailing edge up

Model Description

Origin of Data

Most data for this model originated from wind tunnel tests. Low-speed ($M = 0.08$) data were obtained in the Langley 30- by 60-Foot Tunnel; higher

speed ($M = 0.6$) data were taken in the Calspan 8-Foot Transonic Tunnel.

Langley 30- by 60-Foot Tunnel. A 4.92-ft model was tested in the Langley 30- by 60-Foot Tunnel (Langley tunnel) in a series of runs conducted at $M = 0.08$ (ref. 2). These runs covered a range of angle of attack from 0° to 55° and a range of angle of sideslip from −10° to 10°. Various configurations of control-surface deflections of symmetric body flaps, antisymmetric body flaps, antisymmetric wing flaps, and all-movable rudder deflections of up to 30° were tested; only a few configurations with a single body flap deflected were tested; and no configurations with single wing flaps or symmetric wing flaps were tested in these early wind tunnel runs. A summary of the Langley tunnel runs used in the development of this model is given in table I.

Calspan 8-Foot Transonic Tunnel. A 20.63-in. model was tested in the Calspan 8-Foot Transonic Tunnel (Calspan tunnel) at $M = 0.6$ (ref. 3). The tests covered a range of angle of attack from −10° to 30° and a range of angle of sideslip from −10° to 10°. Control deflections of symmetric and antisymmetric body flaps, symmetric and antisymmetric wing flaps, and the all-movable rudder were tested. No deflections of single surface body or wing flap were tested. A summary of the configurations tested in the Calspan tunnel is given in table II.

Ground proximity and landing-gear effects. Ground effects and landing-gear effects were based on Space Shuttle data given in reference 4. These data were scaled according to ratios between the HL-20 and the Space Shuttle orbiter reference lengths and areas.

Dynamic derivatives. The dynamic derivative coefficients ($C_{m_q}, C_{l_p}, C_{l_r}, C_{n_p}$, and C_{n_r}) were predicted with software called the Aerodynamic Preliminary Analysis System (APAS). The use of this software is described in references 5 and 6.

Sign Conventions

Figure 2 illustrates the body and axis-sign conventions used for the aerodynamic coefficient tables. Figure 3 shows the control-surface nomenclature and sign convention used to describe aerodynamic surface deflections.

Computation of Aerodynamic Forces and Moments

Input variables. For the convenience of the reader, table III summarizes the independent variables (input quantities) required for the HL-20 aerodynamic model.

Combination of surfaces. Because most of the wind tunnel tests were conducted by using combinations of control-surface deflections, individual body-flap and wing-flap surface contributions were difficult to determine. For this reason, the aerodynamic functions documented in this report are based upon linear combinations of symmetric and differential surface deflections. These combinations are defined in figure 4.

Force and moment equations. A conventional "coefficient build-up" method is used in the formulation of the aerodynamic model, in which the vehicle aerodynamic coefficients for the basic configuration, modeled as functions of angles of attack and sideslip, are modified by incremental coefficients that represent the effect of control-surface positions, landing-gear extension, and ground proximity effects. Moment coefficients are also modified by rotational effects (dynamic derivatives). In general, the incremental coefficients are functions of angle of attack. Landing-gear effects are functions of angle of attack and landing-gear deflection angle. Ground effects are functions of angle of attack and normalized height above ground.

The following six equations define how the functions described in the appendix are combined to yield the six total aerodynamic coefficients:

$$C_X = C_{X,o}(\alpha,\beta) + C_{X_{\delta_e}}(\alpha)\,\delta_e + C_{X_{|\delta_a|}}(\alpha)\,|\delta_a| + C_{X_{\delta_{f+}}}(\alpha)\,\delta_{f+} + C_{X_{\delta_{f-}}}(\alpha)\,\delta_{f-}$$
$$+ C_{X_{|\delta_{\Delta f}|}}(\alpha)\,|\delta_{\Delta f}| + C_{X_{|\delta_r|}}(\alpha)\,|\delta_r| + C_{X,\delta_{lg}}(\alpha,\delta_{lg}) + C_{X,GE}\left(\alpha,\frac{h}{b}\right) \tag{1}$$

$$C_Y = C_{Y_\beta}\beta + C_{Y_{\delta_a}}(\alpha)\,\delta_a + C_{Y_{\delta_{\Delta f}}}(\alpha)\,\delta_{\Delta f} + C_{Y_{\delta_r}}(\alpha)\,\delta_r \tag{2}$$

$$C_Z = C_{Z,o}(\alpha,\beta) + C_{Z_{\delta_e}}(\alpha)\,\delta_e + C_{Z_{\delta_{f+}}}(\alpha)\,\delta_{f+} + C_{Z_{\delta_{f-}}}(\alpha)\,\delta_{f-} + C_{Z,\delta_{lg}}(\alpha,\delta_{lg})$$

$$+ C_{Z,GE}\left(\alpha, \frac{h}{b}\right) \tag{3}$$

$$C_l = C_{l_\beta}\beta + C_{l_{\delta_a}}(\alpha)\,\delta_a + C_{l_{\delta_{\Delta f}}}(\alpha)\,\delta_{\Delta f} + C_{l_{\delta_r}}(\alpha)\,\delta_r + C_{l_p}(\alpha)\,\frac{pb}{2V} + C_{l_r}(\alpha)\,\frac{rb}{2V} \tag{4}$$

$$C_m = C_{m,o}(\alpha,\beta) + C_{m_{\delta_e}}(\alpha)\,\delta_e + C_{m_{|\delta_a|}}(\alpha)\,|\delta_a| + C_{m_{\delta_{f+}}}(\alpha)\,\delta_{f+} + C_{m_{\delta_{f-}}}(\alpha)\,\delta_{f-}$$

$$+ C_{m_q}(\alpha)\,\frac{q\bar{c}}{2V} + C_{m,\delta_{lg}}(\alpha,\delta_{lg}) + C_{m,GE}\left(\alpha, \frac{h}{b}\right) \tag{5}$$

$$C_n = C_{n,o}(\alpha,\beta) + C_{n_{\delta_a}}(\alpha)\,\delta_a + C_{n_{\delta_{\Delta f}}}(\alpha)\,\delta_{\Delta f} + C_{n_{\delta_r}}(\alpha)\,\delta_r$$

$$+ C_{n_p}(\alpha)\,\frac{pb}{2V} + C_{n_r}(\alpha)\,\frac{rb}{2V} \tag{6}$$

These nondimensional coefficients are then scaled to provide dimensional forces (F_i) and moments (M_i), as follows:

$$F_X = \bar{q}SC_X \tag{7}$$

$$F_Y = \bar{q}SC_Y \tag{8}$$

$$F_Z = \bar{q}SC_Z \tag{9}$$

$$M_X = \bar{q}SbC_l \tag{10}$$

$$M_Y = \bar{q}S\bar{c}C_m \tag{11}$$

$$M_Z = \bar{q}SbC_n \tag{12}$$

Reference values. The moment reference point for all wind tunnel tests was located at 54 percent of body length along the X body axis, as measured from the nose. Table IV provides the reference values for the nondimensionalizing constants S, $\bar{c}$, and b.

Output variables. Table V summarizes the output quantities calculated by equations (7) through (12).

Development of Model

Measurement axes. The aerodynamic coefficient data were measured about the normal, axial, and sideward axes (N, A, Y) in both wind tunnels (fig. 2). These axes were retained for all data reduction steps described in this report. The tables given in the appendix provide these same data in body X, Y, Z axes as this transformation is trivial ($C_X = -C_A, C_Z = -C_N, C_Y = C_Y$) and the X, Y, Z axes are the conventional axes for real-time flight simulation.

General procedure. The approach taken to describe the aerodynamics of the HL-20 vehicle included developing, wherever possible, a polynomial description of each aerodynamic function. This ensured a smooth, continuous function and removed some of the scatter in the wind tunnel data. Also, measurements of the same coefficient from the two different wind tunnels were usually taken at dissimilar values of angles of attack and sideslip, and some means of reconciling the two dissimilar sets of raw data were needed. This curve-fitting procedure was unnecessary for some coefficients, and those instances are mentioned subsequently.

The curve-fitting method used to generate the parameters for each polynomial description was an unweighted least-squares algorithm, as implemented in the matrix left division operation of the Integrated Systems MATRIX_x software product (ref. 7).

Lateral symmetry of the model was assumed. Thus, longitudinal data (N, m, A measurements) were reflected about the axis of zero angle of sideslip before curve fitting, as shown in figure 5(a). Lateral-directional data (l, Y, n measurements) were reflected about the origin before obtaining curve fits to ensure that the resulting curve fits would pass through a value of zero at an angle of sideslip of 0°. Figure 5(b) illustrates this procedure.

A three-dimensional polynomial surface was fit through the longitudinal wind tunnel measurements of the vehicle in the basic configuration (in which control surfaces were undeflected), as a function of angle of attack and angle of sideslip $\left(C_{N,o} = C_{N,o}(\alpha,\beta),\ C_{m,o} = C_{m,o}(\alpha,\beta),\ \text{and}\ C_{A,o} = C_{A,o}(\alpha,\beta)\right)$.

The lateral coefficients C_Y and C_l for the basic configuration were found to vary linearly with angle of sideslip irrespective of angle of attack; they were therefore modeled as scalar sideslip derivative values (C_{Y_β} and C_{l_β}, respectively).

Yawing moment ($C_{n,o}$) for the basic configuration did not lend itself to polynomial surface fitting. It was modeled by using engineering judgement based upon the available data as a function of sideslip for each value of angle of attack.

To generate the incremental effects of control-surface deflections, the difference between deflected control-surface and nondeflected control-surface data for that wind tunnel model was calculated prior to smoothing. (A linear interpolation in angle of attack between the data points for the basic configuration was necessary before performing the subtraction.) This calculation yielded an incremental coefficient for each control deflection. The resulting incremental coefficient was then divided by the control-surface deflection angle. This resulted in a set of derivative coefficients for each measured deflection. A polynomial curve was then fit by using a least-squares algorithm simultaneously through all derivative data points for a given control-surface combination. This curve was fourth-order in angle of attack. Figure 6 illustrates this process for a general coefficient C, an incremental coefficient ΔC, and a derivative coefficient C_δ.

Tabular data were then generated as a function of angles of attack and sideslip by using the polynomial descriptions of the clean and derivative functions (appendix). During this process, the change of axes from N, A, Y to X, Y, Z body axes was performed. Because the aerodynamic functions are continuous (except for $C_{n,o}$), it was possible to tailor the distribution of the function-table indices to better describe the functions by concentrating breakpoints in areas of interest. For example, a higher density of angle of sideslip was chosen on either side of zero angle of sideslip because most flight occurs at relatively small angles of sideslip. Also, the density of angle-of-attack breakpoints was increased near the inflection point on the pitching-moment curve, near an angle of attack of 25°, to better model this aerodynamically interesting area.

Data for basic configuration. The data for the basic configuration from the Calspan tunnel (runs 49–54 in table II) were used to generate a sixth-order polynomial curve fit by using a least-squares algorithm as a function of angle of attack (α) and absolute value of angle of sideslip ($|\beta|$). Equation (13) gives the general matrix equation used to generate the curve fits, and equation (14) contains the values of the parameters of the $\mathbf{P}_o$ matrix. These equations are

$$\left[C_{N,o} \quad C_{m,o} \quad C_{A,o}\right] = \left[1 \quad \alpha \quad \alpha^2 \quad \alpha^3 \quad \alpha^4 \quad \alpha^5 \quad \alpha^6 \quad |\beta| \quad \beta^2 \quad |\beta^3| \quad \beta^4 \quad \alpha|\beta|\right] \quad \mathbf{P}_o \tag{13}$$

where

$$\mathbf{P}_o = \begin{bmatrix} -9.025 \times 10^{-2} & 2.632 \times 10^{-2} & 7.362 \times 10^{-2} \\ 4.070 \times 10^{-2} & -2.226 \times 10^{-3} & -2.560 \times 10^{-4} \\ 3.094 \times 10^{-5} & -1.859 \times 10^{-5} & -2.208 \times 10^{-4} \\ 1.564 \times 10^{-5} & 6.001 \times 10^{-7} & -2.262 \times 10^{-6} \\ -1.386 \times 10^{-6} & 1.828 \times 10^{-7} & 2.966 \times 10^{-7} \\ 2.545 \times 10^{-8} & -9.733 \times 10^{-9} & -3.640 \times 10^{-9} \\ -1.189 \times 10^{-10} & 1.710 \times 10^{-10} & 9.388 \times 10^{-12} \\ 2.564 \times 10^{-3} & -5.233 \times 10^{-4} & -5.299 \times 10^{-4} \\ 8.501 \times 10^{-4} & 6.795 \times 10^{-5} & -4.709 \times 10^{-4} \\ -1.156 \times 10^{-4} & -1.993 \times 10^{-5} & 8.572 \times 10^{-5} \\ 3.416 \times 10^{-6} & 1.341 \times 10^{-6} & -4.199 \times 10^{-6} \\ -4.862 \times 10^{-4} & 6.061 \times 10^{-5} & 1.295 \times 10^{-4} \end{bmatrix} \tag{14}$$

Figures 7 through 9 depict the wind tunnel measurements and show comparisons with the numerically generated curve fits. The Langley tunnel data are shown for comparison with the curve fits and the Calspan tunnel data. In each figure, the first two parts, (a) and (b), show the curve fits and the wind tunnel data. The next part, (c), shows the surfaces plotted in three dimensions with constant spacing between α and β grid points. The final part, (d), shows the same surfaces drawn with the α and β grid point sets used to generate the tables found in the appendix.

As might be anticipated, the lateral-directional components are zero at $\beta = 0°$ for the basic configuration. The side-force and roll stability derivatives C_{Y_β} and C_{l_β} were found to be virtually constant with angle of sideslip and constant at most angles of attack with values given in the following equations:

$$C_{Y_\beta} = -0.01242 \text{ per deg} \tag{15}$$

$$C_{l_\beta} = -0.00787 \text{ per deg} \tag{16}$$

Figures 10 and 11 show the validity of this approximation. These values were generated from an examination of Calspan tunnel runs 49–54 in table II.

Yawing-moment coefficient for the basic configuration $C_{n,o}$ was neither constant nor analytic in nature, and consequently a function table was derived by inspection of available wind tunnel data as a function of angles of attack and sideslip. The data were adjusted to pass through zero at $\beta = 0°$. Figure 12 illustrates the wind tunnel $C_{n,o}$ data points (from Langley tunnel runs 2–11 in table I, and Calspan tunnel runs 49–54 in table II) and the corresponding aerodynamic model function.

Symmetric wing flaps (elevator). Whereas the Calspan tunnel runs included symmetric deflections of wing flaps, the initial Langley tunnel runs did not include symmetric wing-flap configurations. Thus, the contribution of symmetric wing flaps to longitudinal aerodynamic characteristics was based entirely on the tests at $M = 0.6$ (Calspan tunnel runs 198, 210, and 216). Symmetric deflection angles of 5°, −5°, and −10° were tested. The equation for symmetric wing-flap contributions is given by

$$\begin{bmatrix} C_{N_{\delta_e}} & C_{m_{\delta_e}} & C_{A_{\delta_e}} \end{bmatrix} = \begin{bmatrix} 1 & \alpha & \alpha^2 & \alpha^3 & \alpha^4 \end{bmatrix} \mathbf{P}_{\delta_e} \tag{17}$$

where values of $\mathbf{P}_{\delta_e}$ are as follows:

$$\mathbf{P}_{\delta_e} = \begin{bmatrix} 5.140 \times 10^{-3} & -1.903 \times 10^{-3} & -1.854 \times 10^{-4} \\ 3.683 \times 10^{-5} & -1.593 \times 10^{-5} & 2.830 \times 10^{-6} \\ -6.092 \times 10^{-6} & 2.611 \times 10^{-6} & -6.966 \times 10^{-7} \\ 2.818 \times 10^{-9} & 5.116 \times 10^{-8} & 1.323 \times 10^{-7} \\ -2.459 \times 10^{-9} & -1.626 \times 10^{-9} & -2.758 \times 10^{-9} \end{bmatrix} \tag{18}$$

Figure 13 shows the effect of symmetric wing flaps per degree of deflection on the normal-force, axial-force, and pitching-moment coefficients, as well as the corresponding curve fit.

Differential wing flaps (ailerons). The contribution of differential wing flaps to HL-20 aerodynamic characteristics was based entirely on Langley tunnel tests at $M = 0.08$ (runs 16, 17, 18, and 19, corresponding to 15°, 30°, −15°, and −30°, respectively). Because the Langley tunnel tests did not include negative angles of attack, the curve fits for these coefficients were held constant at the value for angle of attack of 0° for lower values. The equation for differential elevon contributions is given by

$$\begin{bmatrix} C_{N_{|\delta_a|}} & C_{m_{|\delta_a|}} & C_{A_{|\delta_a|}} & C_{Y_{\delta_a}} & C_{n_{\delta_a}} & C_{l_{\delta_a}} \end{bmatrix} = \begin{bmatrix} 1 & \alpha & \alpha^2 & \alpha^3 & \alpha^4 \end{bmatrix} \mathbf{P}_{\delta_a} \tag{19}$$

where $\mathbf{P}_{\delta_a}$ values are given as follows:

$$\mathbf{P}_{\delta_a} = \begin{bmatrix} -2.503 \times 10^{-4} & 1.471 \times 10^{-4} & 9.776 \times 10^{-4} & 3.357 \times 10^{-3} & -2.769 \times 10^{-3} & 2.538 \times 10^{-3} \\ 4.987 \times 10^{-5} & 4.673 \times 10^{-5} & -2.703 \times 10^{-5} & -1.661 \times 10^{-5} & -4.377 \times 10^{-5} & 1.963 \times 10^{-5} \\ -2.274 \times 10^{-6} & -8.282 \times 10^{-6} & -8.303 \times 10^{-6} & -3.280 \times 10^{-6} & 9.952 \times 10^{-6} & -3.725 \times 10^{-6} \\ -1.407 \times 10^{-7} & 4.891 \times 10^{-7} & 6.645 \times 10^{-7} & 5.526 \times 10^{-8} & -3.642 \times 10^{-7} & 3.539 \times 10^{-8} \\ 5.135 \times 10^{-9} & -8.742 \times 10^{-9} & -1.273 \times 10^{-8} & -3.269 \times 10^{-10} & 4.692 \times 10^{-9} & -1.778 \times 10^{-10} \end{bmatrix} \tag{20}$$

Figure 14 shows the effect of differential wing flaps per degree of deflection on the force and moment coefficients, as well as the corresponding curve fit.

Because the contribution of $C_{N_{|\delta_a|}}$ was small compared to normal-force coefficient $C_{N,o}$, $C_{N_{|\delta_a|}}$ for the basic configuration was set to zero in the model and does not appear in the data tables found in the appendix.

Positive body flaps. The contributions of symmetric, positive (lower) body-flap deflections to HL-20 aerodynamic characteristics were based on Langley tunnel tests (run 15 (10°) and run 34 (30°)) and on Calspan tunnel tests (run 192 (10°)). The equation for positive body-flap contributions is given by

$$\begin{bmatrix} C_{N_{\delta_{f+}}} & C_{m_{\delta_{f+}}} & C_{A_{\delta_{f+}}} \end{bmatrix} = \begin{bmatrix} 1 & \alpha^2 & \alpha^4 \end{bmatrix} \mathbf{P}_{\delta_{f+}} \tag{21}$$

where values of $\mathbf{P}_{\delta_{f+}}$ are given as follows:

$$\mathbf{P}_{\delta_{f+}} = \begin{bmatrix} 3.779 \times 10^{-3} & -9.896 \times 10^{-4} & 1.310 \times 10^{-4} \\ -7.017 \times 10^{-7} & -1.494 \times 10^{-9} & 1.565 \times 10^{-6} \\ 1.400 \times 10^{-10} & 6.303 \times 10^{-11} & -1.542 \times 10^{-9} \end{bmatrix} \tag{22}$$

Figure 15 shows the effect of positive body flaps per deg of deflection on axial-force, normal-force, and pitching-moment coefficients, as well as the corresponding curve fit.

Negative body flaps. The contribution of symmetric negative (upper) body-flap deflections to HL-20 aerodynamic characteristics was based on Langley tunnel runs 12, 13, and 35, and on Calspan tunnel run 180, at flap settings of −5°, −10°, −30°, and −10°, respectively. Note that the test at −30° did not include the

vertical all-movable rudder; this effect is considered to be negligible compared with the contributions of the negative flaps. The equation for negative body-flap contributions is given by

$$\begin{bmatrix} C_{N_{\delta_{f-}}} & C_{m_{\delta_{f-}}} & C_{A_{\delta_{f-}}} \end{bmatrix} = \begin{bmatrix} 1 & \alpha & \alpha^2 & \alpha^3 & \alpha^4 \end{bmatrix} \mathbf{P}_{\delta_{f-}} \tag{23}$$

where values of $\mathbf{P}_{\delta_{f-}}$ are given as follows:

$$\mathbf{P}_{\delta_{f-}} = \begin{bmatrix} 3.711 \times 10^{-3} & -1.086 \times 10^{-3} & -4.415 \times 10^{-4} \\ -3.547 \times 10^{-5} & 1.570 \times 10^{-5} & -4.056 \times 10^{-6} \\ -2.706 \times 10^{-6} & 4.174 \times 10^{-7} & -4.657 \times 10^{-7} \\ 2.938 \times 10^{-7} & -1.133 \times 10^{-7} & 0 \\ -5.552 \times 10^{-9} & 2.723 \times 10^{-9} & 0 \end{bmatrix} \tag{24}$$

Figure 16 shows the effect of negative body flaps per degree of deflection on axial-force, normal-force, and pitching-moment coefficients, as well as the corresponding curve fit.

Differential body flaps. The contribution of differential body flaps to HL-20 aerodynamic characteristics was based on Langley tunnel runs 22 through 26, which included data taken at angles of sideslip from $-10°$ to $10°$, with $-30°$ differential body flap ($\delta_{bf_{ul}} = -30°$, $\delta_{bf_{lr}} = 30°$), and Calspan tunnel run 186, with $-10°$ differential body flap. The differential body flaps had very little effect on normal force or pitching moment, therefore, these effects were not modeled. The equation for differential body-flap contributions is given by

$$\begin{bmatrix} C_{A_{|\delta_{\Delta f}|}} & C_{Y_{\delta_{\Delta f}}} & C_{n_{\delta_{\Delta f}}} & C_{l_{\delta_{\Delta f}}} \end{bmatrix} = \begin{bmatrix} 1 & \alpha & \alpha^2 & \alpha^3 & \alpha^4 \end{bmatrix} \mathbf{P}_{\delta_{\Delta f}} \tag{25}$$

where values of $\mathbf{P}_{\delta_{\Delta f}}$ are given as follows:

$$\mathbf{P}_{\delta_{\Delta f}} = \begin{bmatrix} -6.043 \times 10^{-4} & 2.672 \times 10^{-5} & -5.107 \times 10^{-5} & 7.453 \times 10^{-4} \\ -1.858 \times 10^{-5} & -3.849 \times 10^{-5} & 1.108 \times 10^{-5} & -1.811 \times 10^{-5} \\ 8.000 \times 10^{-7} & 4.564 \times 10^{-7} & -1.547 \times 10^{-8} & -1.264 \times 10^{-7} \\ -4.845 \times 10^{-8} & 1.798 \times 10^{-8} & -1.552 \times 10^{-8} & 9.972 \times 10^{-8} \\ 1.360 \times 10^{-9} & -4.099 \times 10^{-10} & 1.413 \times 10^{-10} & -2.684 \times 10^{-9} \end{bmatrix} \tag{26}$$

Figure 17 shows the effect of differential body flaps per degree of deflection on the other force and moment coefficients, as well as the corresponding curve fits. The large amount of scatter apparent in these plots was due to sideslip, which was not modelled in the curve fit.

All-movable rudder. The contribution of the all-movable rudder to HL-20 aerodynamic characteristics was based on Langley tunnel runs 28 and 29, corresponding to 15° and 30° of the all-movable rudder. Because the Langley tunnel did not include negative angles of attack, the curve fits for these coefficients were held constant at the value for $\alpha = 0°$. The equation for all-movable rudder contributions is given by

$$\begin{bmatrix} C_{N_{|\delta_r|}} & C_{m_{|\delta_r|}} & C_{A_{|\delta_r|}} & C_{Y_{\delta_r}} & C_{n_{\delta_r}} & C_{l_{\delta_r}} \end{bmatrix} = \begin{bmatrix} 1 & \alpha & \alpha^2 & \alpha^3 & \alpha^4 \end{bmatrix} \mathbf{P}_{\delta_r} \tag{27}$$

where values of $\mathbf{P}_{\delta_r}$ are given as follows:

$$\mathbf{P}_{\delta_r} = \begin{bmatrix} 5.173 \times 10^{-4} & -5.116 \times 10^{-5} & 5.812 \times 10^{-4} & 1.855 \times 10^{-3} & -1.278 \times 10^{-3} & 2.260 \times 10^{-4} \\ 7.359 \times 10^{-5} & -1.516 \times 10^{-5} & 1.410 \times 10^{-5} & 1.128 \times 10^{-5} & 1.320 \times 10^{-5} & -1.299 \times 10^{-5} \\ -8.270 \times 10^{-7} & 1.729 \times 10^{-6} & -2.585 \times 10^{-6} & 6.069 \times 10^{-6} & -4.720 \times 10^{-6} & 5.565 \times 10^{-6} \\ -6.034 \times 10^{-7} & -2.481 \times 10^{-8} & 3.051 \times 10^{-7} & -1.780 \times 10^{-7} & 2.371 \times 10^{-7} & -3.382 \times 10^{-7} \\ 2.016 \times 10^{-8} & -7.867 \times 10^{-10} & -8.161 \times 10^{-9} & -1.886 \times 10^{-12} & -3.340 \times 10^{-9} & 6.461 \times 10^{-9} \end{bmatrix} \tag{28}$$

Figure 18 shows the effect of the all-movable rudder per degree of deflection on each of the force and moment coefficients, as well as the corresponding curve fits.

Because the contributions of $C_{N_{|\delta_r|}}$ and $C_{m_{|\delta_r|}}$ are small, they are set to zero in the model and do not appear in the data tables found in the appendix.

Dynamic derivatives. The five dynamic derivative coefficients used in this model (C_{m_q}, C_{l_p}, C_{l_r}, C_{n_p}, and C_{n_r}) were generated with APAS. (See refs. 5 and 6.) The method by which these data were generated is described in reference 1. Figure 19 shows a plot of these coefficients as a function of angle of attack.

Landing-gear effects. The aerodynamic contributions of landing gear were obtained from Space Shuttle aerodynamic models and scaled for a preliminary version of this vehicle, based upon relative reference lengths and areas. The original data from which these values were derived are given in reference 4. Reference 2 provides examples of the calculations used in developing these values. The lateral-directional effects of landing gear are not modeled because of the relatively small effect of these values and the uncertainty of the final landing-gear and gear-door configuration.

The landing-gear effects are scheduled by angle of attack and angle of gear extension, where 0° corresponds to gear fully retracted and 98° represents gear fully extended. Figure 20 presents these coefficients ($C_{X,\delta_{lg}}, C_{m,\delta_{lg}}$, and $C_{Z,\delta_{lg}}$) in graphic form.

Ground effects. In a manner similar to landing-gear effects, the ground effects data were scaled from Space Shuttle data, as a first approximation to HL-20 ground effects. Again, the lateral-directional derivatives were not included because of their relatively small contribution.

Although the reference point used in calculating height above the runway in the Space Shuttle data is the elevon hinge line, the HL-20 reference point is the aerodynamic reference point (54 percent of body length). This point was chosen to partially compensate for the anticipated lesser effect of ground proximity for the HL-20, compared with the Space Shuttle orbiter, owing to the difference between the position of the wings of the Space Shuttle and the canted winglets of the HL-20.

The ground effects data were scheduled by the ratio of altitude (of the reference point) to the span of the vehicle (given as h/b) and angle of attack. Figure 21 shows these effects graphically.

Concluding Remarks

This study was undertaken to develop an aerodynamic model of the HL-20 lifting-body vehicle suitable for preliminary control-system design efforts and studies of the subsonic flight and landing characteristics in a real-time piloted simulation. This report documents the process whereby limited wind tunnel and predicted aerodynamic data were converted into a format suitable for real-time simulation. The resulting model is based upon data obtained in two different wind tunnels with two different test models, scaled Space Shuttle data, and predicted dynamic characteristics from the Aerodynamic Preliminary Analysis System software. A least-squares fit was used to combine and smooth the data from the two wind tunnels. Comparison plots between the original wind tunnel data and the fitted polynomial curves are given. Polynomial descriptions of the resulting curves are given as well as tabular listings of all aerodynamic functions.

Several simplifications were made in the development of this model of the HL-20 aerodynamics. For the most part, these simplifications were made because of the scarcity of wind tunnel data at this early stage in the definition of the vehicle. Simplifications include the omission of compressibility (Mach) effects, assumption of linear control-surface effects with deflection, and no variation in control effects with angle of sideslip.

The linear control effects simplification was mandated by the limited amount of control effects wind tunnel data. This simplification will not invalidate initial control power estimates and control configuration decisions; however, when more data are available, flight control-system designs will need to be revisited to allow for minor nonlinearities in control effects.

The reader is cautioned against using data contained herein to make quantitative predictions of the performance of the HL-20, owing to the preliminary and limited nature of the data used to generate this model. This model is intended to support qualitative evaluations of the flight characteristics of the HL-20.

NASA Langley Research Center
Hampton, VA 23681-0001
June 24, 1992

References

1. Naftel, J. C.; Powell, R. W.; and Talay, T. A.: Ascent, Abort, and Entry Capability Assessment of a Space Station Rescue and Personnel/Logistics Vehicle. AIAA-89-0635, Jan. 1989.

2. Cruz, Christopher I.; Ware, George M.; Grafton, Sue B.; Woods, William C.; and Young, James C.: *Aerodynamic Characteristics of a Proposed Personnel Launch System (PLS) Lifting-Body Configuration at Mach Numbers From 0.05 to 20.3.* NASA TM-101641, 1989.

3. Ware, George M.: *Transonic Aerodynamic Characteristics of a Proposed Assured Crew Return Capability (ACRC) Lifting-Body Configuration.* NASA TM-4117, 1989.

4. *Aerodynamic Design Data Book. Volume 1: Orbiter Vehicle.* NASA CR-160386, 1978.

5. Bonner, E.; Clever, W.; and Dunn, K.: *Aerodynamic Preliminary Analysis System II. Part I—Theory.* NASA CR-182076, 1991.

6. Sova, G.; and Divan, P.: *Aerodynamic Preliminary Analysis System II. Part II—User's Manual.* NASA CR-182077, 1991.

7. *$MATRIX_x$ Core, Edition 7.* MDG014-010, Integrated Systems Inc., Jan. 1990.

Table I. Langley 30- by 60-Foot Tunnel Test Matrix at $M = 0.08$ for 4.92-ft Model

[From ref. 2]

Run	α, deg	β, deg	δ_{wf_l}, deg	δ_{wf_r}, deg	δ_r, deg	$\delta_{bf_{ul}}$, deg	$\delta_{bf_{ll}}$, deg	$\delta_{bf_{ur}}$, deg	$\delta_{bf_{lr}}$, deg
2	(a)	−10	0	0	0	0	0	0	0
3	↓	−5	↓	↓	↓	↓	↓	↓	↓
4	↓	−2	↓	↓	↓	↓	↓	↓	↓
5	↓	0	↓	↓	↓	↓	↓	↓	↓
6	↓	2	↓	↓	↓	↓	↓	↓	↓
7	↓	5	↓	↓	↓	↓	↓	↓	↓
8	↓	10	↓	↓	↓	↓	↓	↓	↓
9	12	(b)	↓	↓	↓	↓	↓	↓	↓
10	14	(b)	↓	↓	↓	↓	↓	↓	↓
11	16	(b)	↓	↓	↓	↓	↓	↓	↓
12	(a)	0	↓	↓	↓	↓	−5	↓	−5
13	↓	↓	↓	↓	↓	↓	−10	↓	−10
15	↓	↓	↓	↓	↓	10	0	10	0
16	↓	↓	15	−15	↓	0	↓	0	↓
17	↓	↓	30	−30	↓	↓	↓	↓	↓
18	↓	↓	−15	15	↓	↓	↓	↓	↓
19	↓	↓	−30	30	↓	↓	↓	↓	↓
22	↓	−10	0	0	↓	↓	−30	30	↓
23	↓	−5	↓	↓	↓	↓	↓	↓	↓
24	↓	0	↓	↓	↓	↓	↓	↓	↓
25	↓	5	↓	↓	↓	↓	↓	↓	↓
26	↓	10	↓	↓	↓	↓	↓	↓	↓
28	↓	0	↓	↓	15	↓	0	0	↓
29	↓	↓	↓	↓	30	↓	↓	0	↓
34	↓	↓	↓	↓	0	30	↓	30	↓
35	↓	↓	↓	↓	Off	0	−30		−30

[a]Angle-of-attack sweep, 0°–55° by 5° increments, except 10°–20° by 2° increments.
[b]Angle-of-sideslip sweep, −10°–10° by 2° increments.

Table II. Calspan 8-Foot Transonic Tunnel Test Matrix at $M = 0.6$ for 20.63-in. Model

[From ref. 3]

Run	α, deg	β, deg	δ_{wf_l}, deg	δ_{wf_r}, deg	δ_r, deg	$\delta_{bf_{ul}}$, deg	$\delta_{bf_{ll}}$, deg	$\delta_{bf_{ur}}$, deg	$\delta_{bf_{lr}}$, deg
49	5	(b)	0	0	0	0	0	0	0
50	10	↓	↓	↓	↓	↓	↓	↓	↓
51	15	↓	↓	↓	↓	↓	↓	↓	↓
52	20	↓	↓	↓	↓	↓	↓	↓	↓
53	(a)	2	↓	↓	↓	↓	↓	↓	↓
54	↓	0	↓	↓	↓	↓	↓	↓	↓
180	↓	↓	↓	↓	↓	↓	−10	↓	−10
186	↓	↓	↓	↓	↓	↓	−10	10	0
192	↓	↓	↓	↓	↓	10	0	10	↓
198	↓	↓	5	5	↓	0	↓	0	↓
210	↓	↓	−5	−5	↓	↓	↓	↓	↓
216	↓	↓	−10	−10	↓	↓	↓	↓	↓

[a]Angle-of-attack sweep, −10°–30° by ∼2° increments.
[b]Angle-of-sideslip sweep, −10°–10° by ∼1° increments.

Table III. Input Quantities Required for the HL-20 Aerodynamic Model

Symbol	Units	Positive direction	Description
δ_{wf_l}	deg	TED	Left wing-flap position
δ_{wf_r}	deg	TED	Right wing-flap position
$\delta_{bf_{ul}}$	deg	TED	Upper left body-flap position
$\delta_{bf_{ll}}$	deg	TED	Lower left body-flap position
$\delta_{bf_{ur}}$	deg	TED	Upper right body-flap position
$\delta_{bf_{lr}}$	deg	TED	Lower right body-flap position
δ_r	deg	TEL	Rudder position
$\bar{q}$	lb/ft^2		Dynamic pressure
α	deg	ANU	Angle of attack
β	deg	ANL	Angle of sideslip
p	rad/sec	RWD	Roll rate
q	rad/sec	ANU	Pitch rate
r	rad/sec	ANR	Yaw rate
V	ft/sec		Wind relative velocity
δ_{lg}	0°–98°	0 = Up	Landing-gear extension
h	ft	Up	Height above ground of reference point

Table IV. Reference Values for HL-20 Aerodynamic Model

Reference area, S	286.45 ft^2
Reference length, $\bar{c}$	28.24 ft
Reference span, b	13.89 ft

Table V. Output Quantities From HL-20 Aerodynamic Model

Symbol	Units	Positive direction	Description
F_X	lb	Forward	Aerodynamic force, X body axis
F_Y	lb	Right	Aerodynamic force, Y body axis
F_Z	lb	Down	Aerodynamic force, Z body axis
M_X	ft-lb	RWD	Aerodynamic torque, X body axis
M_Y	ft-lb	ANU	Aerodynamic torque, Y body axis
M_Z	ft-lb	ANR	Aerodynamic torque, Z body axis

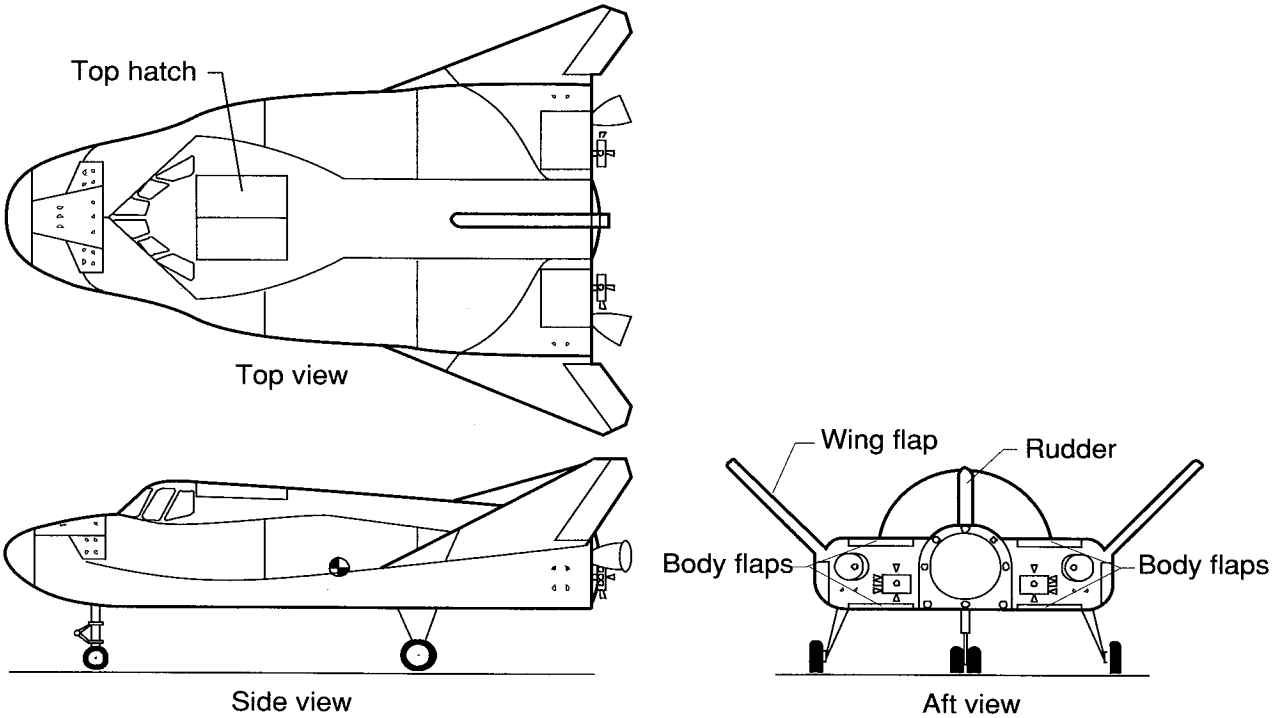

Figure 1. HL-20 lifting-body vehicle.

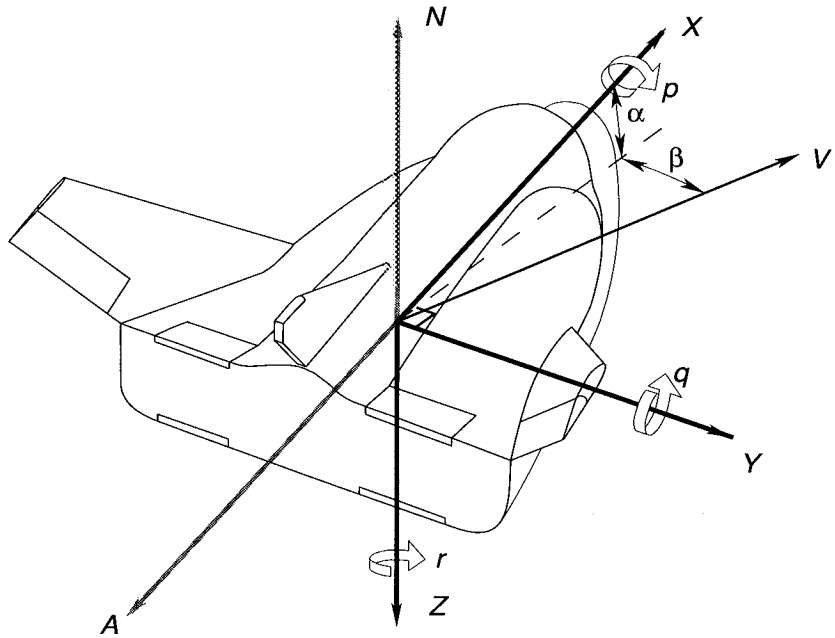

Figure 2. Measurement and axis sign conventions.

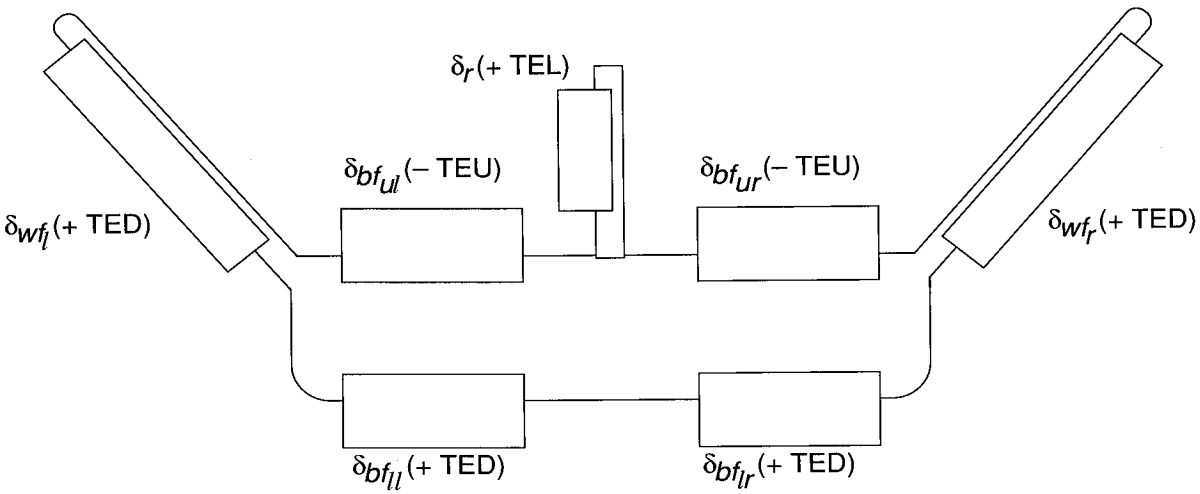

Figure 3. Control-surface nomenclature and sign conventions (viewed from rear).

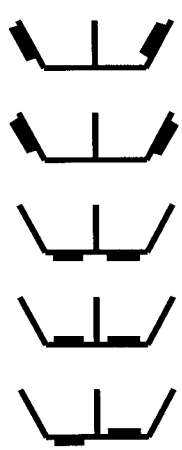

$$\delta a = \frac{\delta wf_l - \delta wf_r}{2}$$

$$\delta e = \frac{\delta wf_l + \delta wf_r}{2}$$

$$\delta f^+ = \frac{\delta bf_{ll} + \delta bf_{lr}}{2}$$

$$\delta f^- = \frac{\delta bf_{ul} + \delta bf_{ur}}{2}$$

$$\delta_\Delta f = \frac{\delta bf_{ul} + \delta bf_{ll} - \delta bf_{ur} - \delta bf_{lr}}{2}$$

Figure 4. Control-surface combination definitions (viewed from rear).

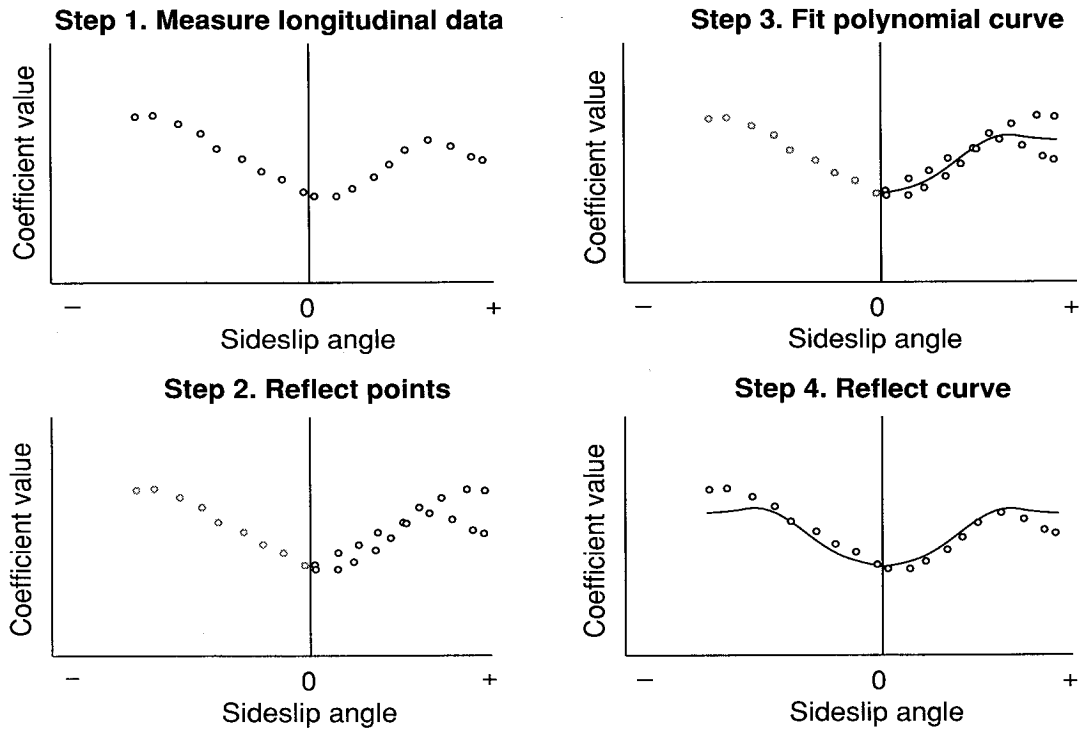

(a) Longitudinal data coefficients.

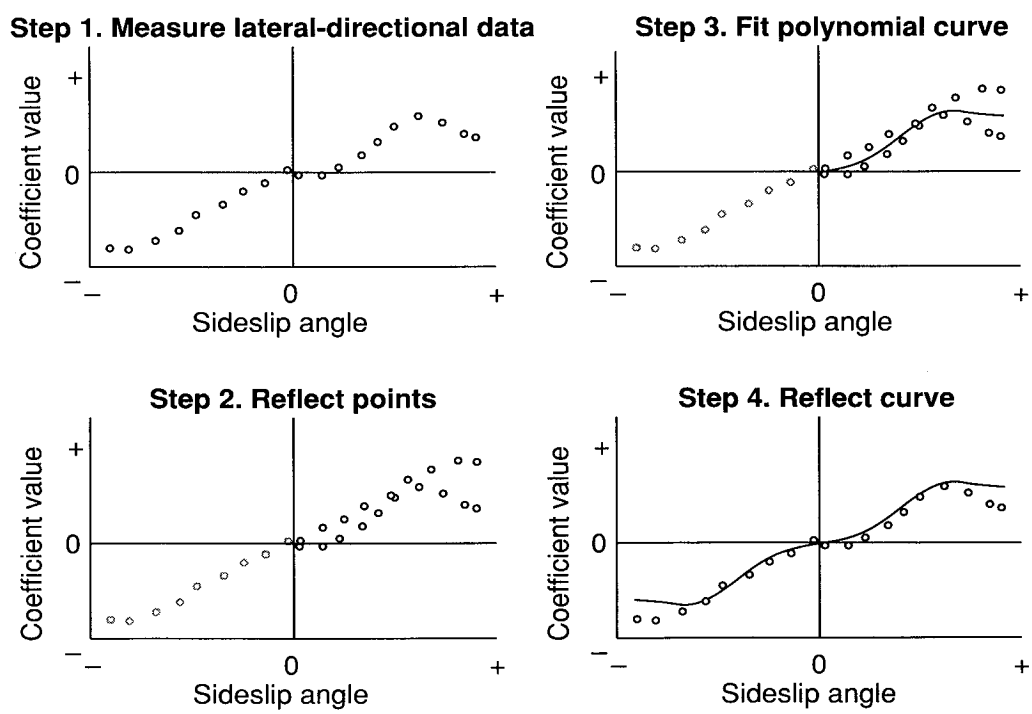

(b) Lateral-directional data coefficients.

Figure 5. Curve-fitting technique assuming lateral symmetry. Shaded circles indicate points that have been reflected.

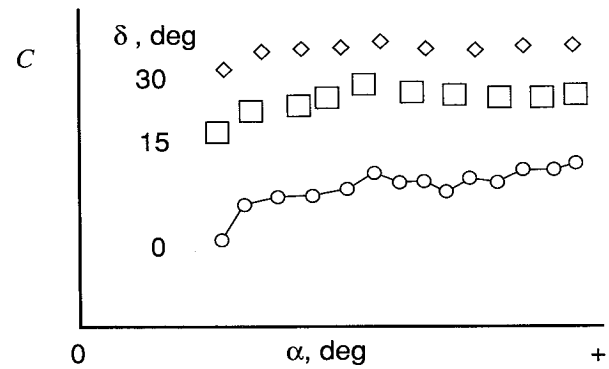

(a) Typical measurements of original wind tunnel coefficient.

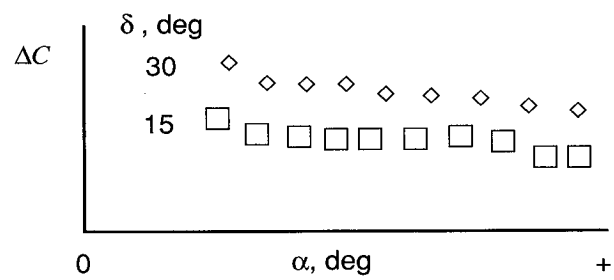

(b) Increments to basic configuration due to deflection (linear interpolation of basic data points required).

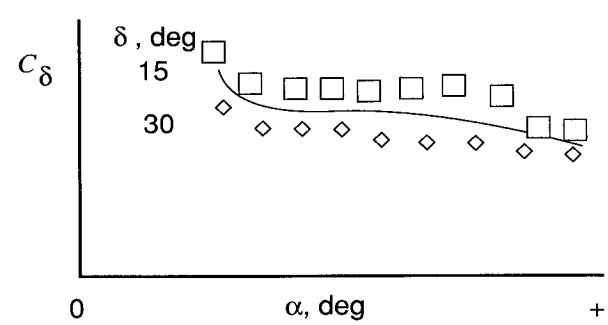

(c) Derivatives with deflection showing polynomial curve fit (formed by dividing increments by deflection).

Figure 6. Procedure for obtaining polynomial curve fits for derivative data.

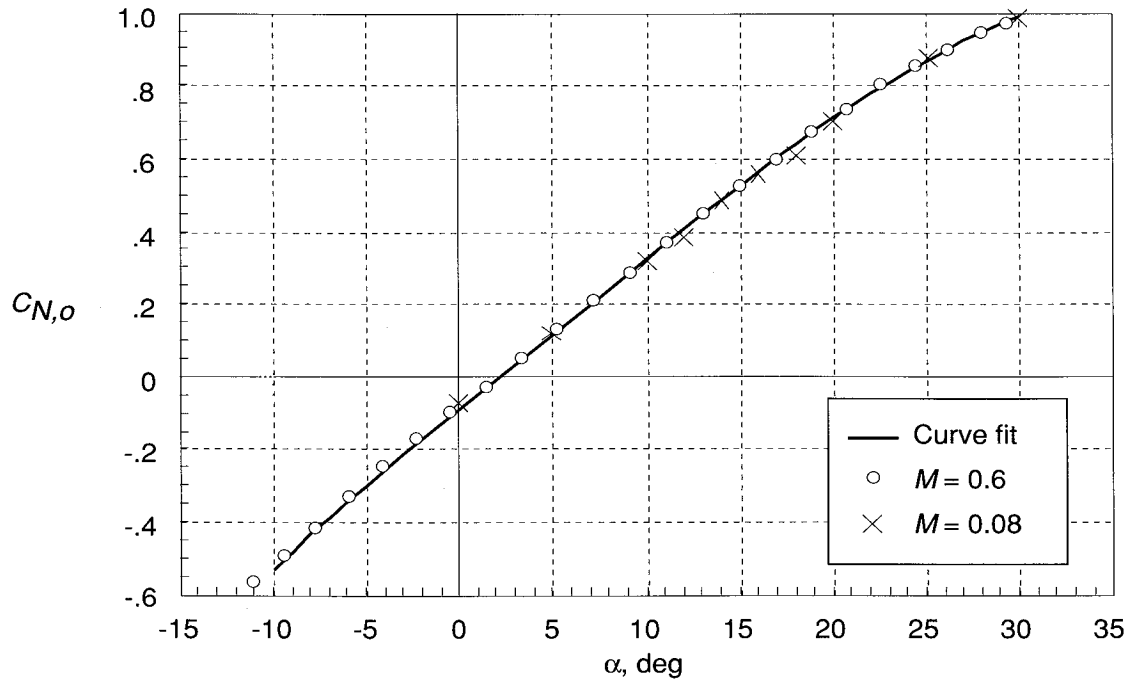

(a) $C_{N,o}$ versus α at $\beta = 0°$.

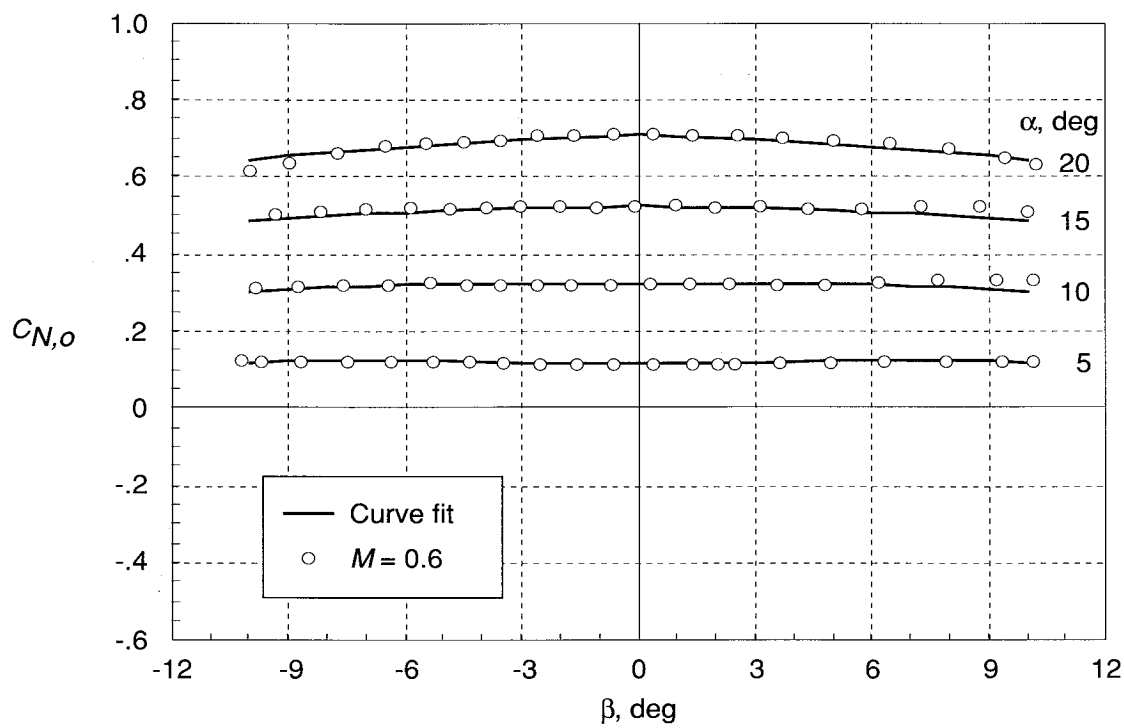

(b) $C_{N,o}$ versus β at various values of α.

Figure 7. Wind tunnel data and polynomial curve fits for normal-force coefficient $C_{N,o}$ for basic configuration.

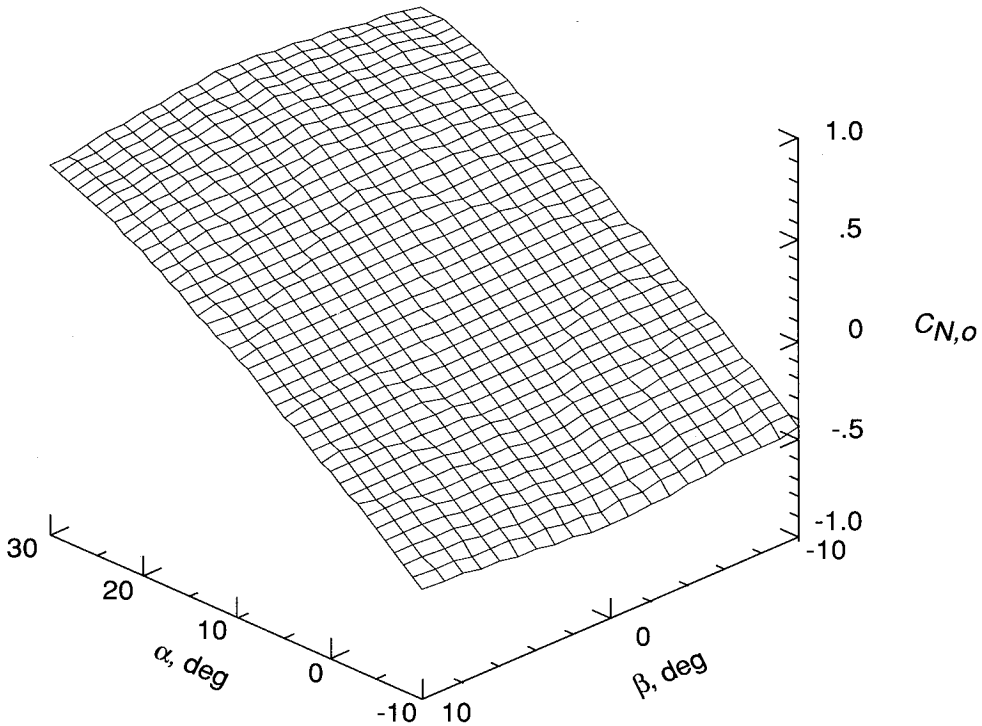

(c) $C_{N,o}$ polynomial surface with constant spacing between α and β grid points.

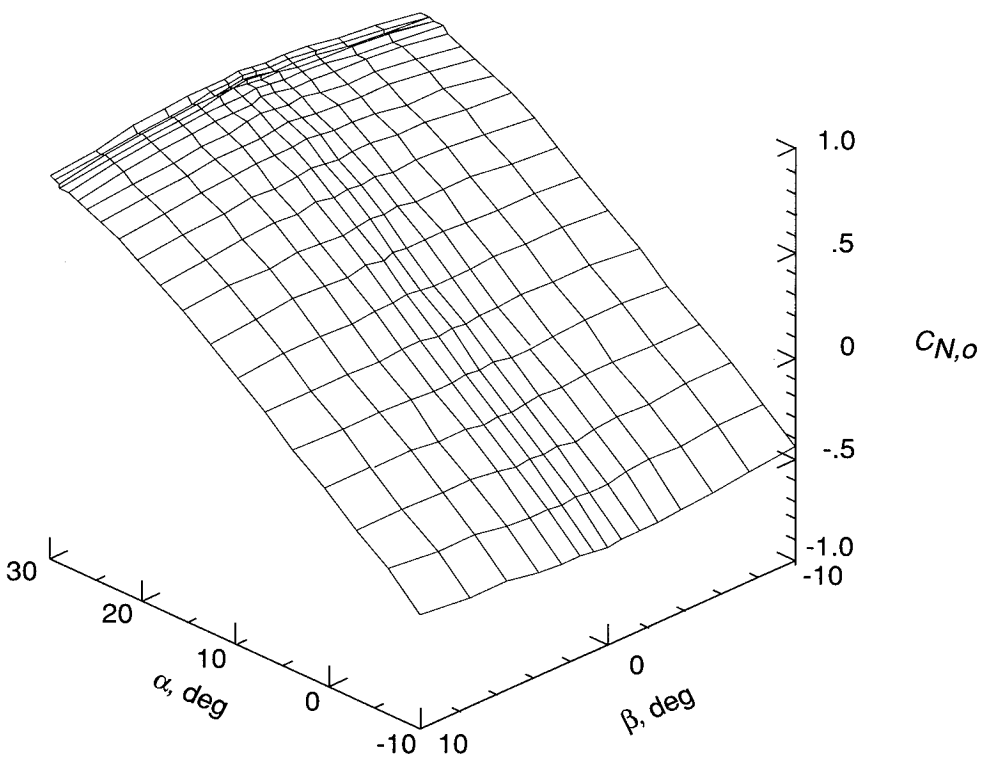

(d) $C_{N,o}$ polynomial surface drawn with α and β grid point sets used to generate table A3.

Figure 7. Concluded.

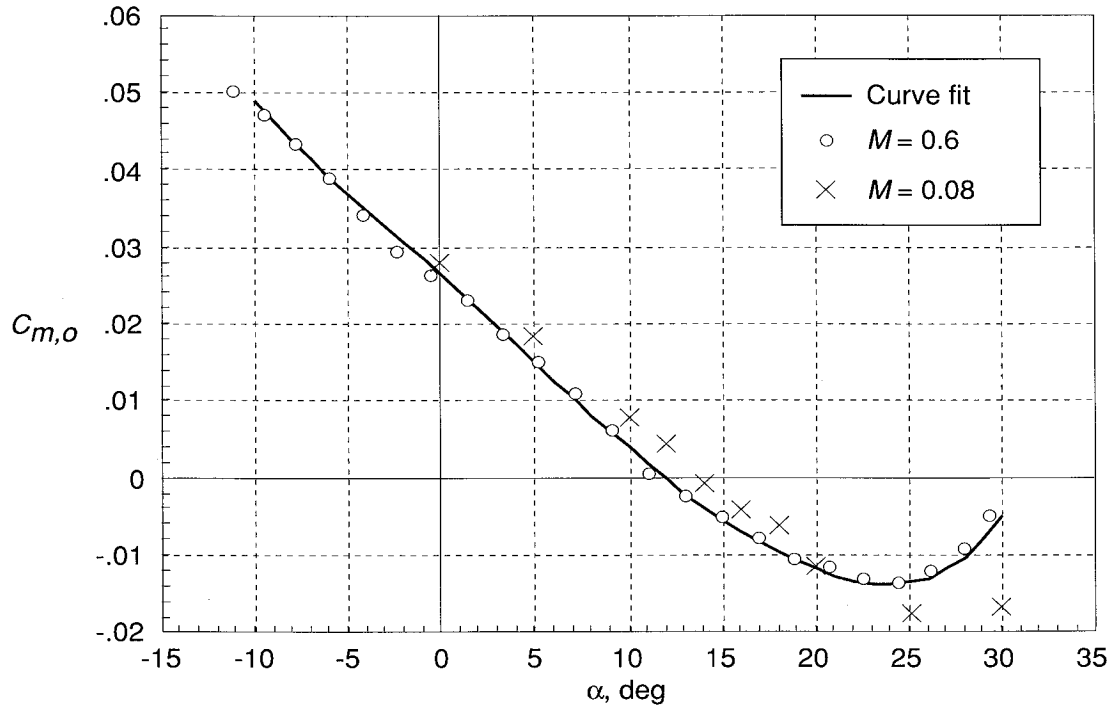

(a) $C_{m,o}$ versus α at $\beta = 0°$.

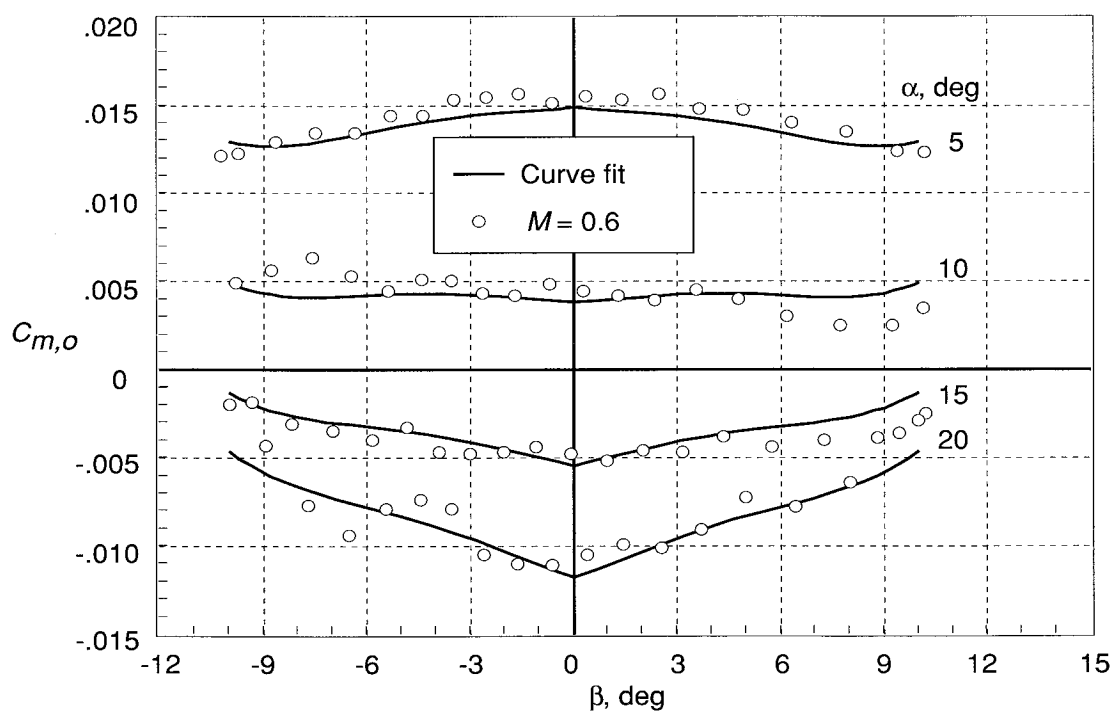

(b) $C_{m,o}$ versus β at various α values.

Figure 8. Wind tunnel data and polynomial curve fits for pitching-moment coefficient $C_{m,o}$ for basic configuration.

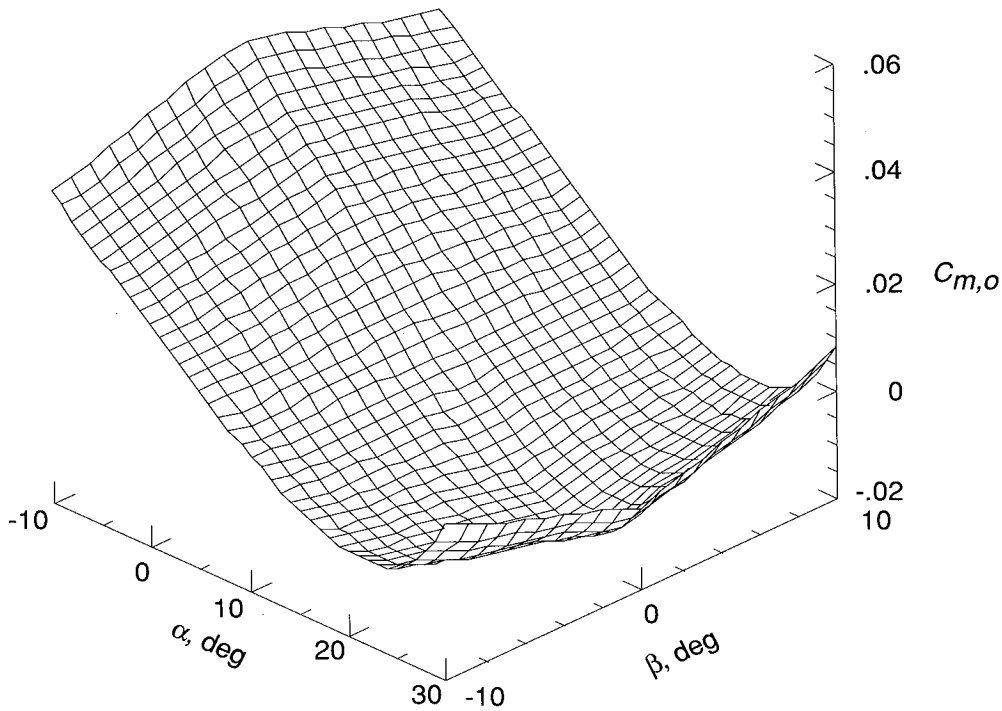

(c) $C_{m,o}$ polynomial surface with constant spacing between α and β grid points.

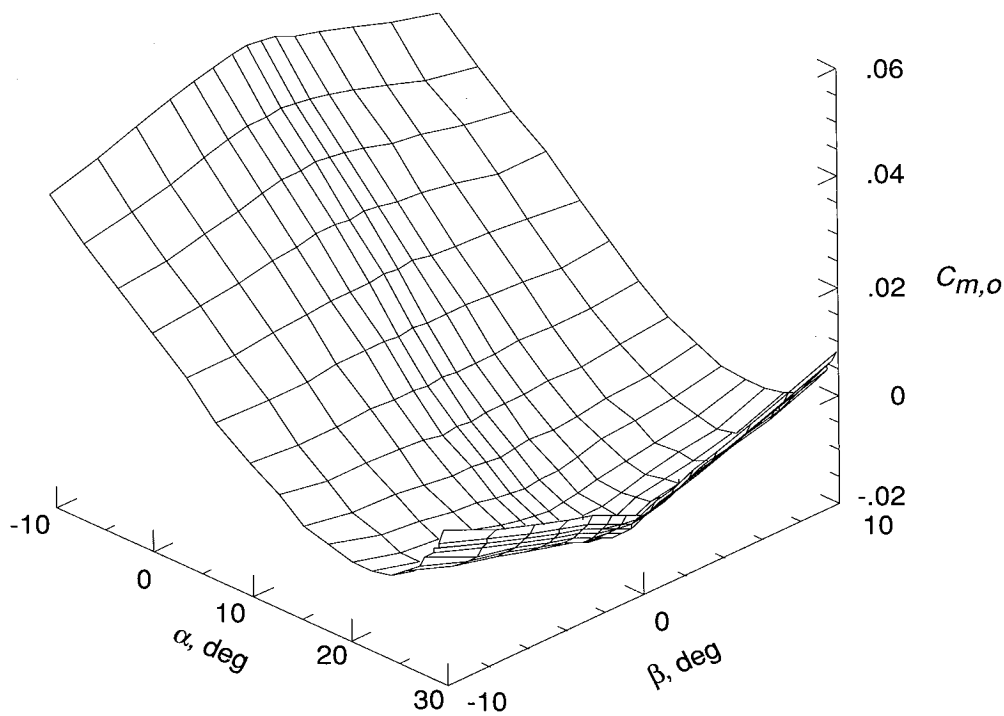

(d) $C_{m,o}$ definition grid polynomial surface drawn with α and β grid point sets used to generate table A2.

Figure 8. Concluded.

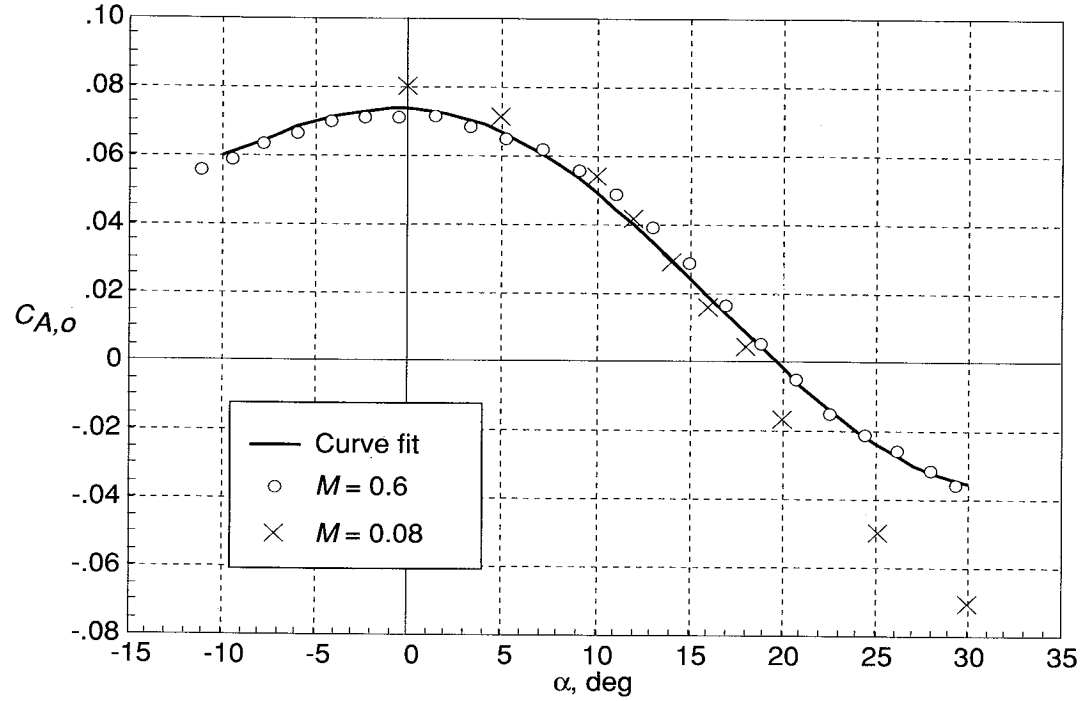

(a) $C_{A,o}$ versus α at $\beta = 0°$.

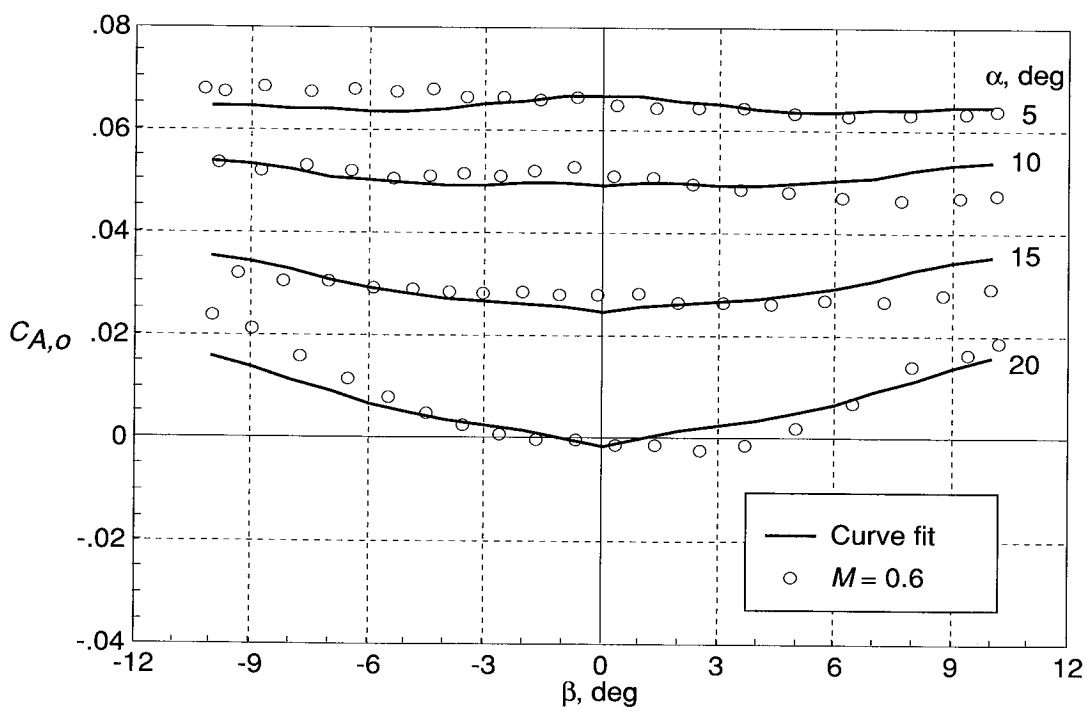

(b) $C_{A,o}$ versus β at various α values.

Figure 9. Wind tunnel data and polynomial curve fits for axial-force coefficient $C_{A,o}$ for basic configuration.

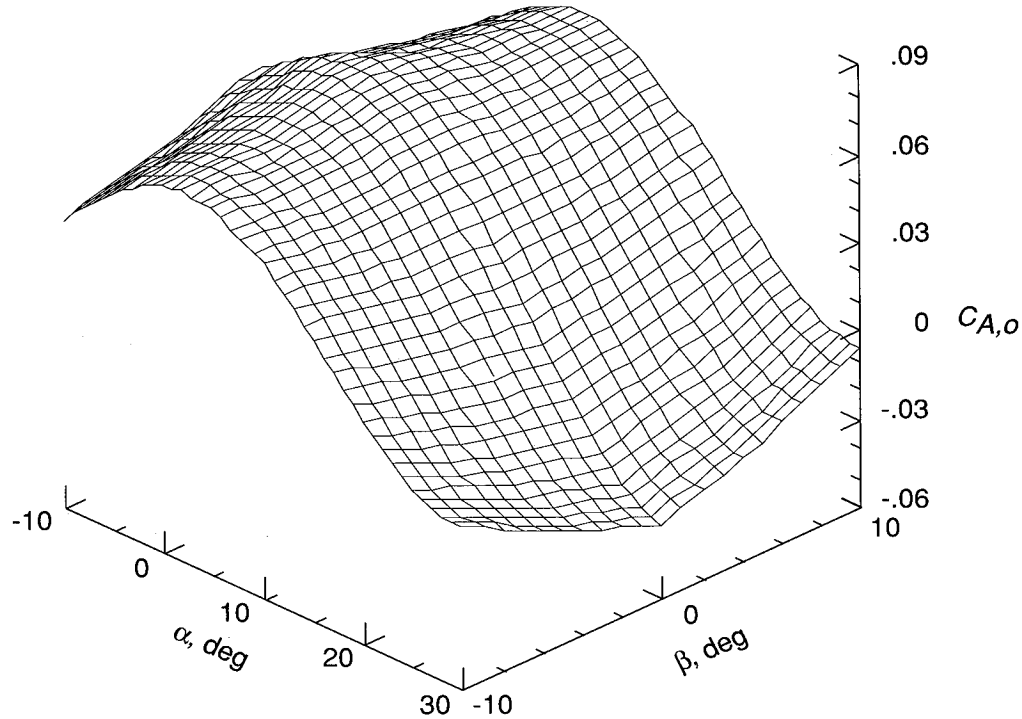

(c) $C_{A,o}$ polynomial surface with constant spacing between α and β grid points.

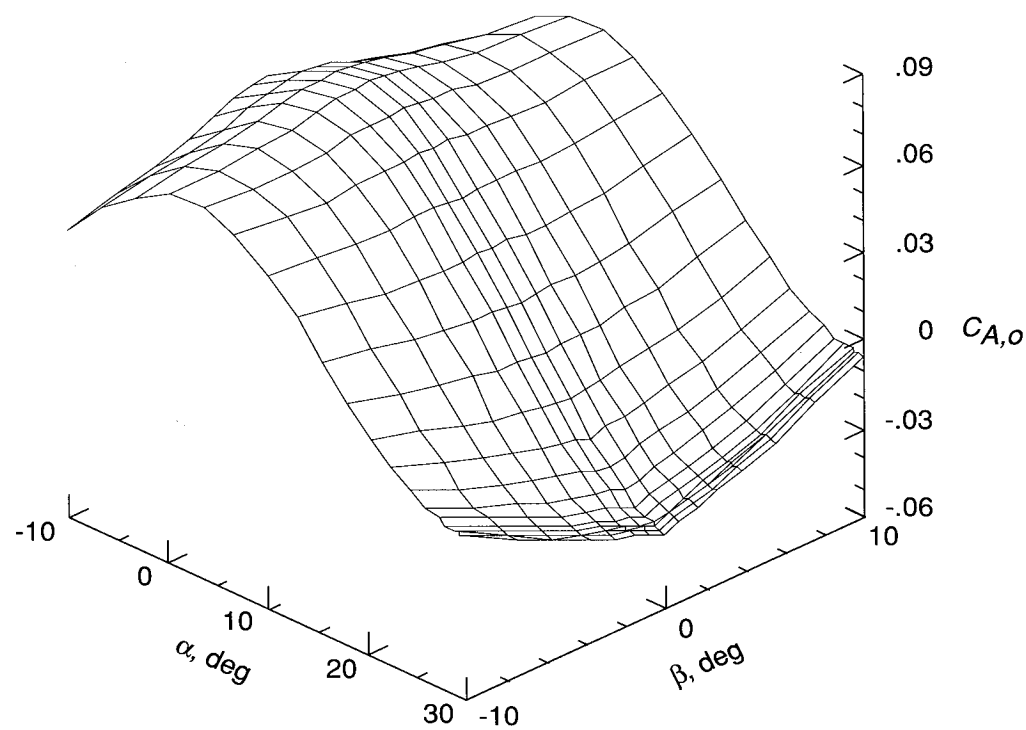

(d) $C_{A,o}$ polynomial surface drawn with α and β grid point sets used to generate table A1.

Figure 9. Concluded.

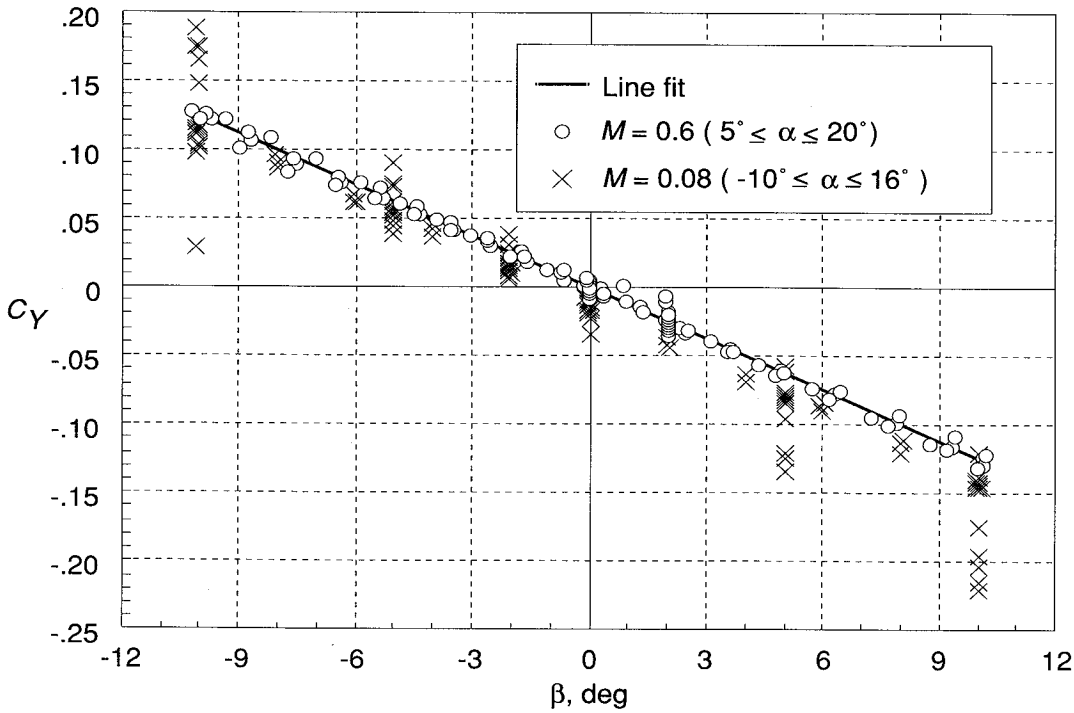

Figure 10. C_Y versus β for α between $-10°$ and $20°$.

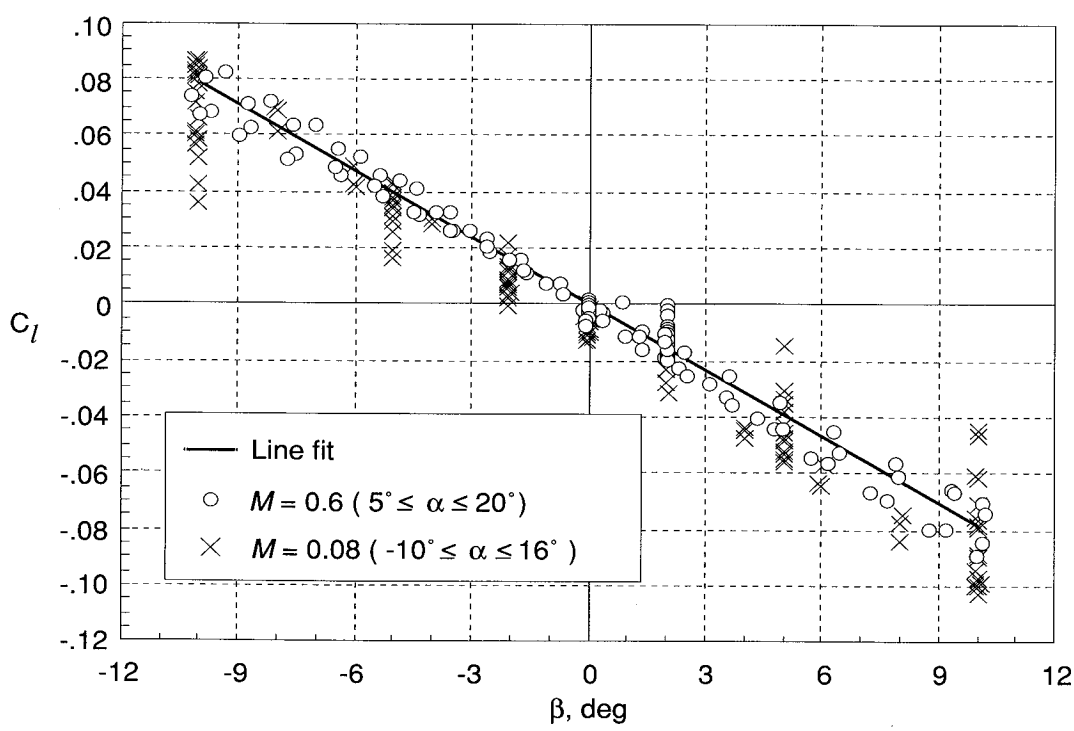

Figure 11. C_l versus β for α between $-10°$ and $20°$.

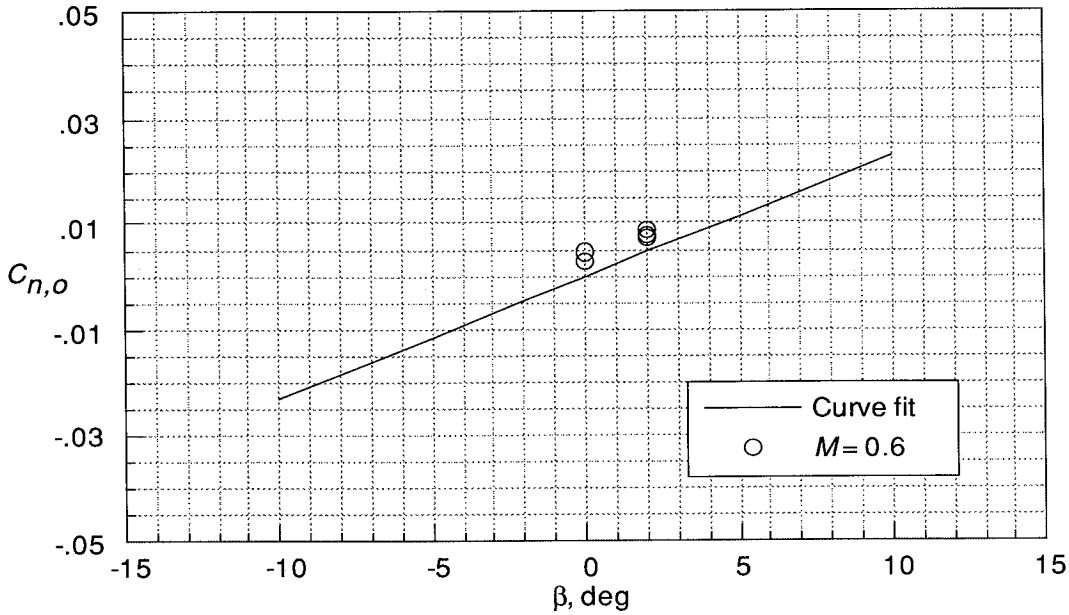

(a) $\alpha = -10°$.

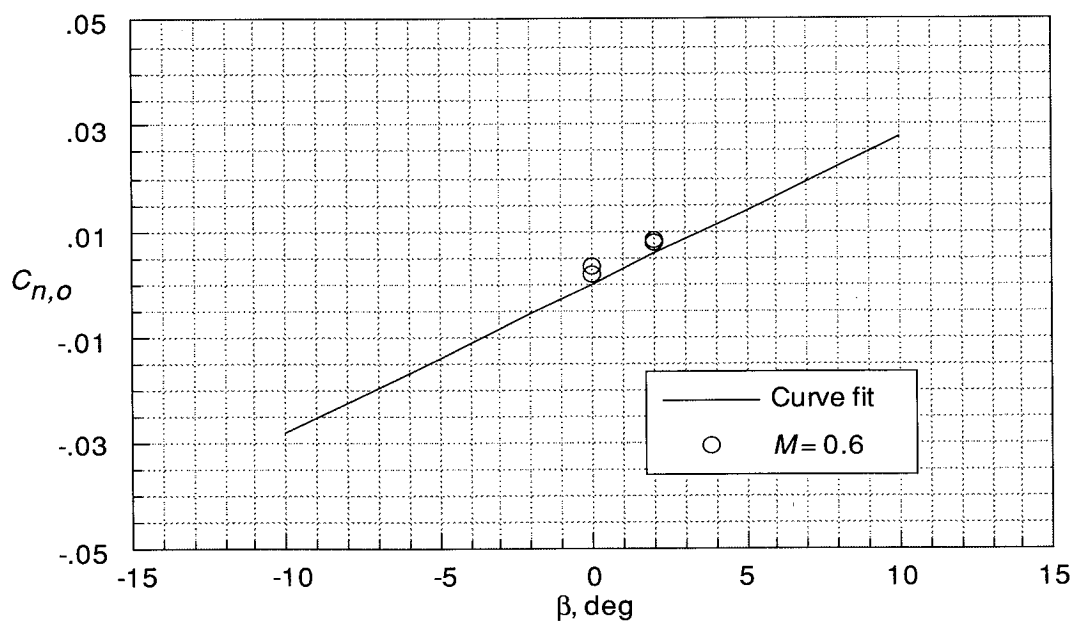

(b) $\alpha = -5°$.

Figure 12. Yawing-moment coefficient $C_{n,o}$ versus β for the basic configuration.

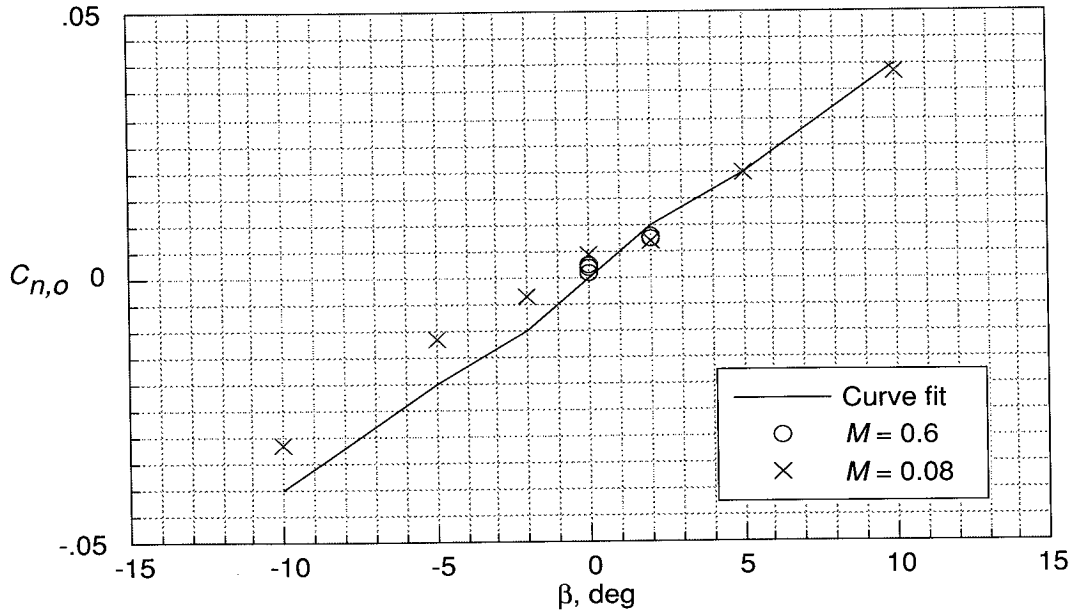

(c) $\alpha = 0°$.

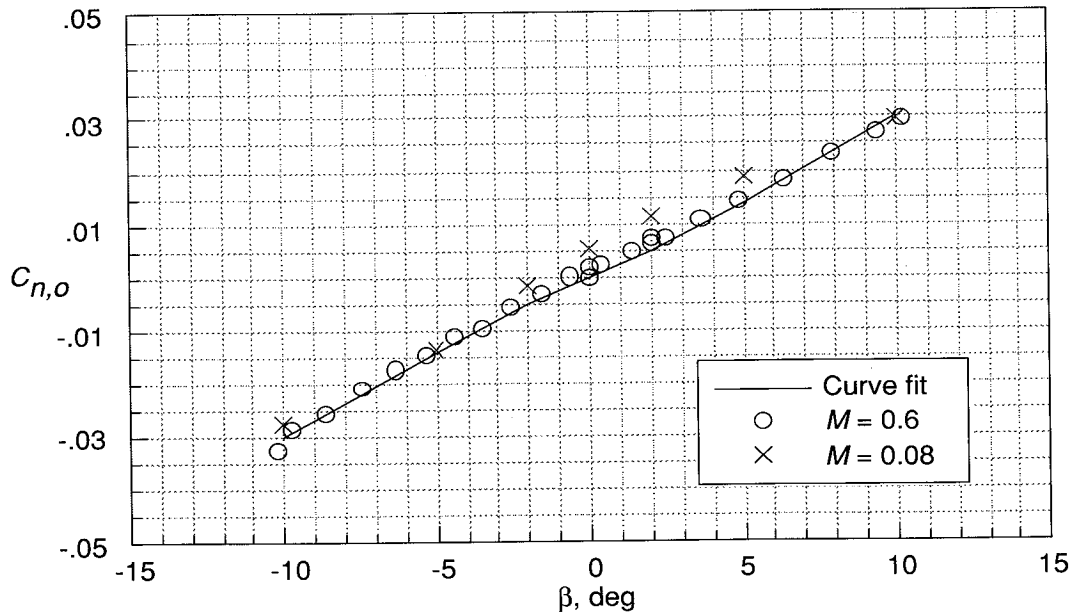

(d) $\alpha = 5°$.

Figure 12. Continued.

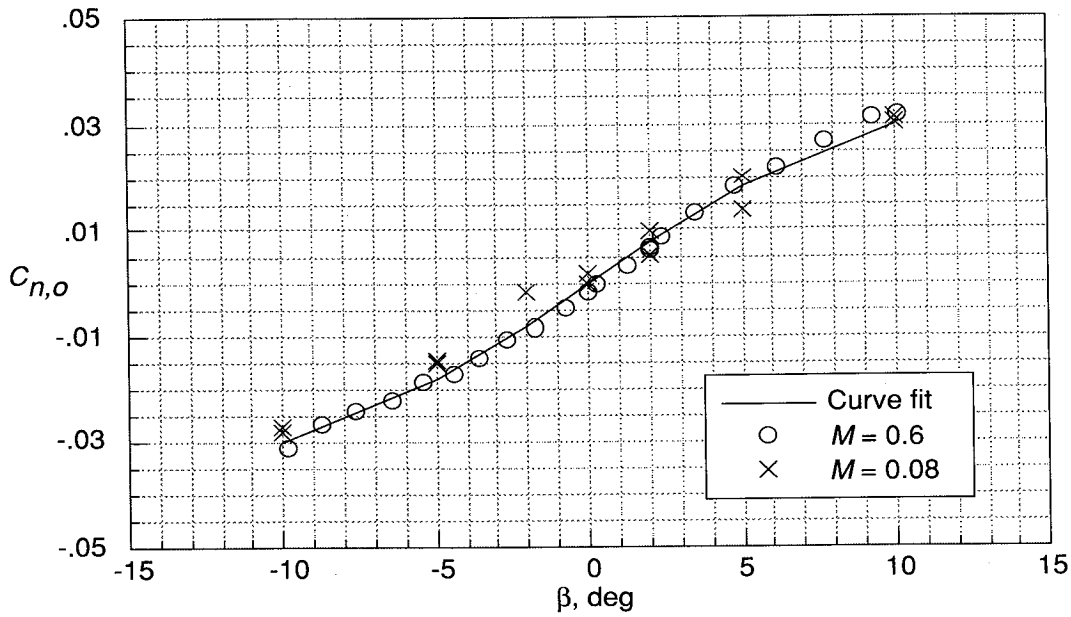

(e) $\alpha = 10°$.

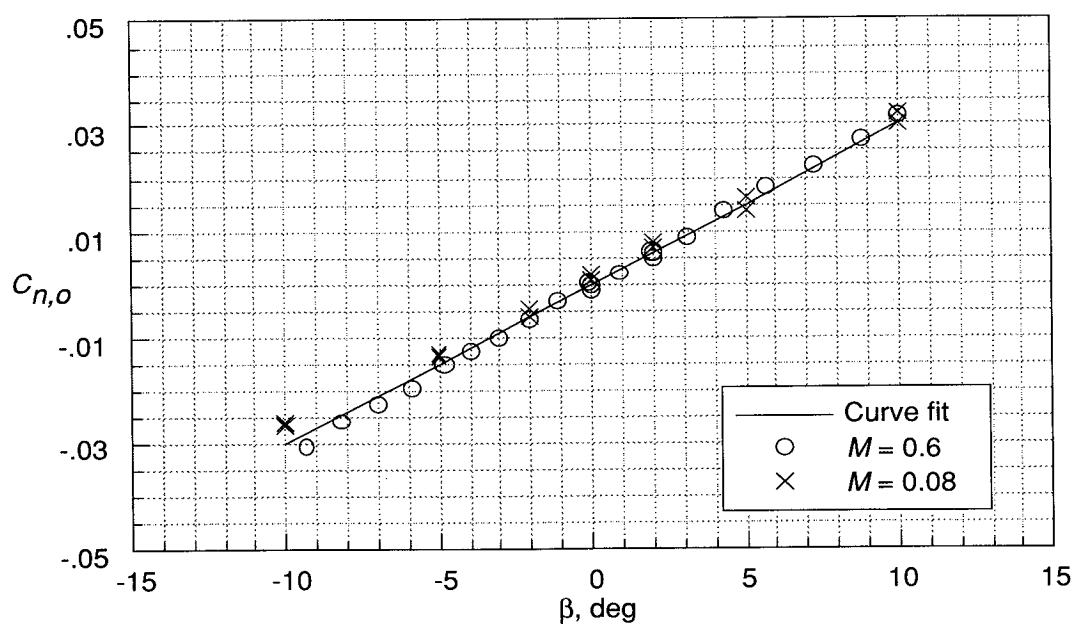

(f) $\alpha = 15°$.

Figure 12. Continued.

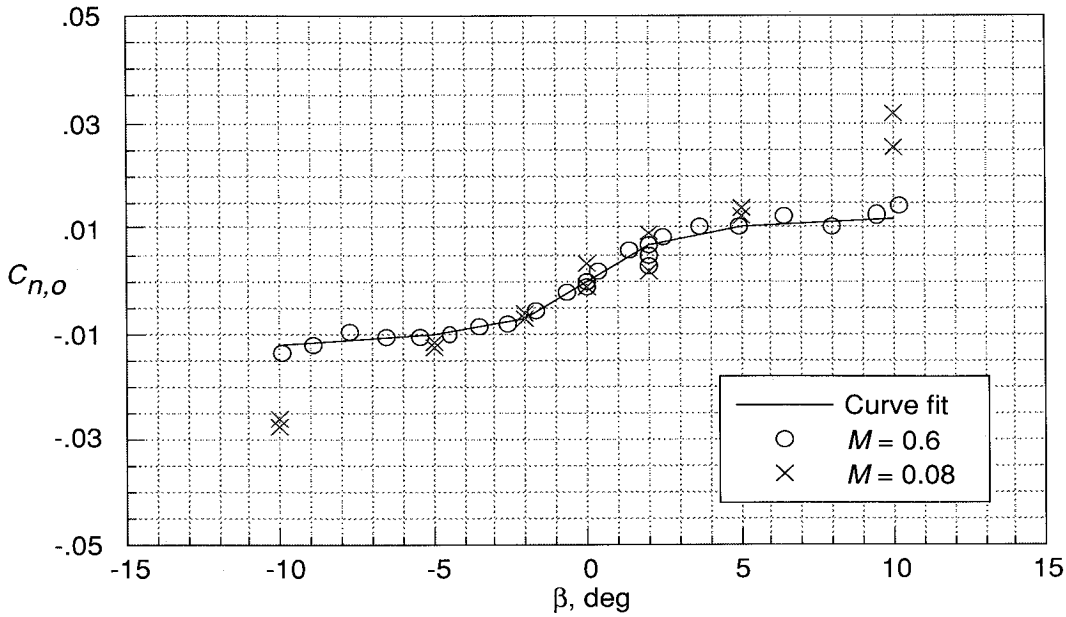

(g) $\alpha = 20°$.

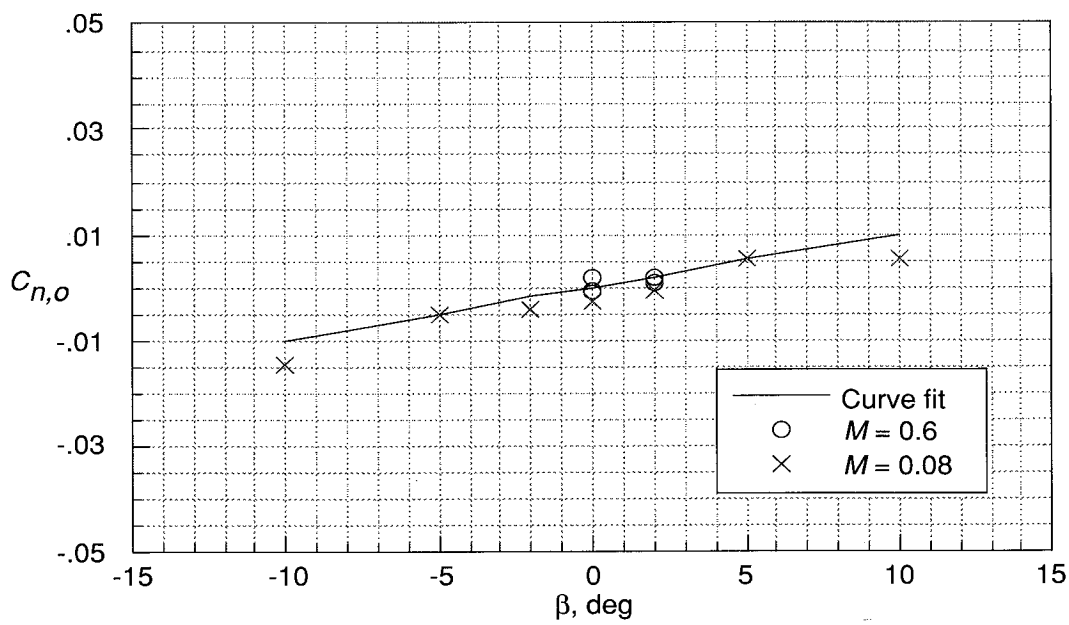

(h) $\alpha = 25°$.

Figure 12. Continued.

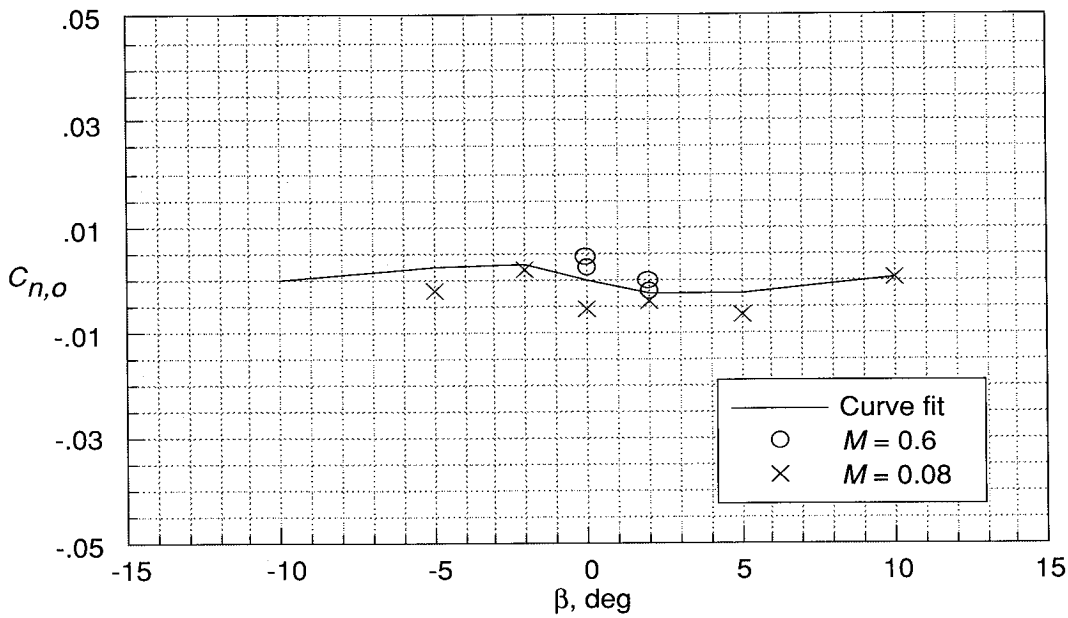

(i) $\alpha = 30°$.

Figure 12. Concluded.

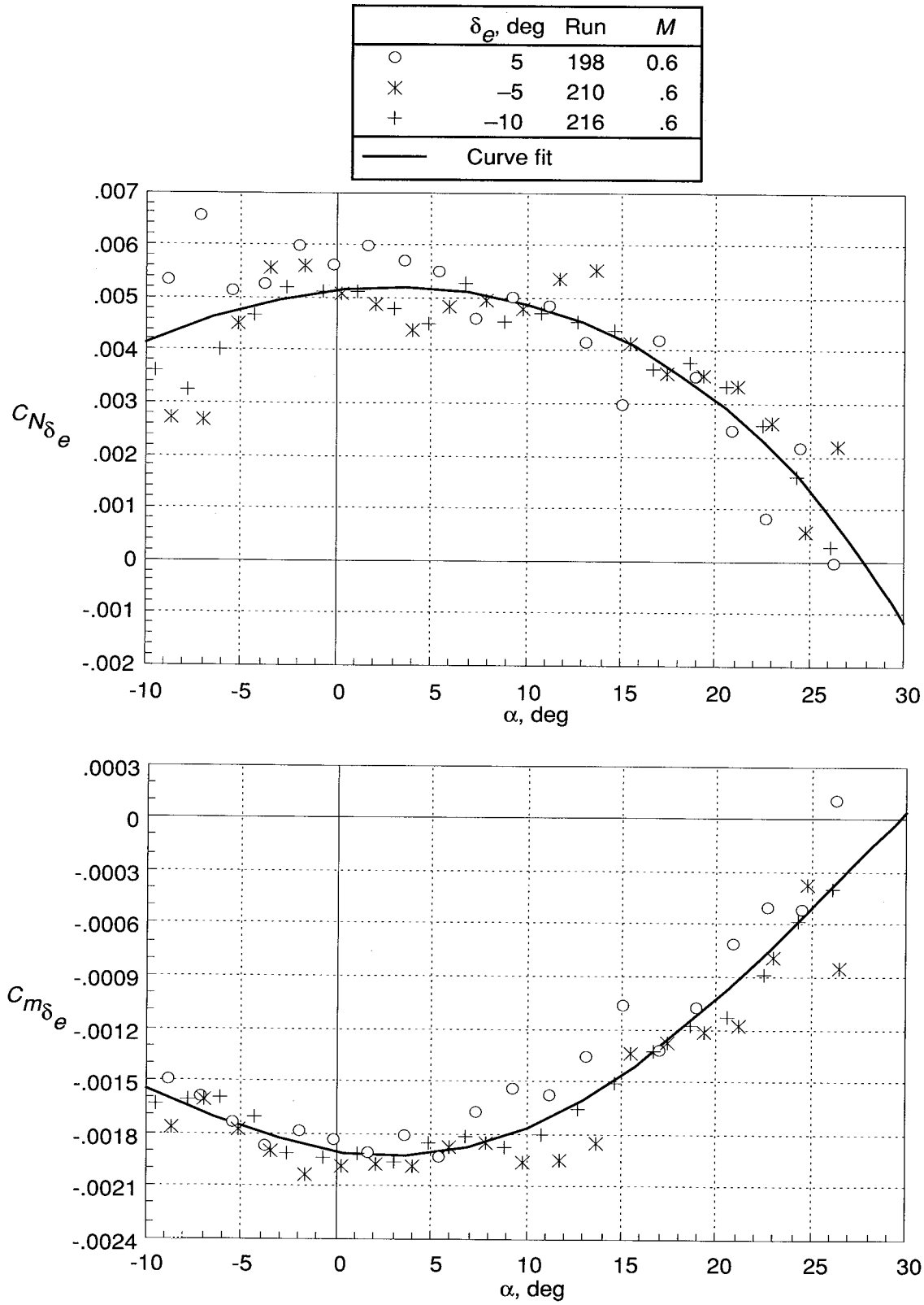

Figure 13. Effect of symmetric wing flaps on longitudinal aerodynamic characteristics.

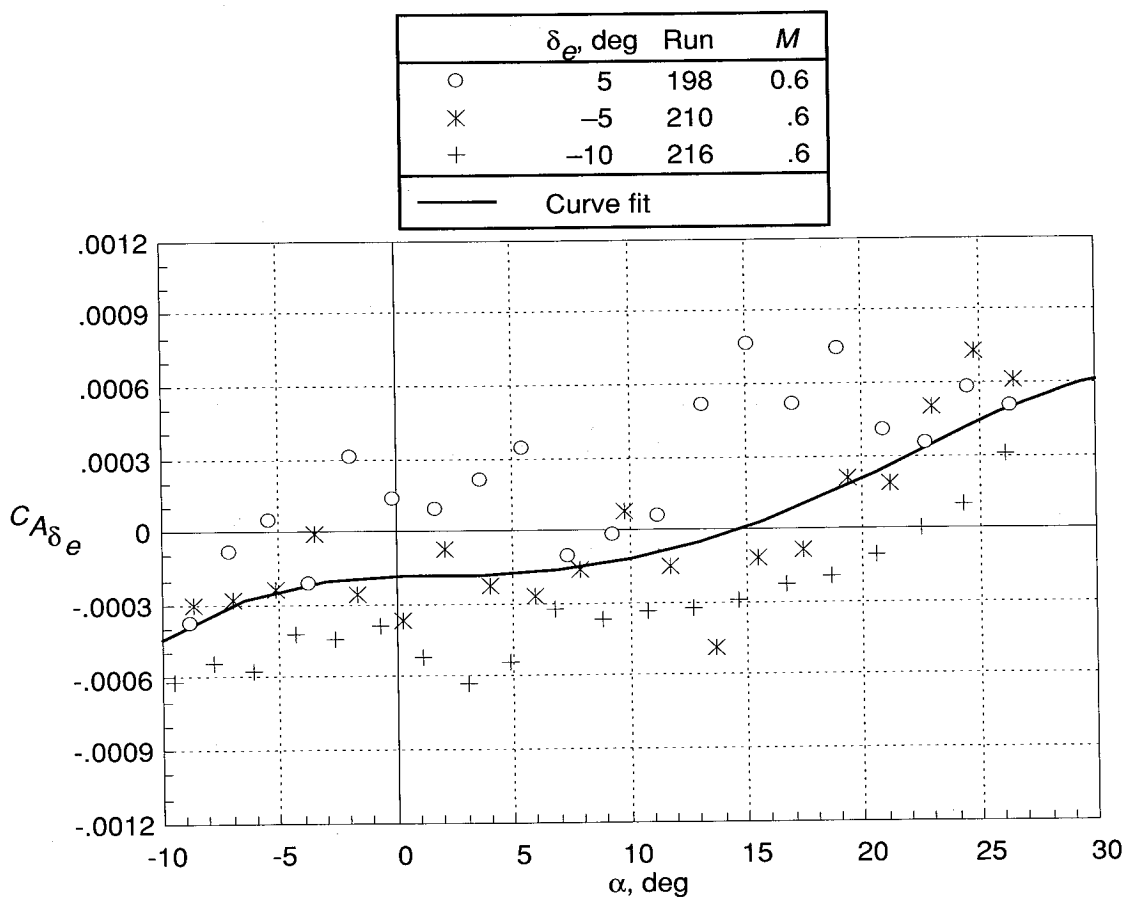

Figure 13. Concluded.

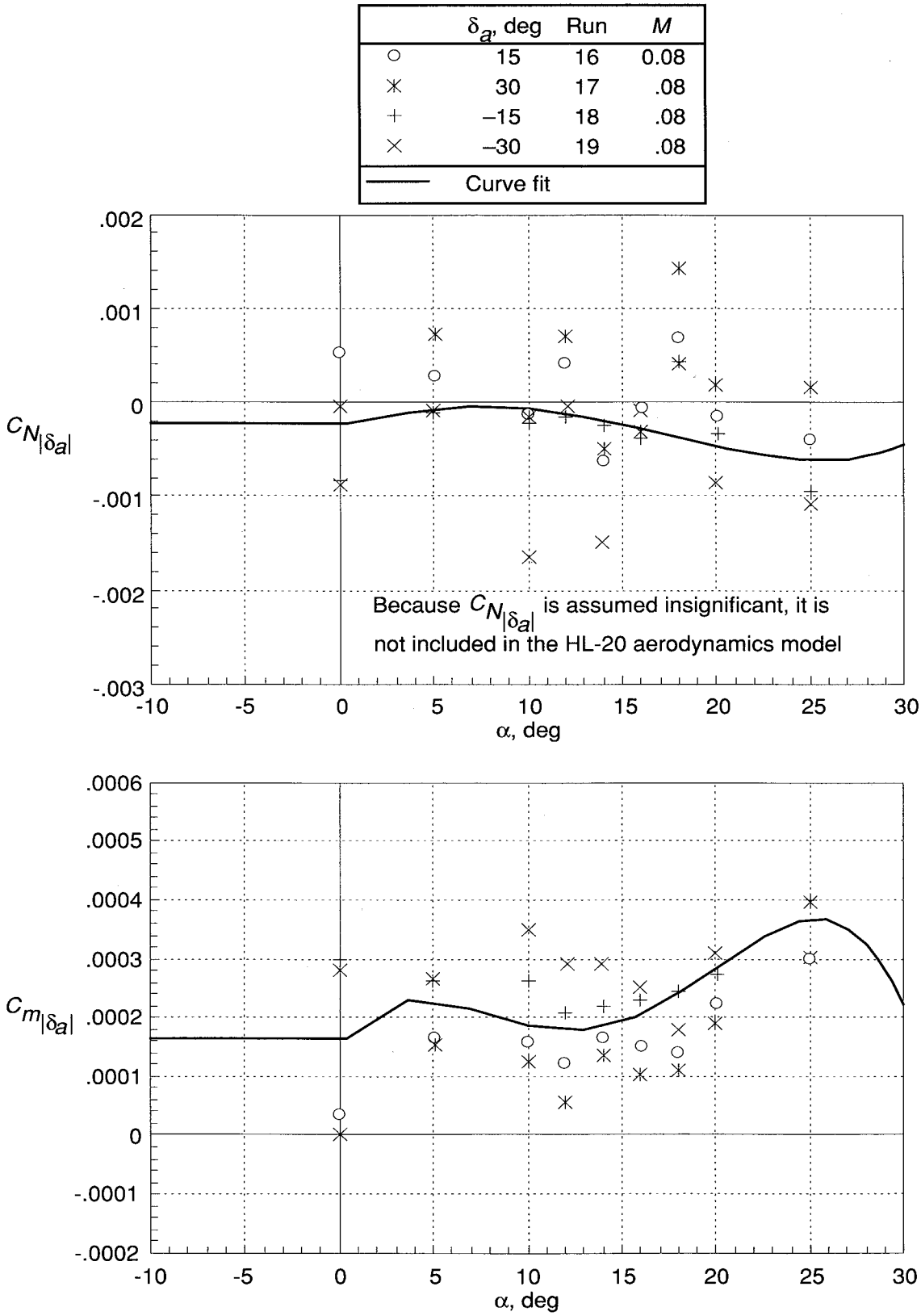

Figure 14. Effects of differential wing flaps on aerodynamic characteristics.

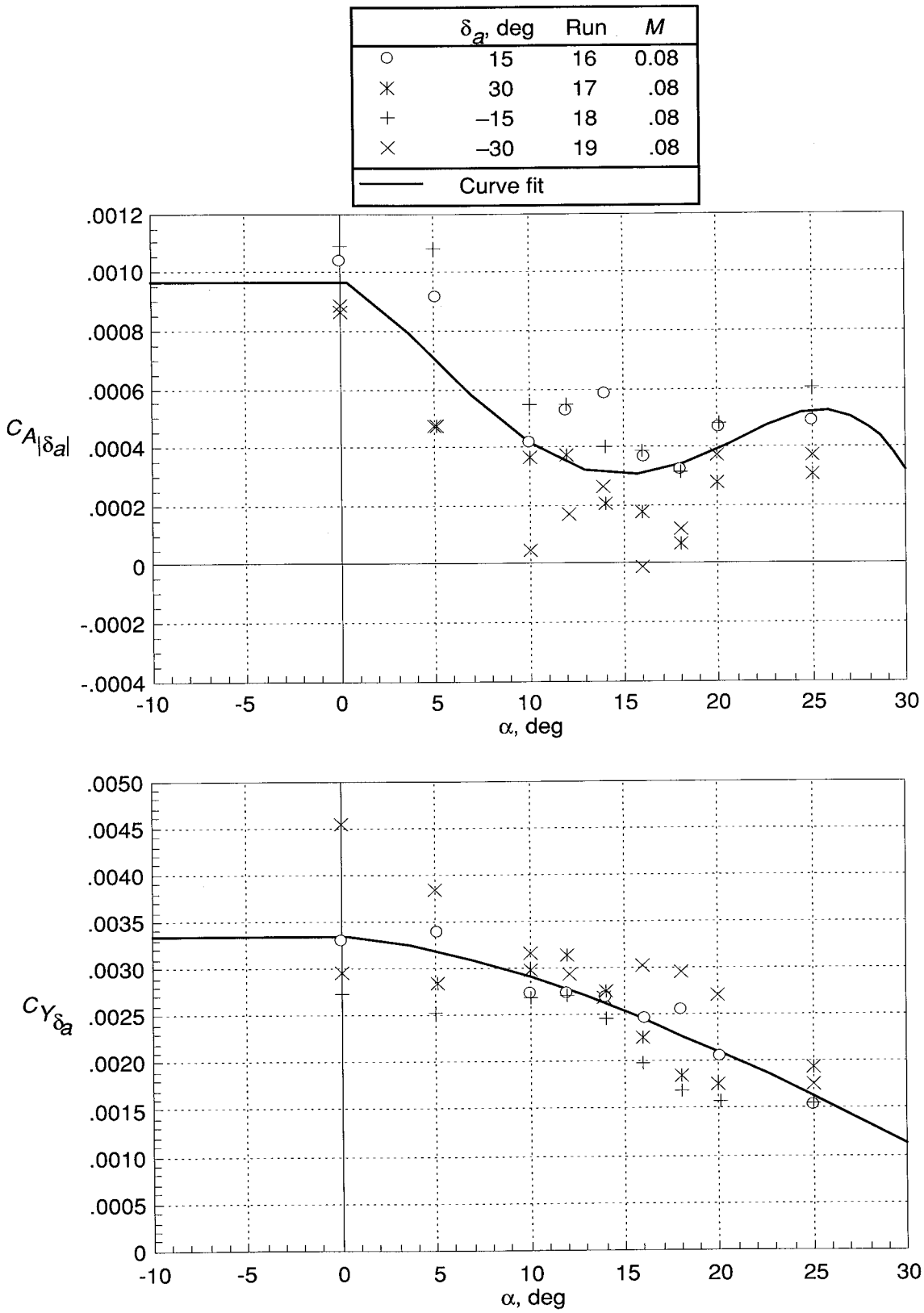

Figure 14. Continued.

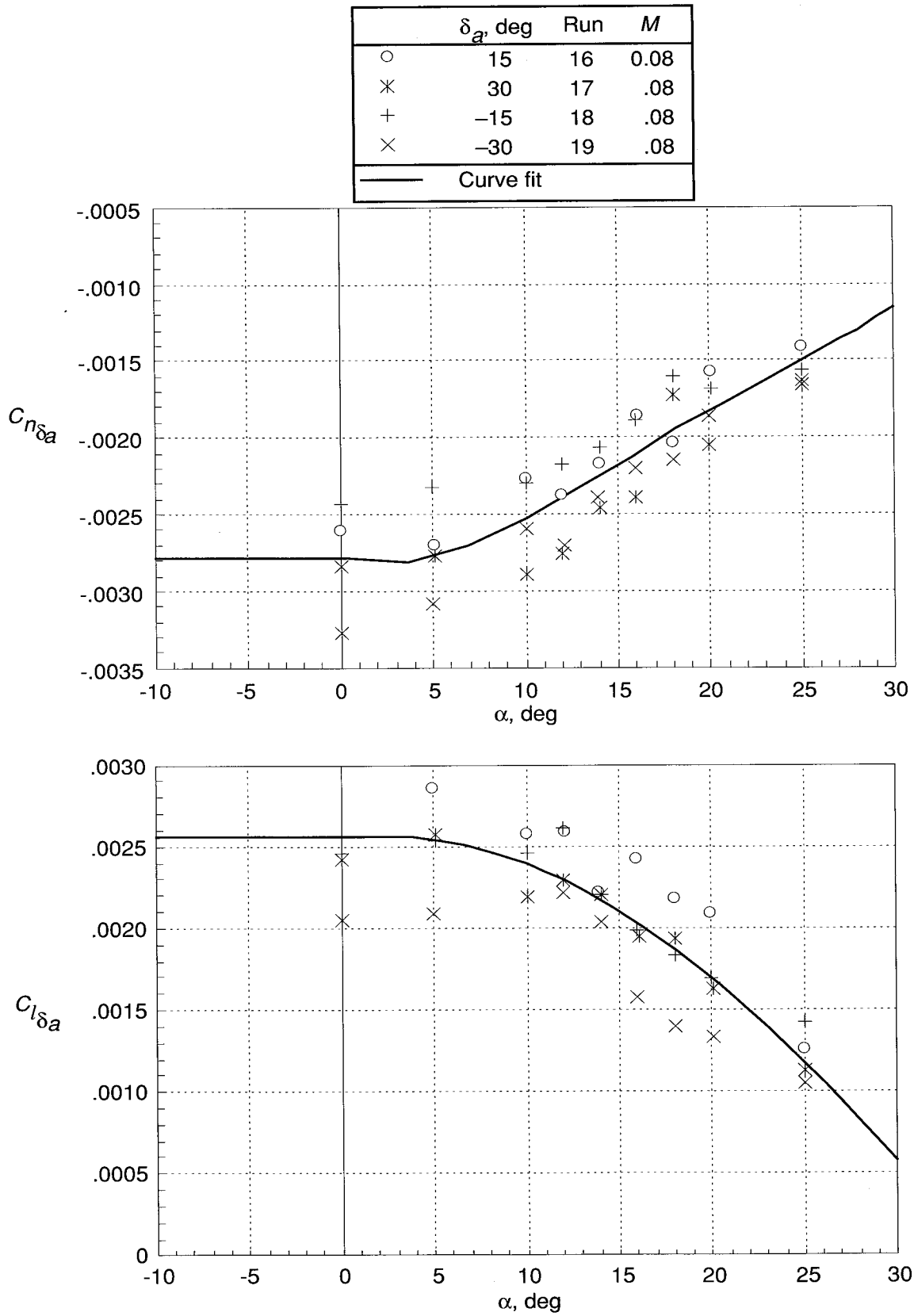

Figure 14. Concluded.

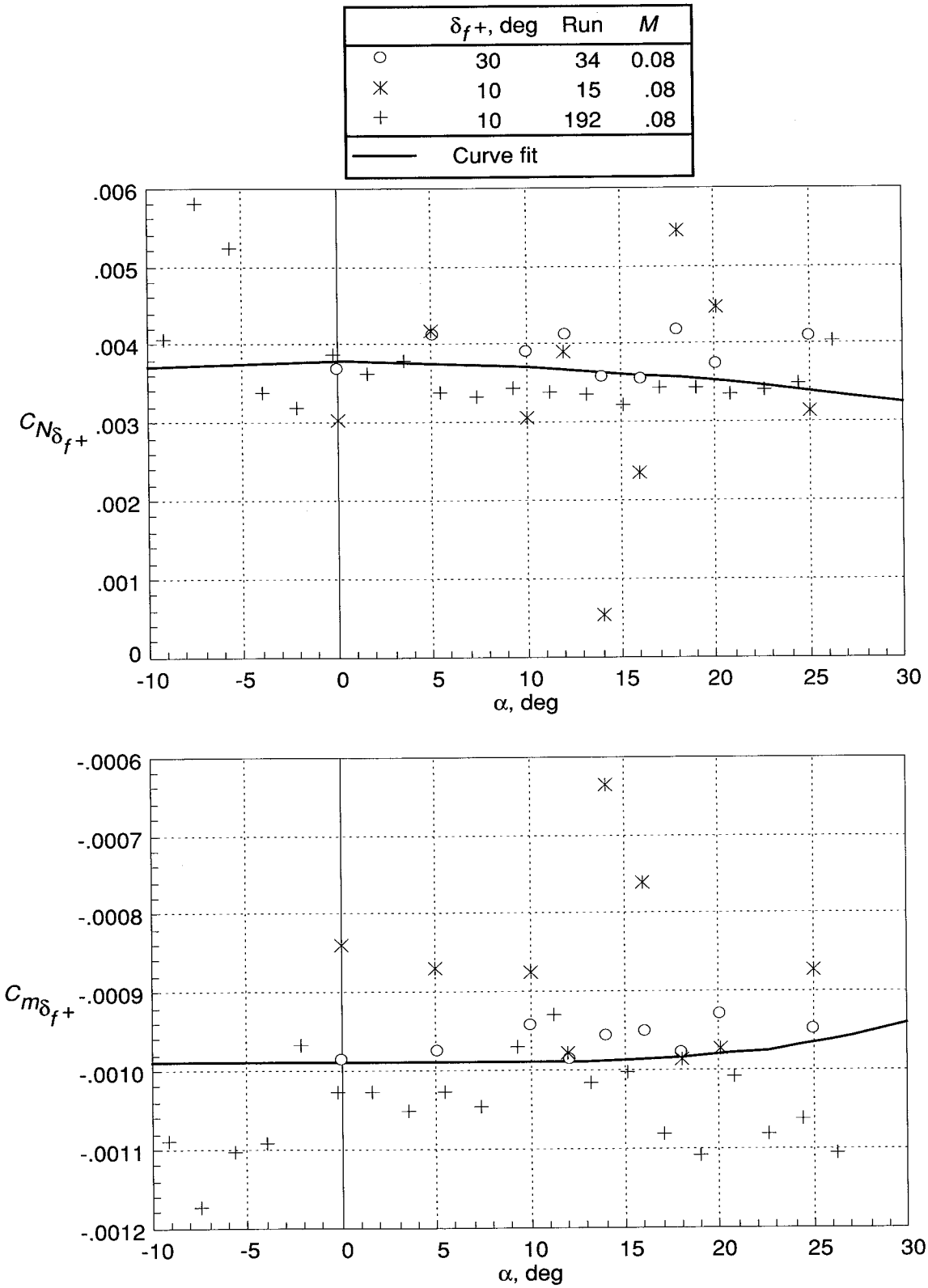

Figure 15. Effect of positive body flaps on aerodynamic characteristics.

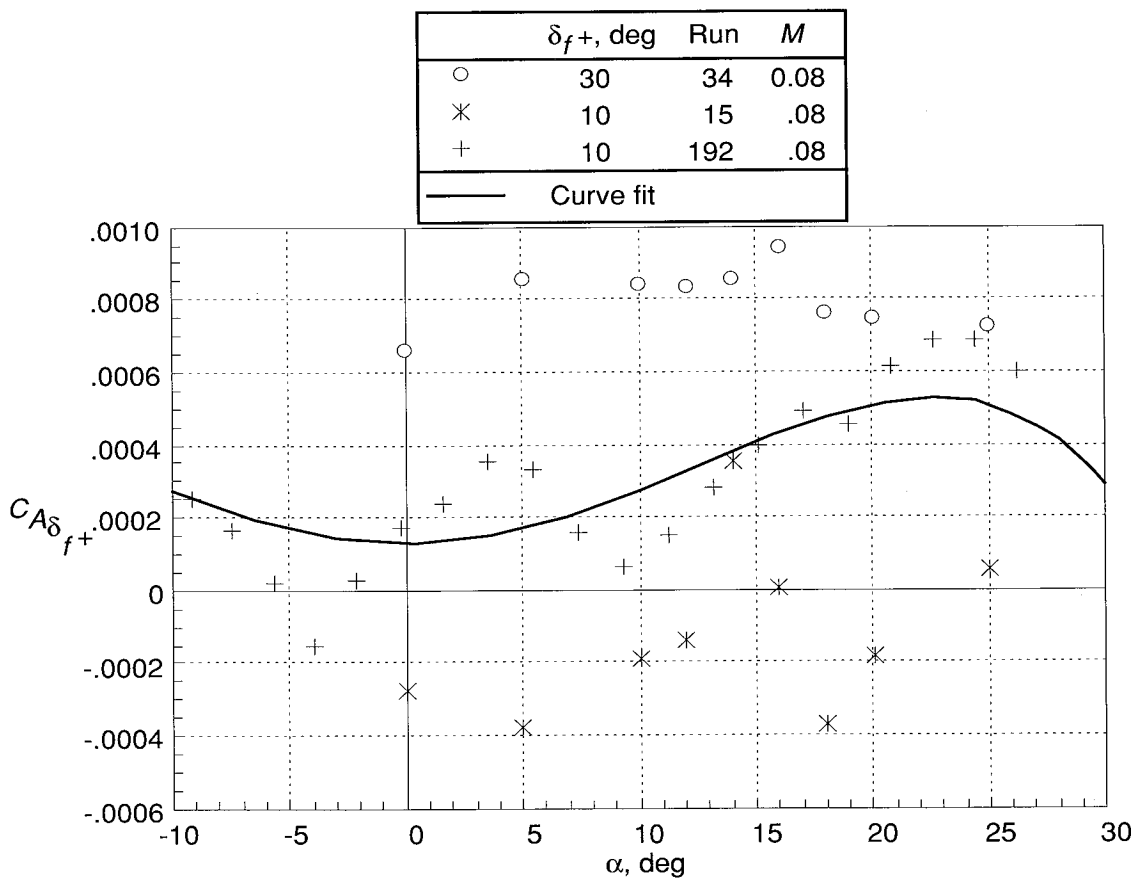

Figure 15. Concluded.

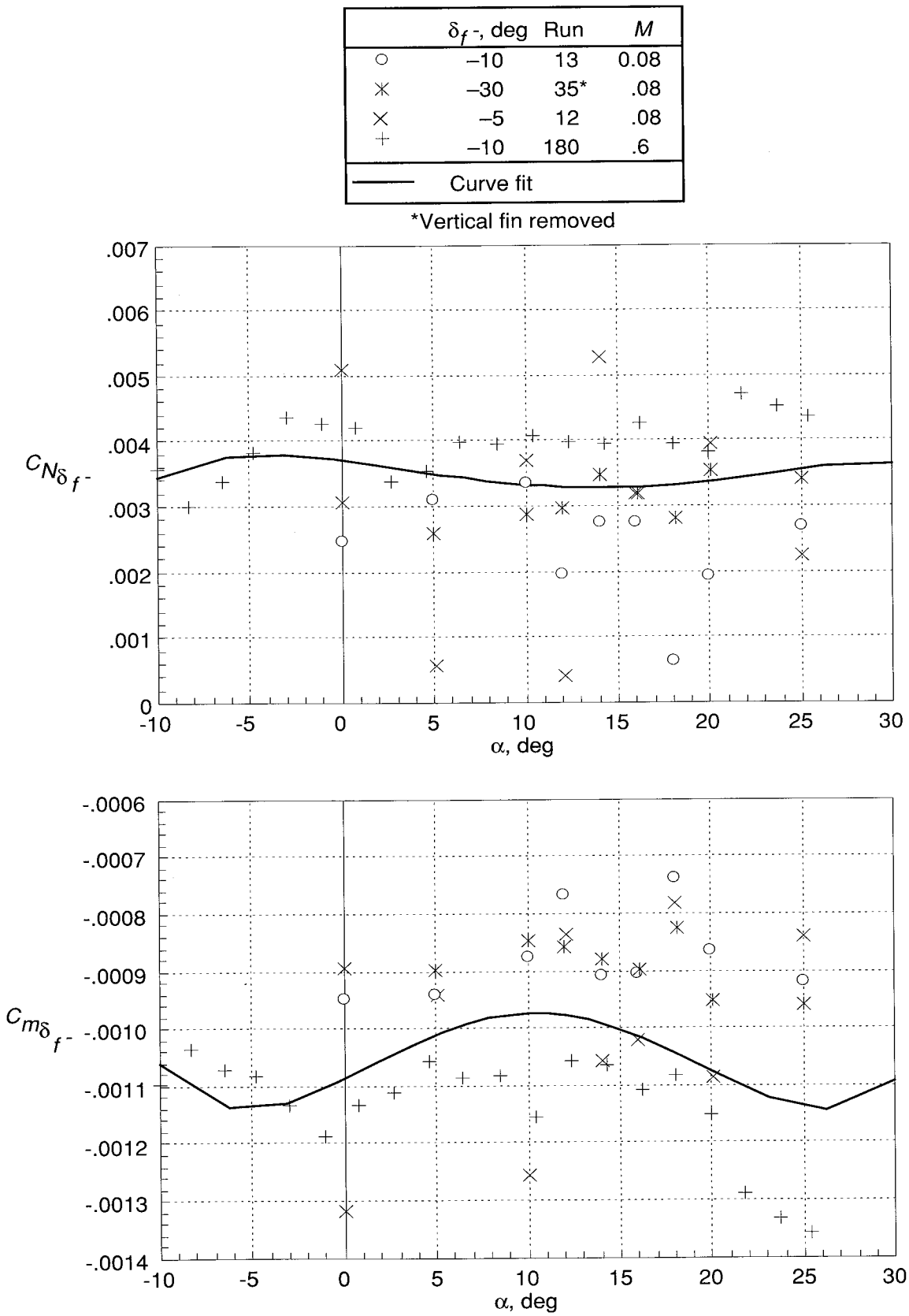

Figure 16. Effect of negative body flaps on aerodynamic characteristics.

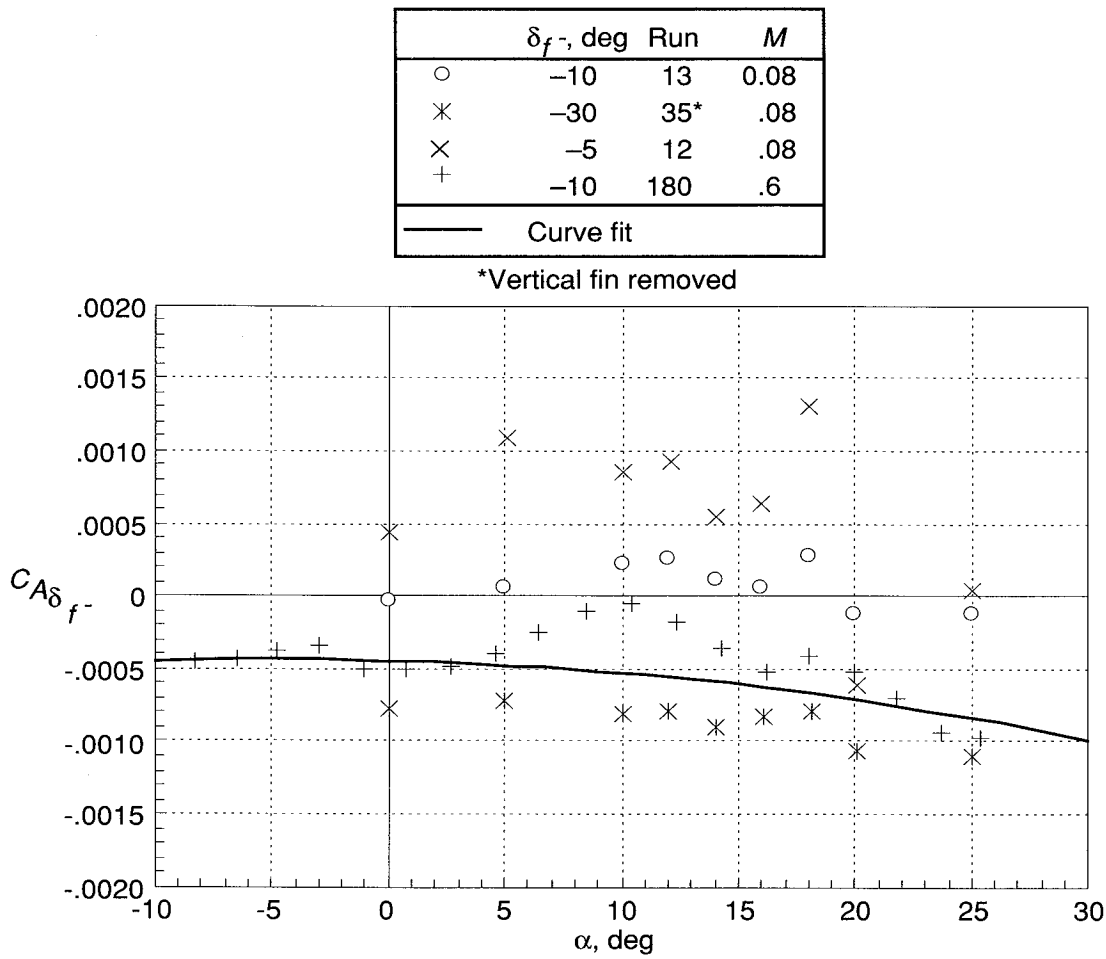

Figure 16. Concluded.

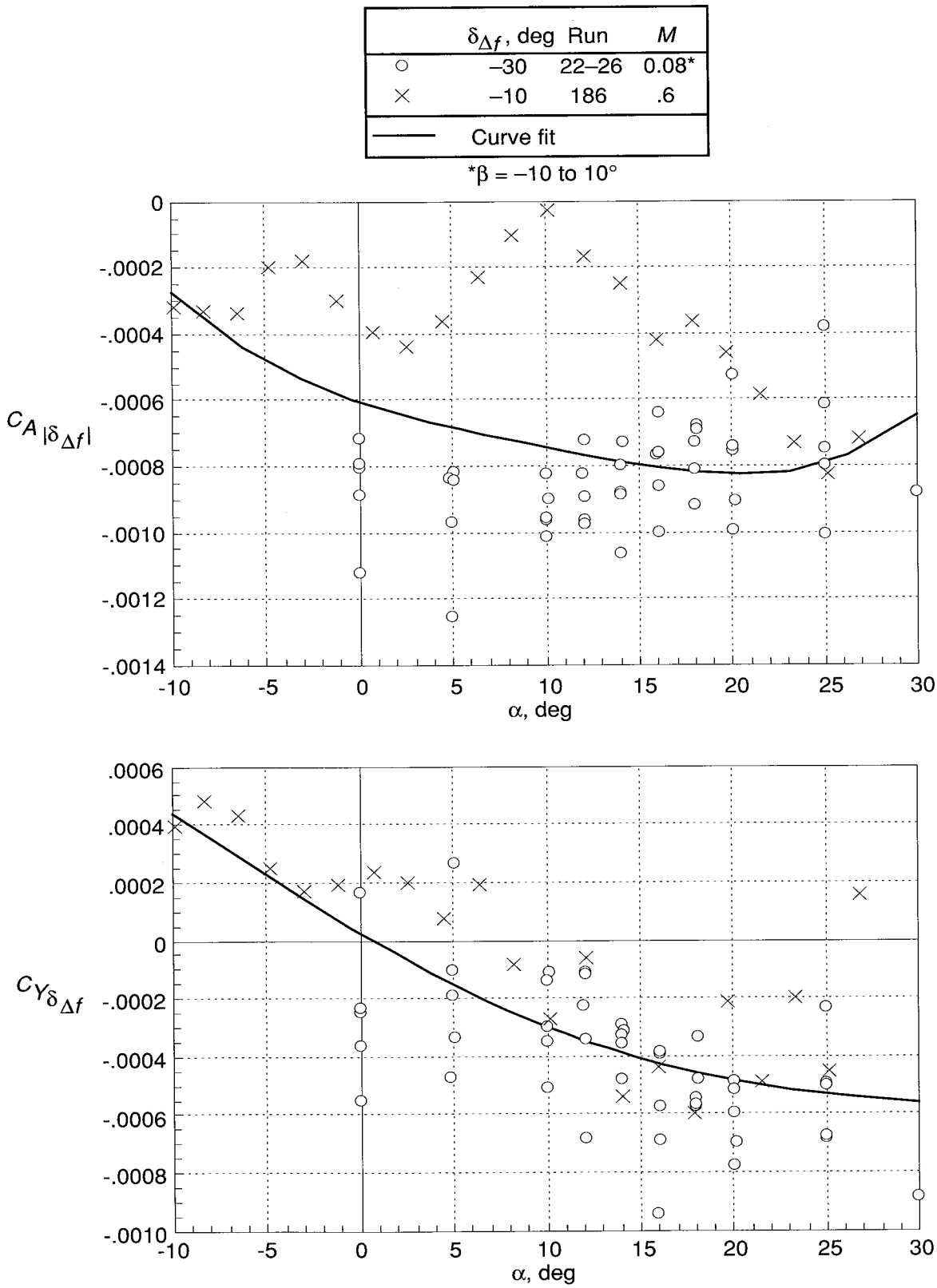

Figure 17. Effect of differential body flaps on aerodynamic characteristics.

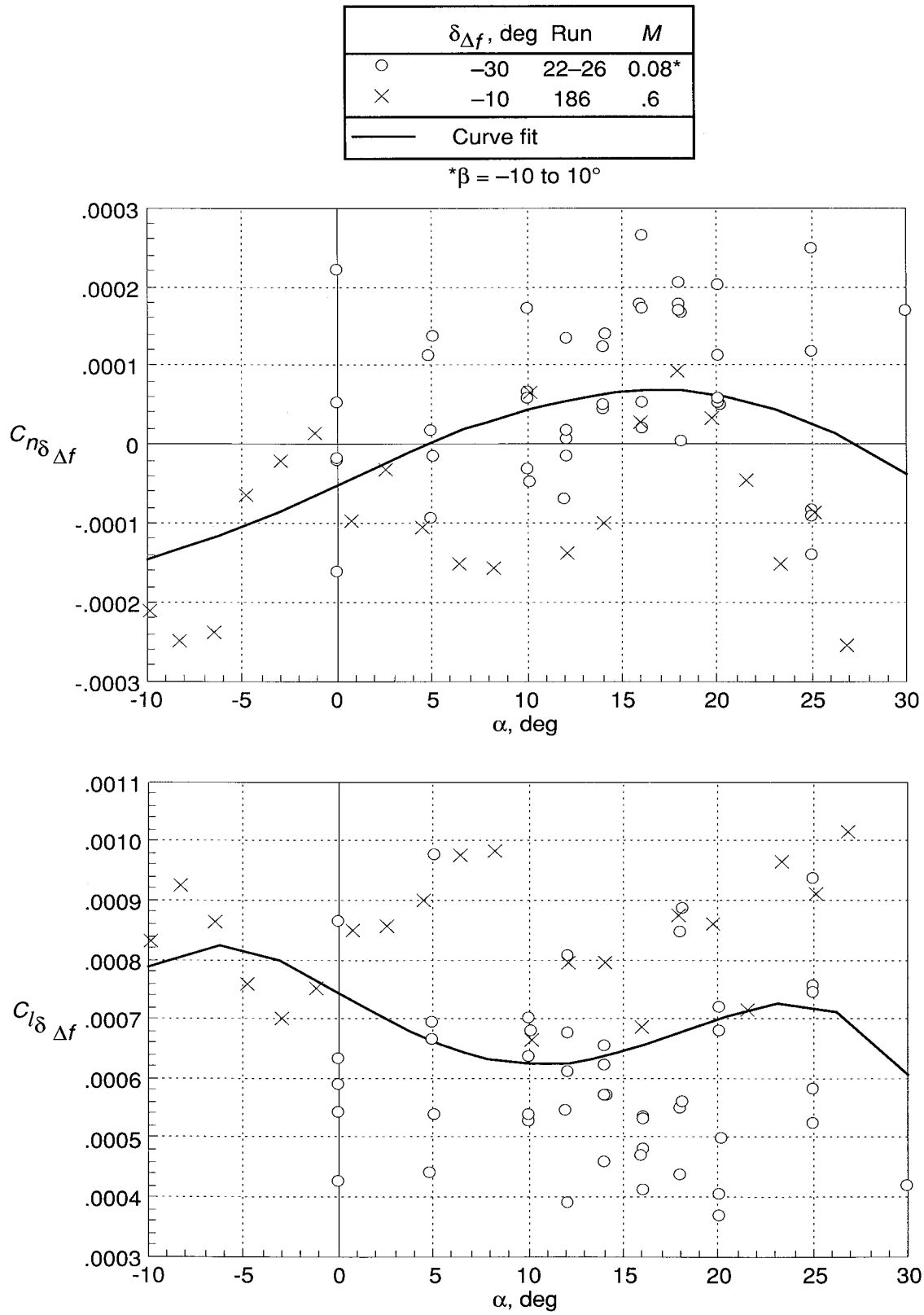

Figure 17. Concluded.

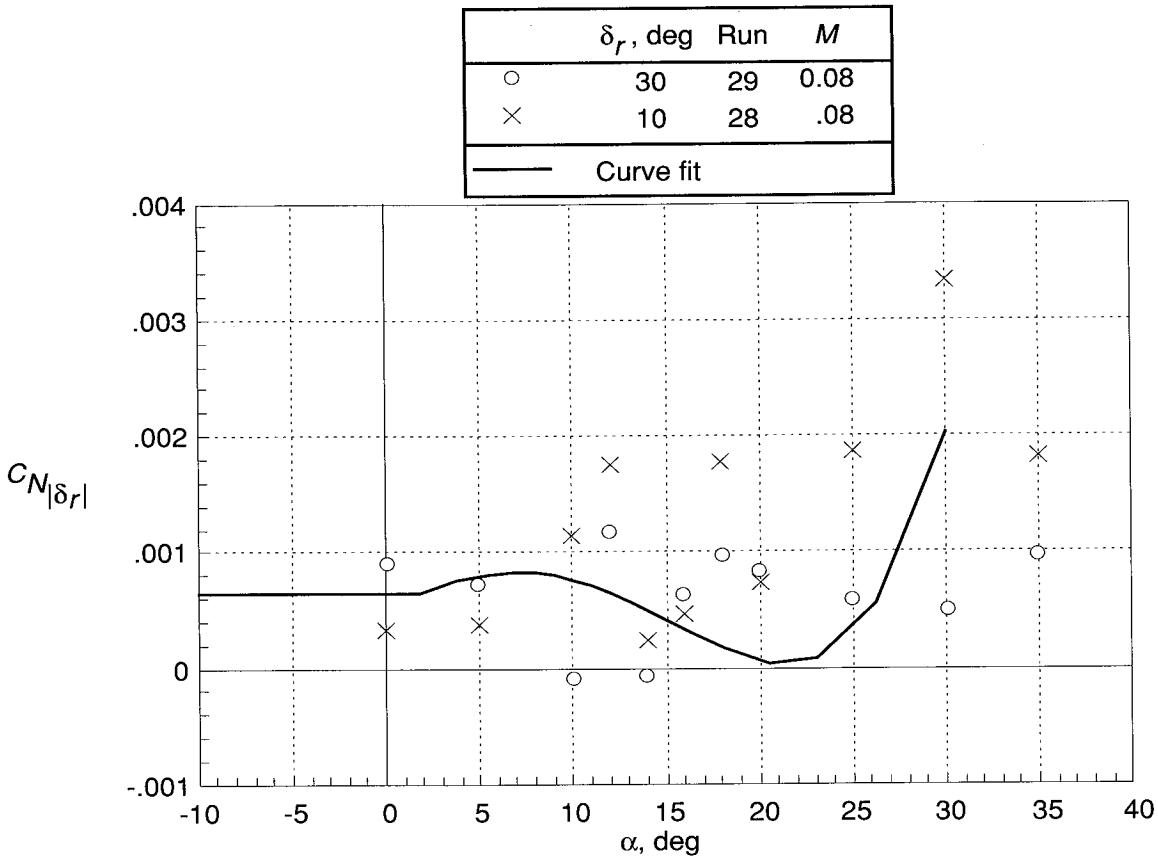

(a) $C_{N_{|\delta_r|}}$ versus α. $C_{N_{|\delta_r|}}$ is assumed insignificant and is not included in the HL-20 aerodynamic model.

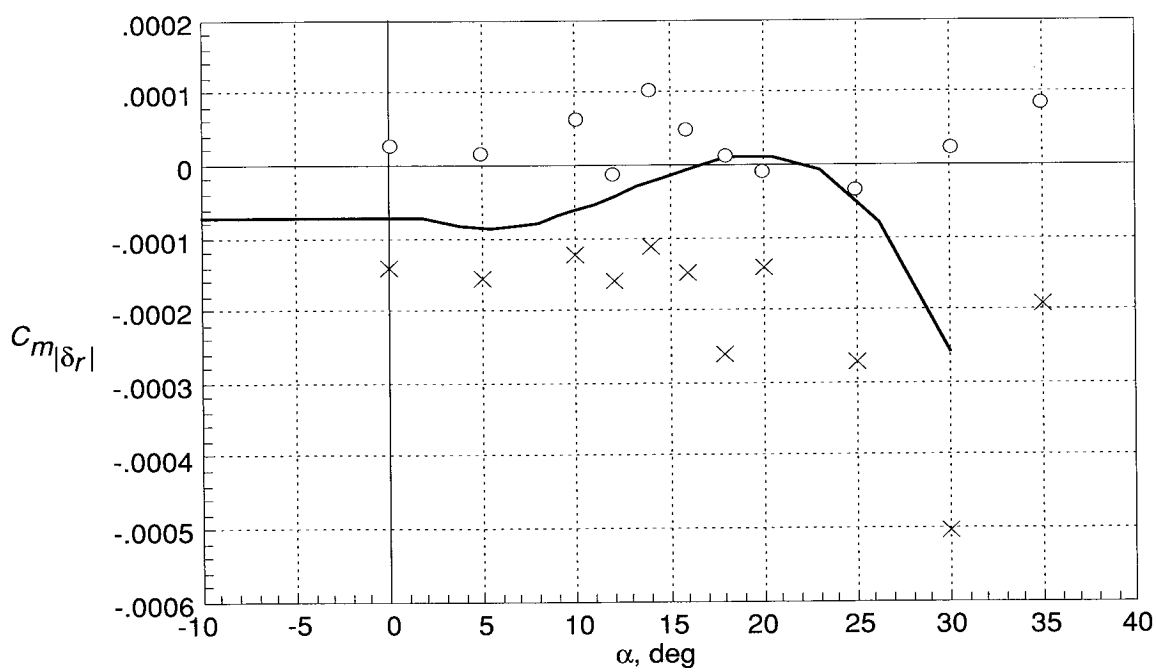

(b) $C_{m_{|\delta_r|}}$ versus α. $C_{m_{|\delta_r|}}$ is assumed insignificant and is not included in the HL-20 aerodynamic model.

Figure 18. Effects of all-movable rudder on aerodynamic characteristics.

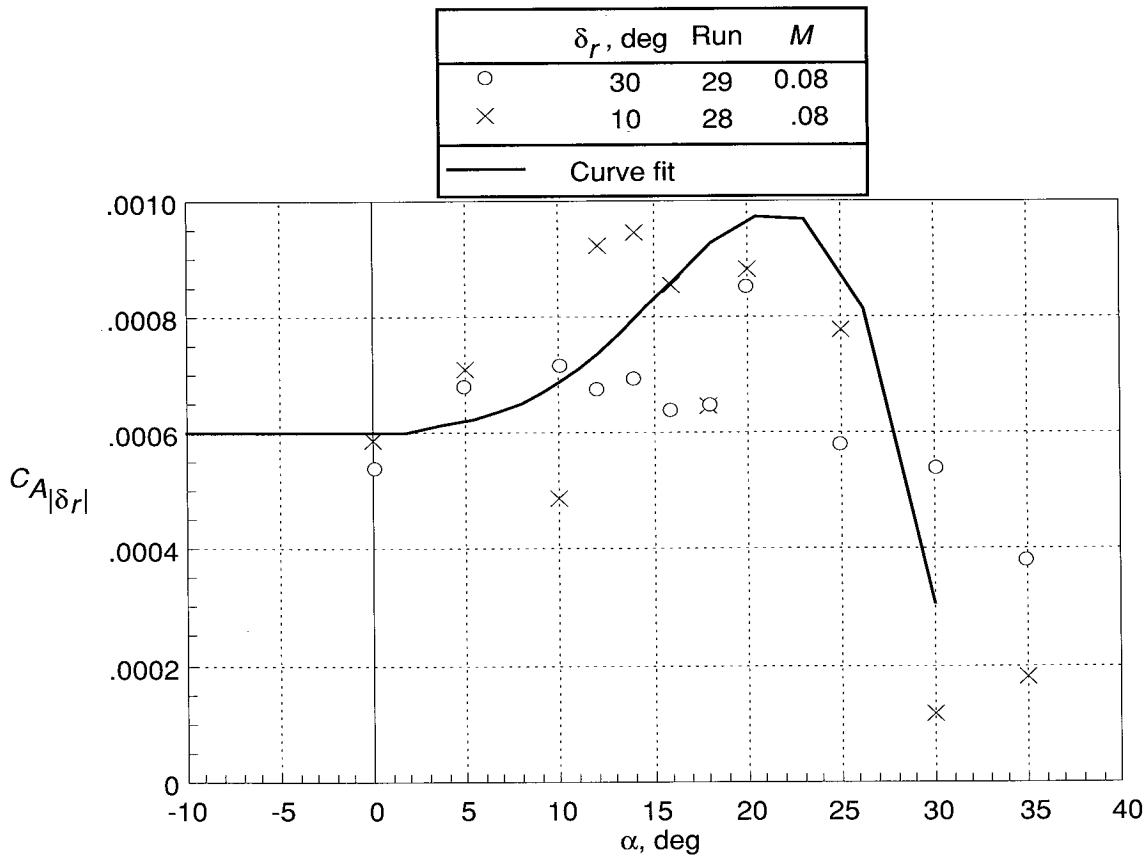

(c) $C_{A_{|\delta_r|}}$ versus α.

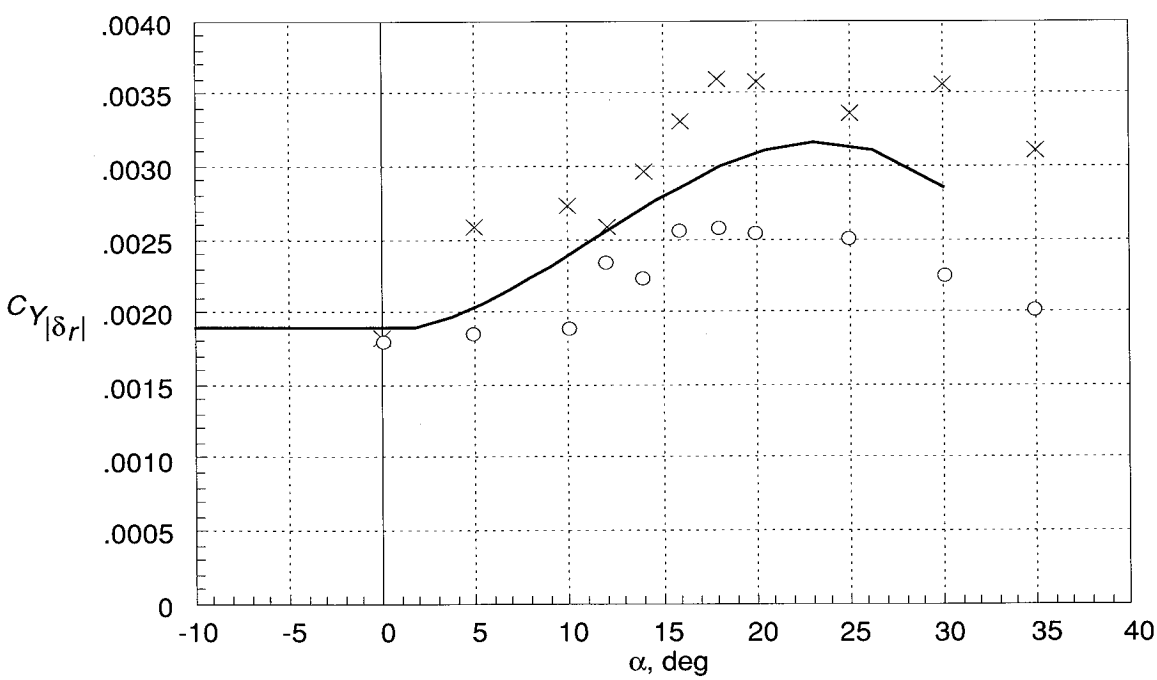

(d) $C_{Y_{|\delta_r|}}$ versus α.

Figure 18. Continued.

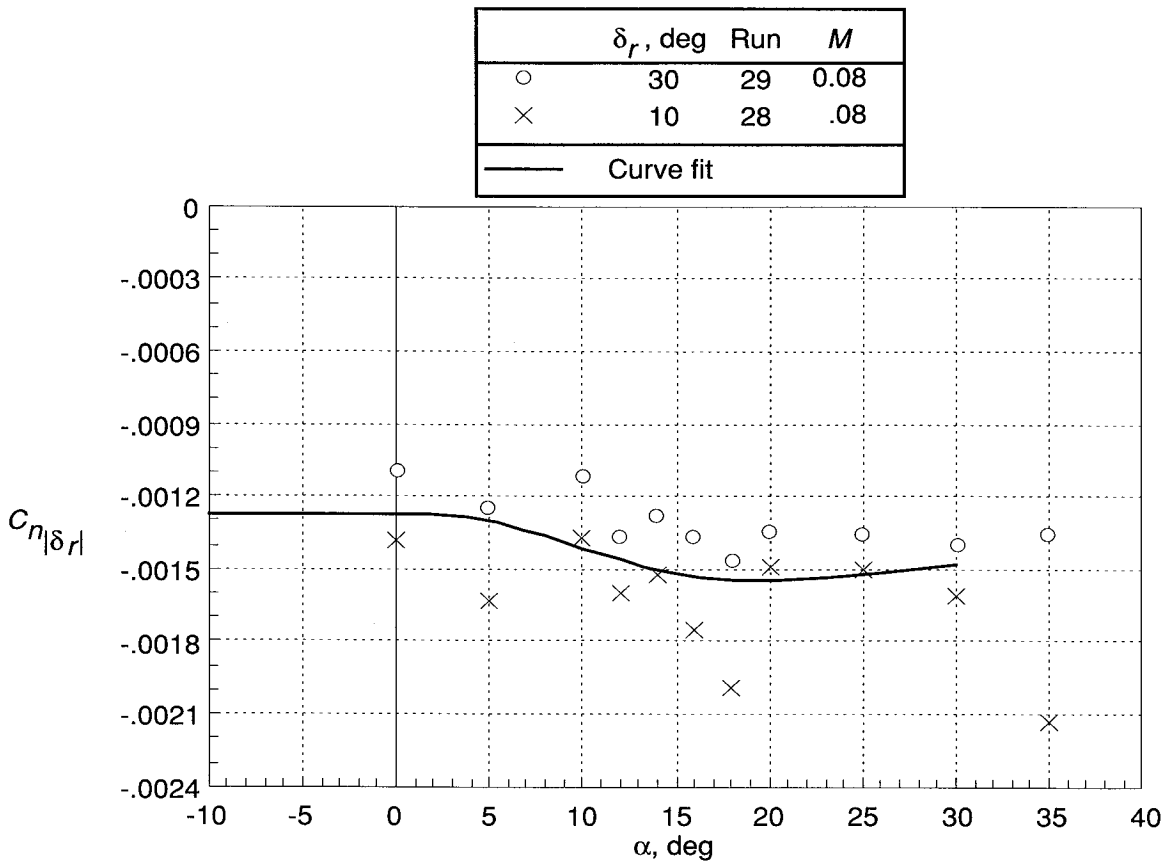

(e) $C_{n_{|\delta_r|}}$ versus α.

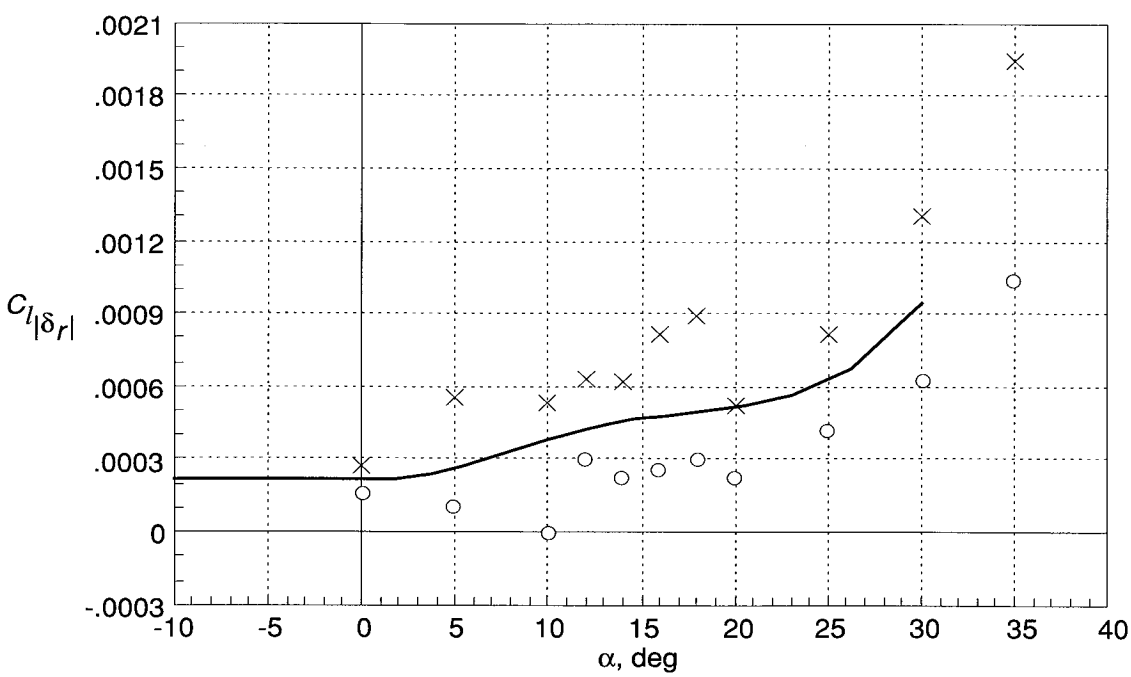

(f) $C_{l_{|\delta_r|}}$ versus α.

Figure 18. Concluded.

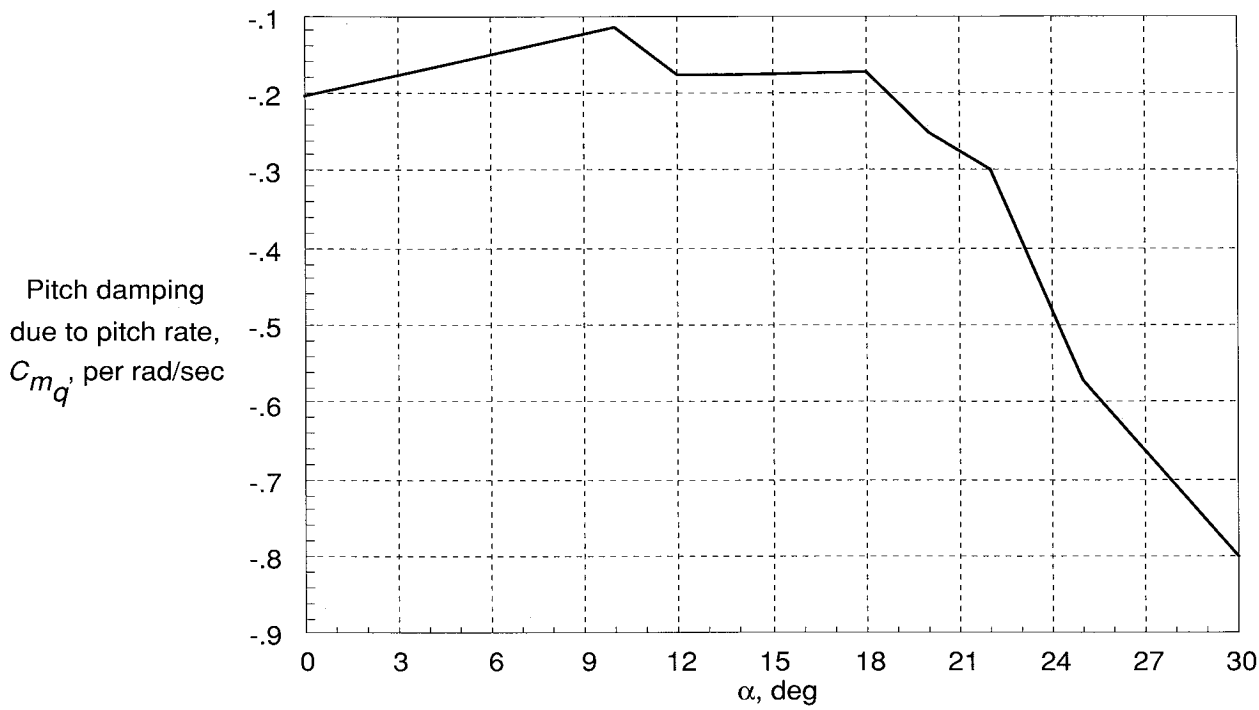

(a) C_{m_q} versus α.

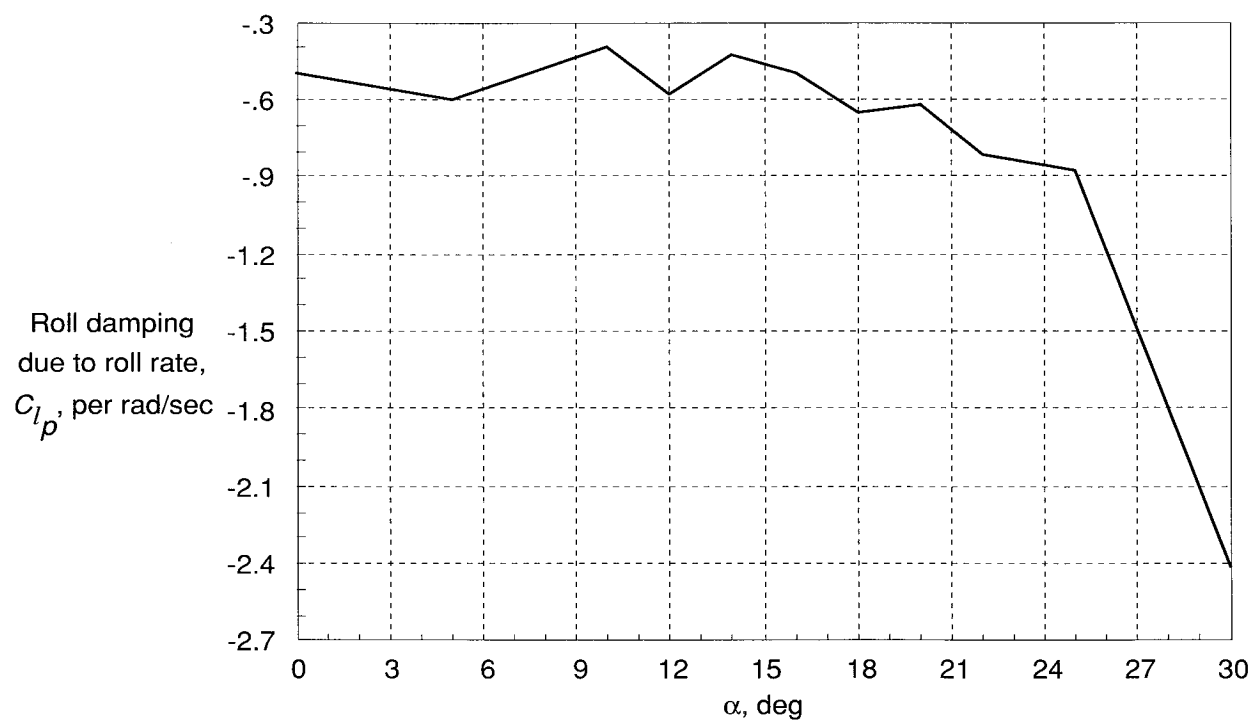

(b) C_{l_p} versus α.

Figure 19. Predicted dynamic derivatives generated with APAS.

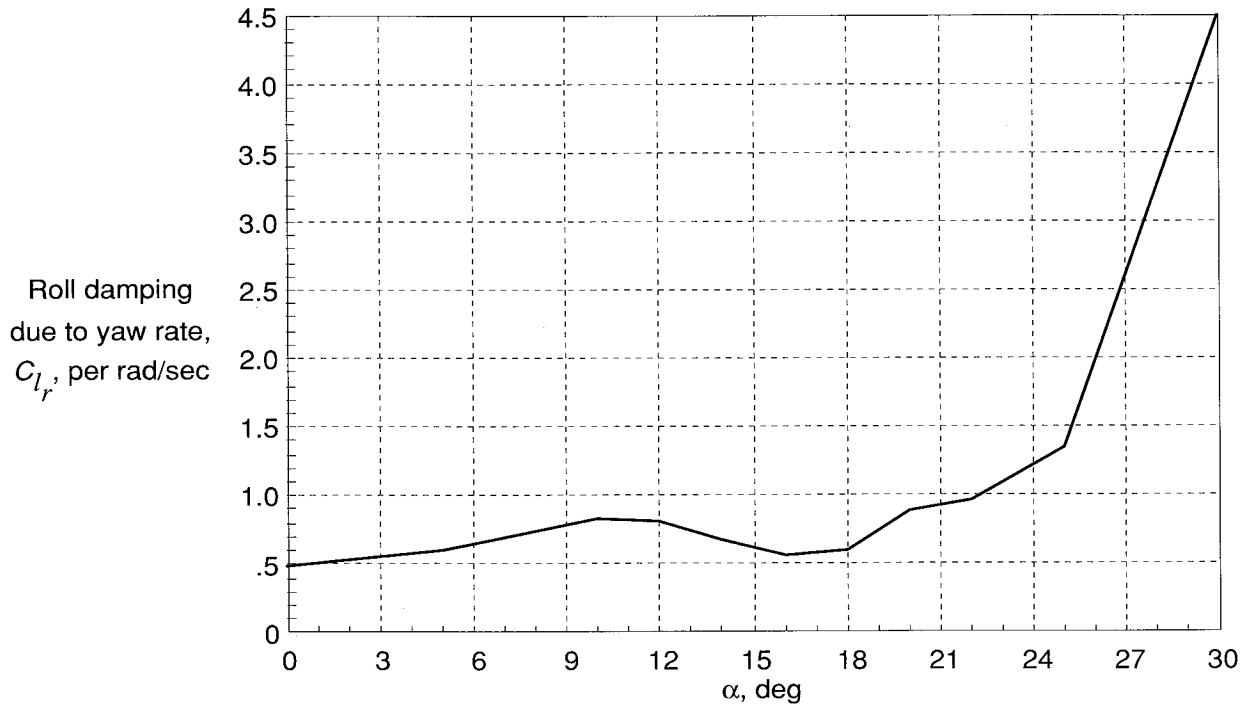

(c) C_{l_r} versus α.

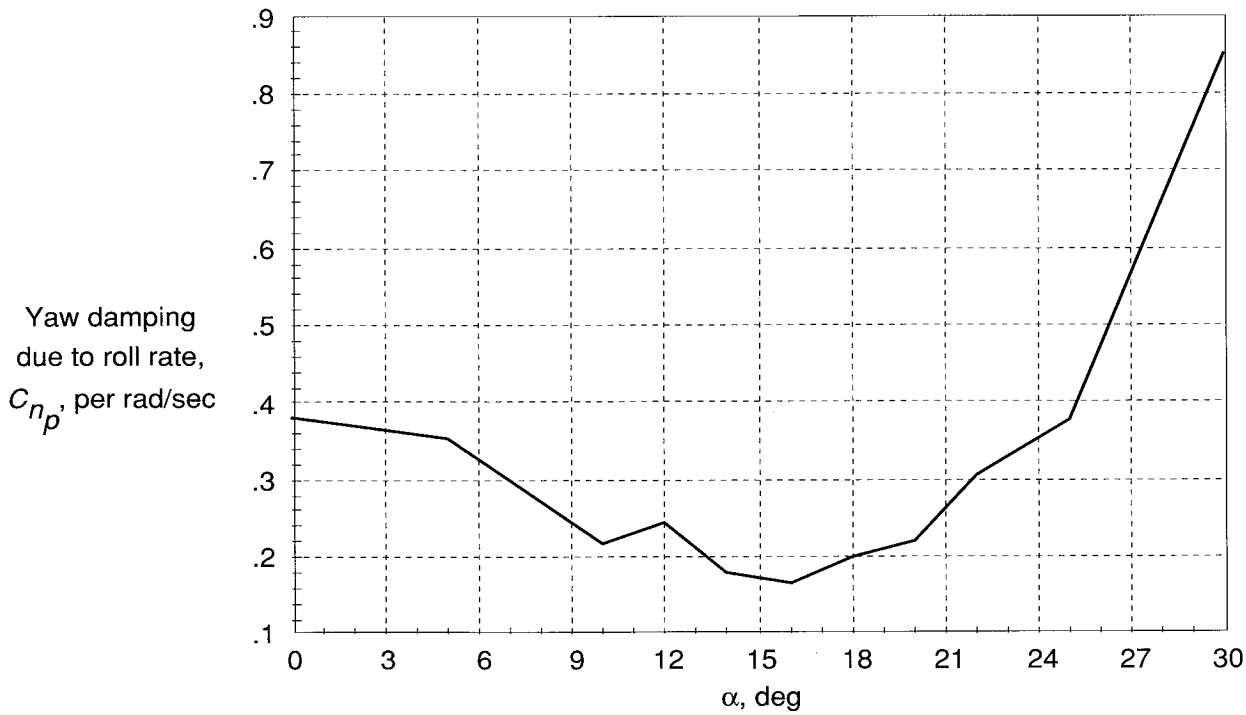

(d) C_{n_p} versus α.

Figure 19. Continued.

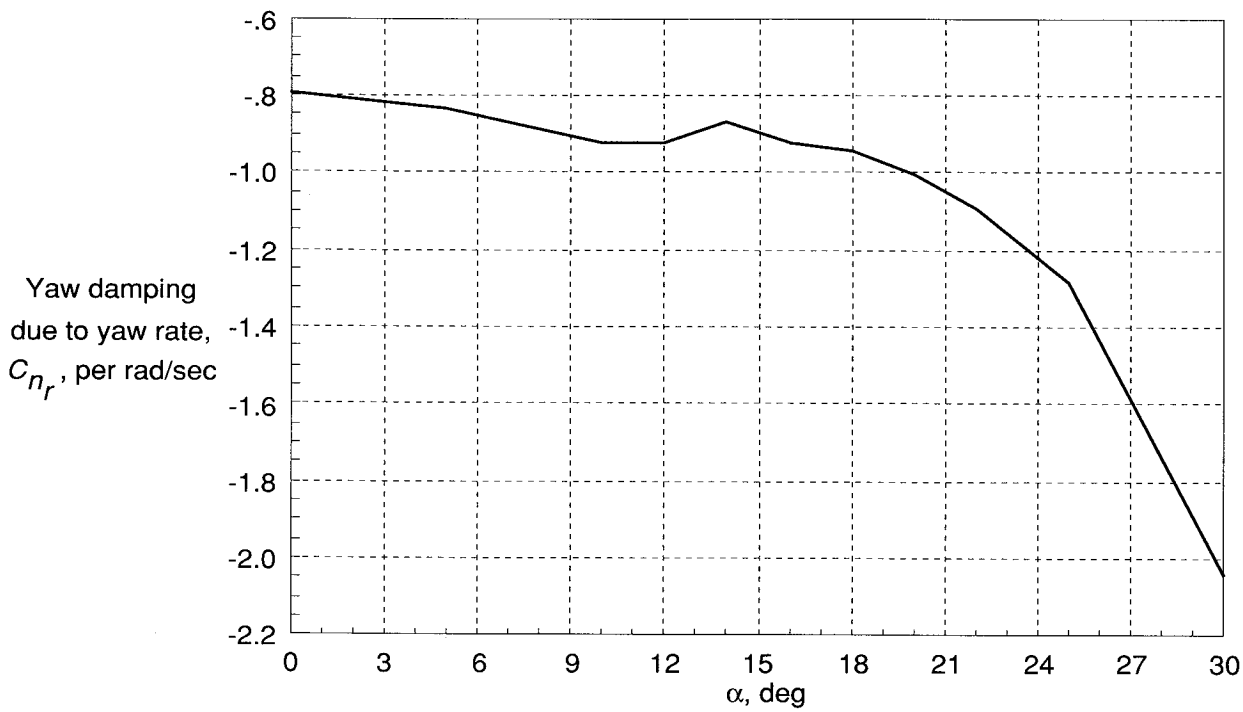

(e) C_{n_r} versus α.

Figure 19. Concluded.

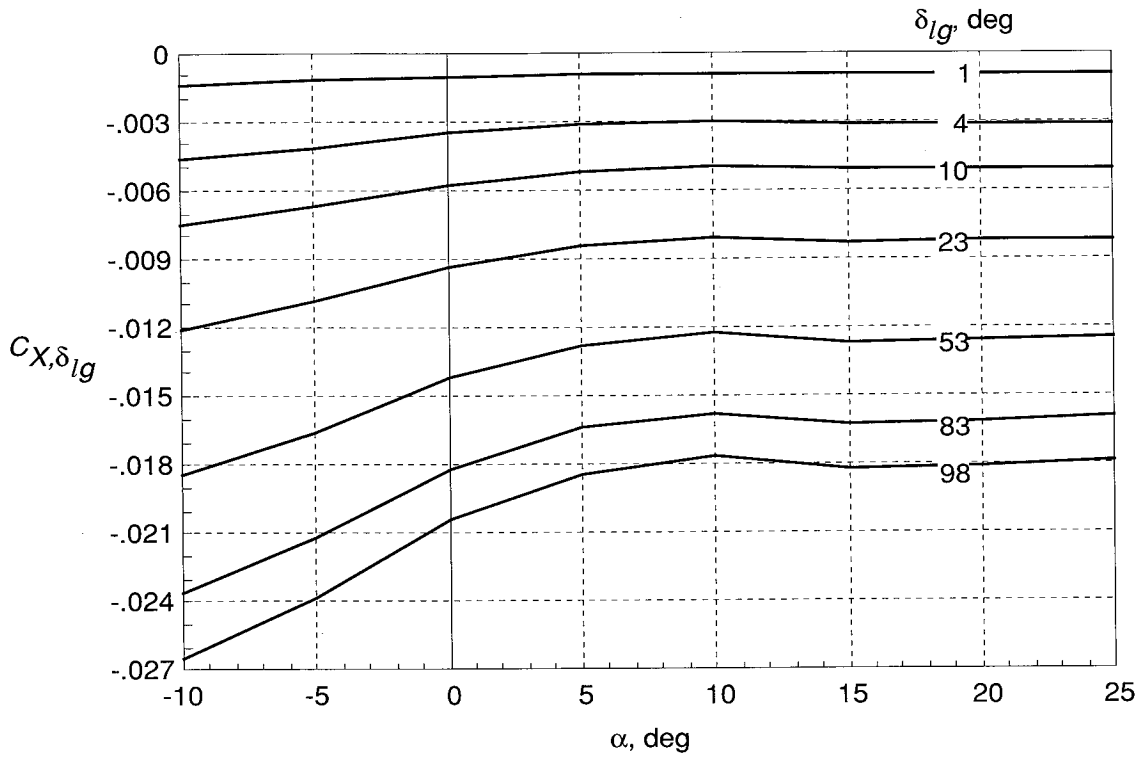

(a) $C_{X,\delta_{lg}}$ versus α.

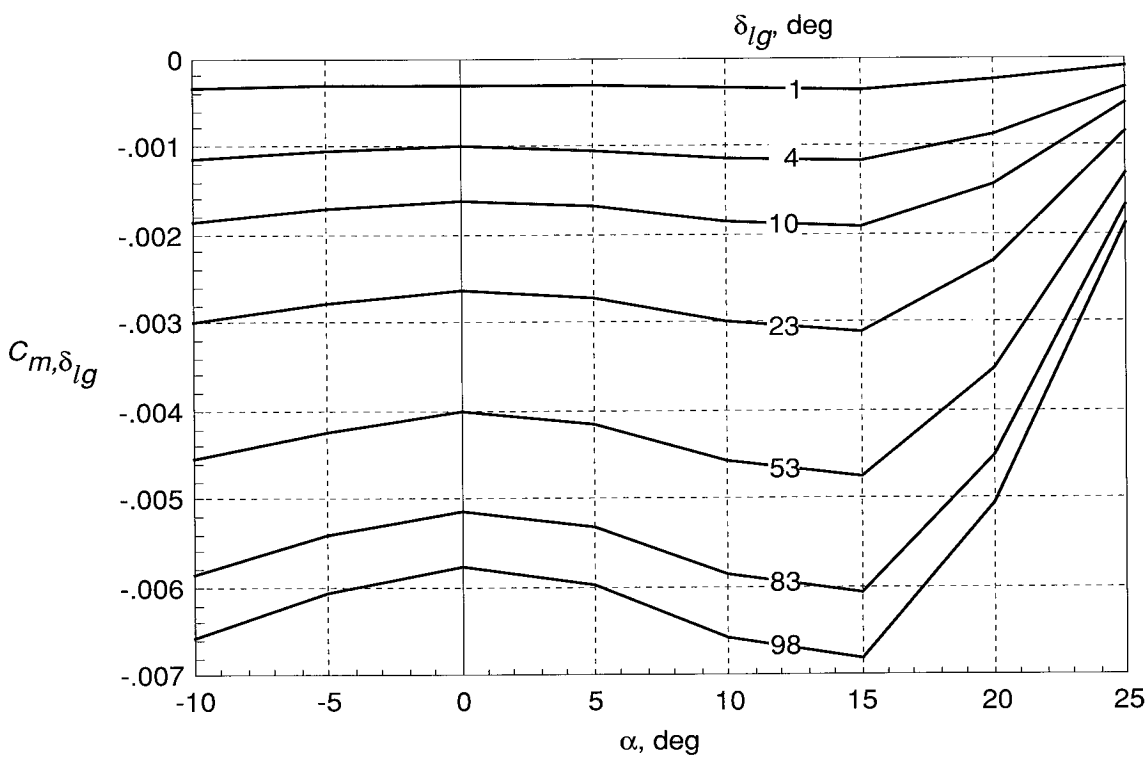

(b) $C_{m,\delta_{lg}}$ versus α.

Figure 20. Landing-gear increments (scaled from data from Space Shuttle aerodynamic models).

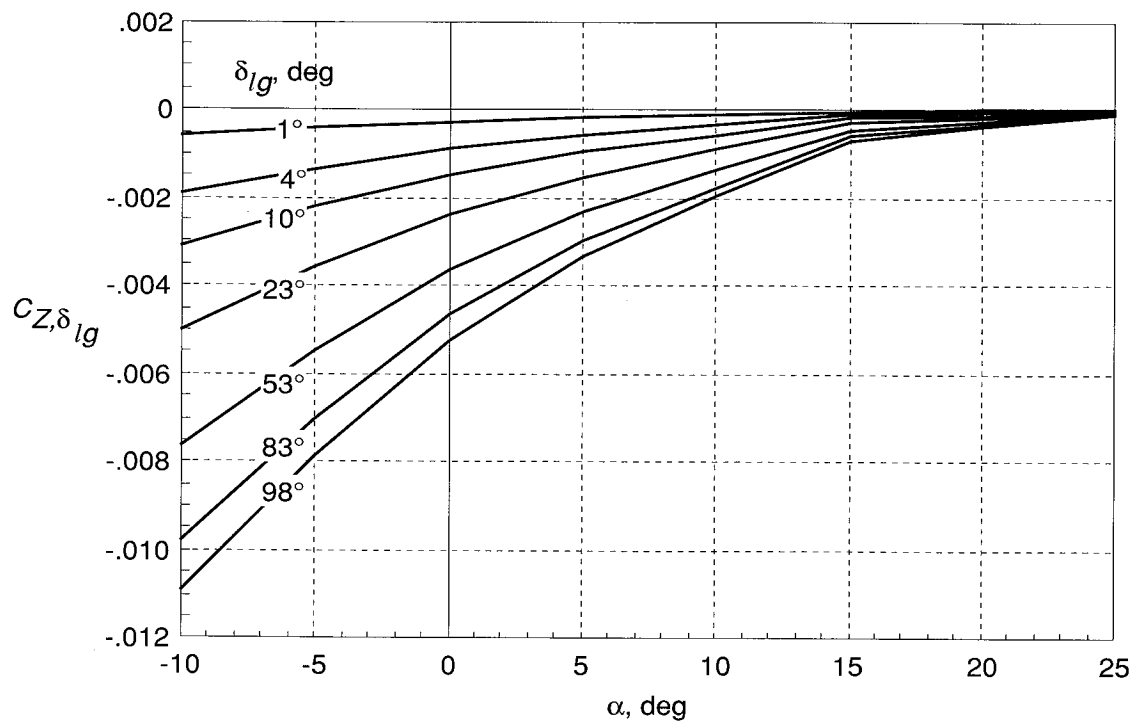

(c) $C_{Z,\delta_{lg}}$ versus α.

Figure 20. Concluded.

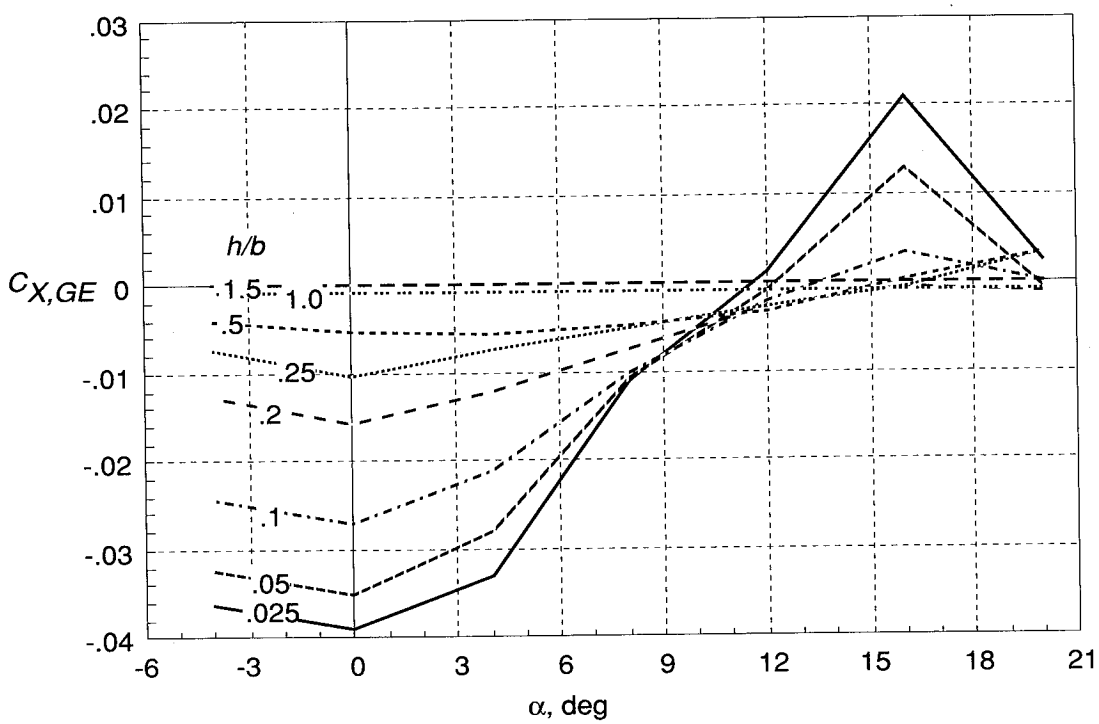

(a) $C_{X,GE}$ versus α.

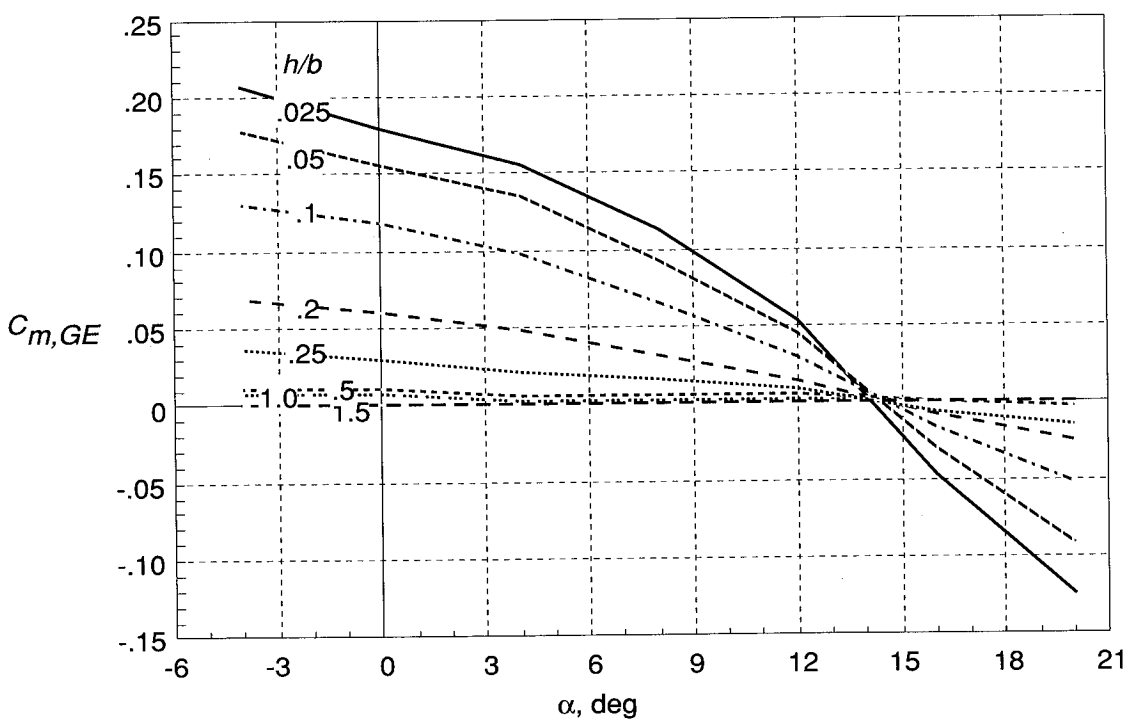

(b) $C_{m,GE}$ versus α.

Figure 21. Ground effect increments (scaled from data from Space Shuttle aerodynamic models).

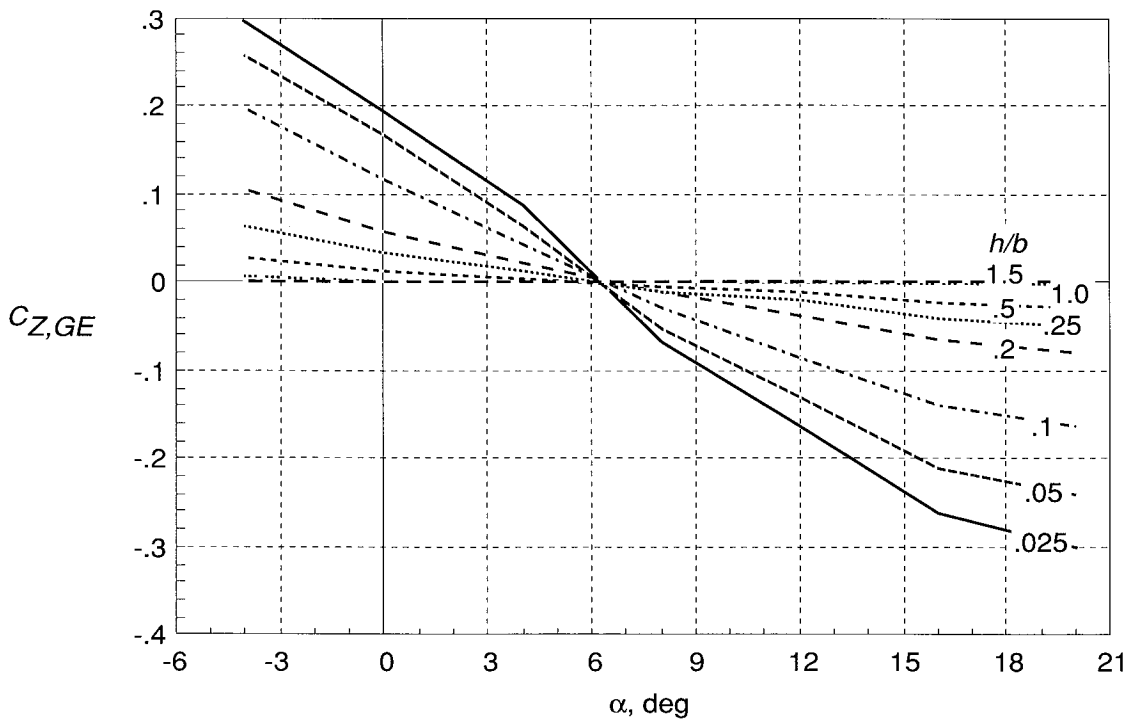

(c) $C_{Z,GE}$ versus α.

Figure 21. Concluded.

Appendix

Data Tables

This appendix contains tabular listings of values used in the preliminary HL-20 real-time simulation at Langley Research Center. These listings represent the functions given in polynomial form in the body of this report and include the scaled Space Shuttle orbiter landing-gear and ground effects data, as well as the predicted dynamic derivatives generated with APAS. Data are presented as follows:

	Table
X Body Axis Force Coefficient for Basic Configuration	A1
Pitching-Moment Coefficient for Basic Configuration	A2
Z Body Axis Force Coefficient for Basic Configuration	A3
Yawing-Moment Coefficient for Basic Configuration	A4
Incremental Force and Moment Coefficients per Degree of Deflection of Symmetric Wing Flap	A5
Incremental Force and Moment Coefficients per Degree of Deflection of Differential Wing Flap	A6
Incremental Force and Moment Coefficients per Degree of Deflection of Positive Body Flap	A7
Incremental Force and Moment Coefficients per Degree of Deflection of Negative Body Flap	A8
Incremental Force and Moment Coefficients per Degree of Deflection of Differental Body Flap	A9
Incremental Force and Moment Coefficients per Degree of Deflection of All-Movable Rudder	A10
Dynamic Derivatives	A11
Incremental X Body Axis Force Coefficient due to Deflection of Landing Gear	A12
Incremental Pitching-Moment Coefficient due to Deflection of Landing Gear	A13
Incremental Z Body Axis Force Coefficient due to Deflection of Landing Gear	A14
Incremental X Body Axis Force Coefficient due to Ground Effect	A15
Incremental Pitching-Moment Coefficient due to Ground Effect	A16
Incremental Z Body Axis Force Coefficient due to Ground Effect	A17

Table A1. X Body Axis Force Coefficient for Basic Configuration

α, deg	$C_{X,o}$ for β, deg, of—							
	−10.00	−7.50	−5.46	−3.84	−2.56	−1.55	−0.73	0
−10.00	-3.81×10^{-2}	-4.24×10^{-2}	-4.59×10^{-2}	-4.97×10^{-2}	-5.32×10^{-2}	-5.60×10^{-2}	-5.82×10^{-2}	-5.97×10^{-2}
−6.50	−5.01	−5.32	−5.58	−5.89	−6.18	−6.42	−6.59	−6.71
−3.03	−5.99	−6.19	−6.36	−6.59	−6.83	−7.02	−7.16	−7.25
0.38	−6.53	−6.63	−6.70	−6.86	−7.04	−7.19	−7.29	−7.35
3.71	−6.57	−6.56	−6.55	−6.64	−6.76	−6.86	−6.93	−6.96
6.93	−6.14	−6.03	−5.93	−5.95	−6.02	−6.08	−6.12	−6.11
10.01	−5.36	−5.14	−4.96	−4.92	−4.94	−4.96	−4.96	−4.93
12.94	−4.36	−4.05	−3.79	−3.69	−3.66	−3.64	−3.61	−3.55
15.67	−3.29	−2.89	−2.56	−2.40	−2.33	−2.27	−2.21	−2.13
18.21	−2.27	−1.79	−1.39	−1.18	−1.06	−0.98	−0.89	−0.78
20.51	−1.39	−0.83	−0.38	−0.11	0.04	0.16	0.27	0.40
22.57	−0.68	−0.06	0.45	0.75	0.94	1.09	1.22	1.37
24.36	−0.17	0.51	1.06	1.41	1.63	1.79	1.95	2.12
25.88	0.16	0.89	1.49	1.86	2.11	2.29	2.46	2.65
27.11	0.36	1.13	1.76	2.16	2.42	2.62	2.81	3.00
28.04	0.46	1.26	1.91	2.33	2.61	2.82	3.02	3.22
28.67	0.49	1.31	1.98	2.42	2.71	2.93	3.13	3.34
28.98	0.51	1.34	2.01	2.45	2.75	2.98	3.18	3.39
29.06	0.51	1.34	2.02	2.46	2.76	2.99	3.19	3.40
29.38	0.51	1.35	2.04	2.49	2.79	3.02	3.23	3.45
30.00	0.50	1.37	2.07	2.53	2.84	3.08	3.30	3.52

Table A1. Concluded

α, deg	$C_{X,o}$ for β, deg, of—						
	0.73	1.55	2.56	3.84	5.46	7.50	10.00
−10.00	-5.82×10^{-2}	-5.60×10^{-2}	-5.32×10^{-2}	-4.97×10^{-2}	-4.59×10^{-2}	-4.24×10^{-2}	-3.81×10^{-2}
−6.50	−6.59	−6.42	−6.18	−5.89	−5.58	−5.32	−5.01
−3.03	−7.16	−7.02	−6.83	−6.59	−6.36	−6.19	−5.99
0.38	−7.29	−7.19	−7.04	−6.86	−6.70	−6.63	−6.53
3.71	−6.93	−6.86	−6.76	−6.64	−6.55	−6.56	−6.57
6.93	−6.12	−6.08	−6.02	−5.95	−5.93	−6.03	−6.14
10.01	−4.96	−4.96	−4.94	−4.92	−4.96	−5.14	−5.36
12.94	−3.61	−3.64	−3.66	−3.69	−3.79	−4.05	−4.36
15.67	−2.21	−2.27	−2.33	−2.40	−2.56	−2.89	−3.29
18.21	−0.89	−0.98	−1.06	−1.18	−1.39	−1.79	−2.27
20.51	0.27	0.16	0.04	−0.11	−0.38	−0.83	−1.39
22.57	1.22	1.09	0.94	0.75	0.45	−0.06	−0.68
24.36	1.95	1.79	1.63	1.41	1.06	0.51	−0.17
25.88	2.46	2.29	2.11	1.86	1.49	0.89	0.16
27.11	2.81	2.62	2.42	2.16	1.76	1.13	0.36
28.04	3.02	2.82	2.61	2.33	1.91	1.26	0.46
28.67	3.13	2.93	2.71	2.42	1.98	1.31	0.49
28.98	3.18	2.98	2.75	2.45	2.01	1.34	0.51
29.06	3.19	2.99	2.76	2.46	2.02	1.34	0.51
29.38	3.23	3.02	2.79	2.49	2.04	1.35	0.51
30.00	3.30	3.08	2.84	2.53	2.07	1.37	0.50

Table A2. Pitching-Moment Coefficient for Basic Configuration

α, deg	$C_{m,o}$ for β, deg, of—							
	−10.00	−7.50	−5.46	−3.84	−2.56	−1.55	−0.73	0
−10.00	38.07×10^{-3}	40.27×10^{-3}	42.89×10^{-3}	44.91×10^{-3}	46.36×10^{-3}	47.43×10^{-3}	48.29×10^{-3}	49.09×10^{-3}
−6.50	31.39	33.07	35.25	36.93	38.11	38.96	39.65	40.29
−3.03	26.10	27.25	29.01	30.35	31.25	31.90	32.41	32.90
0.38	20.74	21.37	22.71	23.71	24.35	24.79	25.13	25.47
3.71	15.15	15.28	16.20	16.88	17.27	17.50	17.67	17.86
6.93	9.73	9.37	9.89	10.25	10.39	10.42	10.44	10.49
10.01	4.91	4.08	4.23	4.29	4.18	4.03	3.89	3.80
12.94	0.99	−0.28	−0.49	−0.72	−1.05	−1.39	−1.67	−1.89
15.67	−1.92	−3.60	−4.16	−4.66	−5.20	−5.70	−6.12	−6.46
18.21	−3.82	−5.89	−6.76	−7.51	−8.24	−8.90	−9.45	−9.90
20.51	−4.75	−7.17	−8.32	−9.29	−10.21	−11.01	−11.67	−12.22
22.57	−4.74	−7.46	−8.87	−10.05	−11.12	−12.04	−12.81	−13.45
24.36	−3.84	−6.84	−8.47	−9.82	−11.04	−12.07	−12.93	−13.65
25.88	−2.23	−5.46	−7.27	−8.78	−10.11	−11.24	−12.17	−12.96
27.11	−0.17	−3.58	−5.55	−7.17	−8.60	−9.80	−10.79	−11.64
28.04	1.95	−1.60	−3.68	−5.40	−6.90	−8.16	−9.20	−10.08
28.67	3.70	0.05	−2.11	−3.89	−5.44	−6.73	−7.80	−8.72
28.98	4.68	0.98	−1.21	−3.02	−4.60	−5.91	−7.00	−7.93
29.06	4.94	1.23	−0.98	−2.80	−4.37	−5.69	−6.78	−7.71
29.38	6.02	2.26	0.02	−1.83	−3.43	−4.77	−5.88	−6.82
30.00	8.43	4.57	2.25	0.34	−1.31	−2.69	−3.28	−4.79

Table A2. Concluded

α, deg	$C_{m,o}$ for β, deg, of—						
	0.73	1.55	2.56	3.84	5.46	7.50	10.00
−10.00	48.29×10^{-3}	47.43×10^{-3}	46.36×10^{-3}	44.91×10^{-3}	42.89×10^{-3}	40.27×10^{-3}	38.07×10^{-3}
−6.50	39.65	38.96	38.11	36.93	35.25	33.07	31.39
−3.03	32.41	31.90	31.25	30.35	29.01	27.25	26.10
0.38	25.13	24.79	24.35	23.71	22.71	21.37	20.74
3.71	17.67	17.50	17.27	16.88	16.20	15.28	15.15
6.93	10.44	10.42	10.39	10.25	9.89	9.37	9.73
10.01	3.89	4.03	4.18	4.29	4.23	4.08	4.91
12.94	−1.67	−1.39	−1.05	−0.72	−0.49	−0.28	0.99
15.67	−6.12	−5.70	−5.20	−4.66	−4.16	−3.60	−1.92
18.21	−9.45	−8.90	−8.24	−7.51	−6.76	−5.89	−3.82
20.51	−11.67	−11.01	−10.21	−9.29	−8.32	−7.17	−4.75
22.57	−12.81	−12.04	−11.12	−10.05	−8.87	−7.46	−4.74
24.36	−12.93	−12.07	−11.04	−9.82	−8.47	−6.84	−3.84
25.88	−12.17	−11.24	−10.11	−8.78	−7.27	−5.46	−2.23
27.11	−10.79	−9.80	−8.60	−7.17	−5.55	−3.58	−0.17
28.04	−9.20	−8.16	−6.90	−5.40	−3.68	−1.60	1.95
28.67	−7.80	−6.73	−5.44	−3.89	−2.11	0.05	3.70
28.98	−7.00	−5.91	−4.60	−3.02	−1.21	0.98	4.68
29.06	−6.78	−5.69	−4.37	−2.80	−0.98	1.23	4.94
29.38	−5.88	−4.77	−3.43	−1.83	0.02	2.26	6.02
30.00	−3.82	−2.69	−1.31	0.34	2.25	4.57	8.43

Table A3. Z Body Axis Force Coefficient for Basic Configuration

α, deg	$C_{Z,o}$ for β, deg, of—							
	−10.00	−7.50	−5.46	−3.84	−2.56	−1.55	−0.73	0
−10.00	4.48×10^{-1}	4.61×10^{-1}	4.76×10^{-1}	4.91×10^{-1}	5.04×10^{-1}	5.13×10^{-1}	5.21×10^{-1}	5.26×10^{-1}
−6.50	3.00	3.08	3.20	3.32	3.42	3.50	3.56	3.61
−3.03	1.70	1.74	1.82	1.92	2.00	2.06	2.11	2.14
0.38	0.47	0.47	0.52	0.59	0.65	0.69	0.73	0.75
3.71	−0.73	−0.77	−0.76	−0.71	−0.68	−0.65	−0.63	−0.62
6.93	−1.91	−2.00	−2.01	−1.99	−1.97	−1.96	−1.96	−1.96
10.01	−3.05	−3.17	−3.22	−3.23	−3.23	−3.23	−3.23	−3.25
12.94	−4.12	−4.27	−4.34	−4.38	−4.39	−4.41	−4.43	−4.45
15.67	−5.07	−5.26	−5.36	−5.41	−5.45	−5.48	−5.51	−5.54
18.21	−5.90	−6.12	−6.25	−6.32	−6.37	−6.41	−6.45	−6.50
20.51	−6.60	−6.85	−7.00	−7.09	−7.15	−7.21	−7.26	−7.31
22.57	−7.17	−7.44	−7.61	−7.72	−7.80	−7.86	−7.92	−7.97
24.36	−7.62	−7.91	−8.10	−8.22	−8.31	−8.38	−8.45	−8.51
25.88	−7.96	−8.27	−8.48	−8.61	−8.71	−8.79	−8.86	−8.93
27.11	−8.22	−8.54	−8.76	−8.90	−9.01	−9.09	−9.17	−9.24
28.04	−8.39	−8.73	−8.96	−9.11	−9.22	−9.31	−9.39	−9.46
28.67	−8.51	−8.85	−9.08	−9.24	−9.35	−9.45	−9.53	−9.61
28.98	−8.56	−8.91	−9.14	−9.30	−9.42	−9.52	−9.60	−9.68
29.06	−8.57	−8.93	−9.16	−9.32	−9.44	−9.53	−9.61	−9.70
29.38	−8.63	−8.98	−9.22	−9.38	−9.50	−9.60	−9.68	−9.76
30.00	−8.73	−9.09	−9.33	−9.50	−9.63	−9.73	−9.81	−9.90

Table A3. Concluded

α, deg	$C_{Z,o}$ for β, deg, of—						
	0.73	1.55	2.56	3.84	5.46	7.50	10.00
−10.00	5.21×10^{-1}	5.13×10^{-1}	5.04×10^{-1}	4.91×10^{-1}	4.76×10^{-1}	4.61×10^{-1}	4.48×10^{-1}
−6.50	3.56	3.50	3.42	3.32	3.20	3.08	3.00
−3.03	2.11	2.06	2.00	1.92	1.82	1.74	1.70
0.38	0.73	0.69	0.65	0.59	0.52	0.47	0.47
3.71	−0.63	−0.65	−0.68	−0.71	−0.76	−0.77	−0.73
6.93	−1.96	−1.96	−1.97	−1.99	−2.01	−2.00	−1.91
10.01	−3.23	−3.23	−3.23	−3.23	−3.22	−3.17	−3.05
12.94	−4.43	−4.41	−4.39	−4.38	−4.34	−4.27	−4.12
15.67	−5.51	−5.48	−5.45	−5.41	−5.36	−5.26	−5.07
18.21	−6.45	−6.41	−6.37	−6.32	−6.25	−6.12	−5.90
20.51	−7.26	−7.21	−7.15	−7.09	−7.00	−6.85	−6.60
22.57	−7.92	−7.86	−7.80	−7.72	−7.61	−7.44	−7.17
24.36	−8.45	−8.38	−8.31	−8.22	−8.10	−7.91	−7.62
25.88	−8.86	−8.79	−8.71	−8.61	−8.48	−8.27	−7.96
27.11	−9.17	−9.09	−9.01	−8.90	−8.76	−8.54	−8.22
28.04	−9.39	−9.31	−9.22	−9.11	−8.96	−8.73	−8.39
28.67	−9.53	−9.45	−9.35	−9.24	−9.08	−8.85	−8.51
28.98	−9.60	−9.52	−9.42	−9.30	−9.14	−8.91	−8.56
29.06	−9.61	−9.53	−9.44	−9.32	−9.16	−8.93	−8.57
29.38	−9.68	−9.60	−9.50	−9.38	−9.22	−8.98	−8.63
30.00	−9.81	−9.73	−9.63	−9.50	−9.33	−9.09	−8.73

Table A4. Yawing-Moment Coefficient for Basic Configuration

α, deg	$C_{n,o}$ for β, deg, of—						
	−10	−5	−2	0	2	5	10
−10	-2.30×10^{-2}	-1.15×10^{-2}	-0.46×10^{-2}	0	0.46×10^{-2}	1.15×10^{-2}	2.30×10^{-2}
−5	−2.80	−1.40	−0.56	↓	0.56	1.40	2.80
0	−4.00	−2.00	−1.00	↓	1.00	2.00	4.00
5	−3.00	−1.40	−0.50	↓	0.50	1.40	3.00
10	−3.00	−1.80	−0.80	↓	0.80	1.80	3.00
15	−3.00	−1.50	−0.60	↓	0.60	1.50	3.00
20	−1.20	−1.00	−0.70	↓	0.70	1.00	1.20
25	−0.99	−0.53	−0.17	↓	0.17	0.53	0.99
30	−0.02	0.24	0.29	↓	−0.29	−0.24	0.02

Table A5. Incremental Force and Moment Coefficients per Degree of Deflection of Symmetric Wing Flap

α, deg	$C_{X_{\delta_e}}$	$C_{m_{\delta_e}}$	$C_{Z_{\delta_e}}$
−10.00	4.43×10^{-4}	-1.55×10^{-3}	-4.13×10^{-3}
−6.29	2.68	−1.71	−4.66
−3.12	2.05	−1.83	−4.97
−0.43	1.87	−1.90	−5.12
1.84	1.82	−1.92	−5.19
3.75	1.78	−1.92	−5.19
5.36	1.72	−1.91	−5.16
6.73	1.63	−1.88	−5.11
7.92	1.52	−1.85	−5.04
8.99	1.38	−1.81	−4.96
10.00	1.22	−1.77	−4.88
11.01	1.03	−1.72	−4.77
12.08	0.78	−1.66	−4.65
13.27	0.47	−1.59	−4.49
14.64	0.05	−1.49	−4.27
16.25	−0.52	−1.37	−3.97
18.16	−1.29	−1.20	−3.55
20.43	−2.29	−0.99	−2.94
23.12	−3.55	−0.71	−2.07
26.29	−4.94	−0.36	−0.77
30.00	−6.10	0.03	1.15

Table A6. Incremental Force and Moment Coefficients per Degree of Deflection of Differential Wing Flap

α, deg	$C_{X_{\lvert\delta_a\rvert}}$	$C_{m_{\lvert\delta_a\rvert}}$	$C_{Y_{\delta_a}}$	$C_{l_{\delta_a}}$	$C_{n_{\delta_a}}$
−10.00	-9.04×10^{-4}	2.08×10^{-4}	3.32×10^{-3}	2.56×10^{-3}	-2.82×10^{-3}
−6.29	↓	↓	↓	↓	↓
−3.12	↓	↓	↓	↓	↓
−0.43	↓	↓	↓	↓	↓
1.84	↓	↓	↓	↓	↓
3.75	−7.92	2.30	3.25	↓	−2.81
5.36	−6.86	2.28	3.18	2.54	−2.77
6.73	−5.96	2.18	3.11	2.51	−2.71
7.92	−5.23	2.06	3.05	2.48	−2.65
8.99	−4.63	1.96	2.98	2.44	−2.59
10.00	−4.14	1.88	2.91	2.40	−2.53
11.01	−3.73	1.82	2.85	2.35	−2.46
12.08	−3.40	1.79	2.77	2.29	−2.39
13.27	−3.15	1.81	2.68	2.22	−2.30
14.64	−3.02	1.89	2.57	2.13	−2.20
16.25	−3.09	2.09	2.44	2.01	−2.09
18.16	−3.43	2.43	2.27	1.86	−1.95
20.43	−4.08	2.93	2.06	1.66	−1.80
23.12	−4.88	3.48	1.81	1.39	−1.62
26.29	−5.20	3.63	1.50	1.04	−1.42
30.00	−3.22	2.21	1.13	0.59	−1.16

Table A7. Incremental Force and Moment Coefficients per Degree of Deflection of Positive Body Flap

α, deg	$C_{X_{\delta_{f^+}}}$	$C_{m_{\delta_{f^+}}}$	$C_{Z_{\delta_{f^+}}}$
−10.00	-2.72×10^{-4}	-9.89×10^{-4}	-3.71×10^{-3}
−6.29	−1.91	−9.90	−3.75
−3.12	−1.46	↓	−3.77
−0.43	−1.31	↓	−3.78
1.84	−1.36	↓	−3.78
3.75	−1.53	↓	−3.77
5.36	−1.75	↓	−3.76
6.73	−1.99	↓	−3.75
7.92	−2.23	−9.89	−3.74
8.99	−2.47	↓	−3.72
10.00	−2.72	↓	−3.71
11.01	−2.98	↓	−3.70
12.08	−3.27	−9.88	−3.68
13.27	−3.59	−9.88	−3.66
14.64	−3.96	−9.87	−3.63
16.25	−4.37	−9.86	−3.60
18.16	−4.79	−9.83	−3.56
20.43	−5.16	−9.79	−3.51
23.12	−5.27	−9.72	−3.44
26.29	−4.76	−9.60	−3.36
30.00	−2.91	−9.40	−3.26

Table A8. Incremental Force and Moment Coefficients per Degree of Deflection of Negative Body Flap

α, deg	$C_{X_{\delta_{f^-}}}$	$C_{m_{\delta_{f^-}}}$	$C_{Z_{\delta_{f^-}}}$
−10.00	4.47×10^{-4}	-10.61×10^{-4}	-3.45×10^{-3}
−6.29	4.34	−11.36	−3.75
−3.12	4.33	−11.28	−3.79
−0.43	4.40	−10.93	−3.73
1.84	4.51	−10.57	−3.64
3.75	4.63	−10.27	−3.55
5.36	4.77	−10.05	−3.48
6.73	4.90	−9.91	−3.43
7.92	5.03	−9.81	−3.38
8.99	5.16	−9.76	−3.35
10.00	5.29	−9.74	−3.32
11.01	5.43	−9.74	−3.30
12.08	5.58	−9.78	−3.29
13.27	5.77	−9.85	−3.28
14.64	6.01	−9.97	−3.28
16.25	6.30	−10.17	−3.29
18.16	6.69	−10.46	−3.33
20.43	7.19	−10.83	−3.40
23.12	7.84	−11.22	−3.49
26.29	8.70	−11.43	−3.59
30.00	9.82	−10.93	−3.65

Table A9. Incremental Force and Moment Coefficients per Degree of Deflection of Differential Body Flap

α, deg	$C_{X_{\lvert\delta_{\Delta f}\rvert}}$	$C_{Y_{\delta_{\Delta f}}}$	$C_{l_{\delta_{\Delta f}}}$	$C_{n_{\delta_{\Delta f}}}$
−10.00	-2.76×10^{-4}	4.35×10^{-4}	7.87×10^{-4}	-14.64×10^{-5}
−6.29	−4.42	2.82	8.25	−11.73
−3.12	−5.37	1.51	7.97	−8.53
−0.43	−5.96	0.43	7.53	−5.58
1.84	−6.36	−0.42	7.12	−3.08
3.75	−6.65	−1.10	6.80	−1.05
5.36	−6.87	−1.64	6.58	0.56
6.73	−7.05	−2.07	6.43	1.83
7.92	−7.20	−2.42	6.33	2.85
8.99	−7.33	−2.72	6.27	3.69
10.00	−7.45	−2.99	6.24	4.40
11.01	−7.57	−3.24	6.24	5.04
12.08	−7.69	−3.49	6.27	5.61
13.27	−7.81	−3.74	6.33	6.13
14.64	−7.94	−4.01	6.43	6.56
16.25	−8.08	−4.30	6.58	6.81
18.16	−8.20	−4.59	6.80	6.74
20.43	−8.26	−4.87	7.05	6.10
23.12	−8.17	−5.14	7.24	4.53
26.29	−7.71	−5.39	7.12	1.49
30.00	−6.48	−5.64	6.06	−3.73

Table A10. Incremental Force and Moment Coefficients per Degree of Deflection of All-Movable Rudder

α, deg	$C_{X_{\lvert\delta_r\rvert}}$	$C_{Y_{\delta_r}}$	$C_{l_{\delta_r}}$	$C_{n_{\delta_r}}$
−10.00	-6.00×10^{-4}	1.90×10^{-3}	2.19×10^{-4}	-1.27×10^{-3}
−6.29	↓	↓	↓	↓
−3.12	↓	↓	↓	↓
−0.43	↓	↓	↓	↓
1.84	↓	↓	↓	↓
3.75	−6.12	1.97	2.39	−1.28
5.36	−6.23	2.06	2.70	−1.31
6.73	−6.35	2.15	3.01	−1.34
7.92	−6.50	2.24	3.30	−1.37
8.99	−6.67	2.32	3.55	−1.39
10.00	−6.87	2.40	3.79	−1.42
11.01	−7.10	2.48	4.01	−1.44
12.08	−7.38	2.56	4.23	−1.46
13.27	−7.73	2.66	4.44	−1.49
14.64	−8.16	2.76	4.64	−1.51
16.25	−8.68	2.88	4.84	−1.53
18.16	−9.25	2.99	5.02	−1.54
20.43	−9.71	3.10	5.25	−1.55
23.12	−9.65	3.16	5.66	−1.54
26.29	−8.11	3.11	6.71	−1.51
30.00	−3.06	2.85	9.46	−1.48

Table A11. Dynamic Derivatives

α, deg	C_{m_q}, per rad/sec	C_{n_p}, per rad/sec	C_{l_p}, per rad/sec	C_{n_r}, per rad/sec	C_{l_r}, per rad/sec
0	-2.03×10^{-1}	3.81×10^{-1}	-4.98×10^{-1}	-7.94×10^{-1}	4.96×10^{-1}
5	−1.58	3.53	−6.00	−8.37	5.98
10	−1.16	2.19	−3.98	−9.21	8.40
12	−1.76	2.44	−5.79	−9.22	8.06
14	−1.76	1.79	−4.25	−8.67	6.86
16	−1.75	1.67	−4.99	−9.22	5.72
18	−1.74	2.01	−6.49	−9.46	6.03
20	−2.52	2.22	−6.19	−10.07	8.99
22	−2.99	3.07	−8.10	−10.90	9.57
25	−5.71	3.79	−8.72	−12.86	13.57
30	−8.00	8.50	−24.10	−20.41	44.90

Table A12. Incremental X Body Axis Force Coefficient Due to Deflection of Landing Gear

α, deg	$C_{X,\delta_{lg}}$ for landing-gear position, deg, of—							
	0	1	4	10	23	53	83	98
−10	0	-0.14×10^{-2}	-0.46×10^{-2}	-0.75×10^{-2}	-1.21×10^{-2}	-1.84×10^{-2}	-2.36×10^{-2}	-2.65×10^{-2}
−5	↓	−0.12	−0.41	−0.67	−1.09	−1.66	−2.12	−2.38
0	↓	−0.11	−0.35	−0.58	−0.93	−1.42	−1.82	−2.04
5	↓	−0.10	−0.32	−0.52	−0.84	−1.28	−1.64	−1.84
10	↓	−0.09	−0.31	−0.50	−0.81	−1.23	−1.58	−1.77
15	↓	↓	−0.32	−0.51	−0.83	−1.26	−1.62	−1.82
20	↓	↓	−0.31	−0.51	−0.83	−1.26	−1.61	−1.81
25	↓	↓	−0.31	−0.51	−0.82	−1.24	−1.59	−1.79

Table A13. Incremental Pitching-Moment Coefficient Due to Deflection of Landing Gear

α, deg	$C_{m,\delta_{lg}}$ for landing-gear position, deg, of—							
	0	1	4	10	23	53	83	98
−10	0	-0.34×10^{-3}	-1.14×10^{-3}	-1.86×10^{-3}	-3.00×10^{-3}	-4.56×10^{-3}	-5.84×10^{-3}	-6.56×10^{-3}
−5	↓	−0.31	−1.06	−1.72	−2.77	−4.23	−5.42	−6.07
0	↓	−0.30	−1.00	−1.63	−2.63	−4.00	−5.13	−5.76
5	↓	−0.31	−1.04	−1.69	−2.73	−4.16	−5.33	−5.99
10	↓	−0.34	−1.14	−1.86	−3.00	−4.57	−5.86	−6.57
15	↓	−0.36	−1.19	−1.93	−3.12	−4.74	−6.07	−6.82
20	↓	−0.26	−0.89	−1.43	−2.32	−3.52	−4.52	−5.06
25	↓	−0.10	−0.33	−0.53	−0.86	−1.32	−1.69	−1.89

Table A14. Incremental Z Body Axis Force Coefficient Due to Deflection of Landing Gear

α, deg	$C_{Z,\delta_{lg}}$ for landing-gear position, deg, of—							
	0	1	4	10	23	53	83	98
−10	0	-0.57×10^{-3}	-1.90×10^{-3}	-3.08×10^{-3}	-4.99×10^{-3}	-7.60×10^{-3}	-9.74×10^{-3}	-10.93×10^{-3}
−5	↓	−0.41	−1.37	−2.22	−3.58	−5.46	−6.99	−7.84
0	↓	−0.28	−0.91	−1.47	−2.39	−3.64	−4.66	−5.23
5	↓	−0.17	−0.58	−0.94	−1.52	−2.31	−2.97	−3.33
10	↓	−0.10	−0.34	−0.56	−0.90	−1.36	−1.75	−1.96
15	↓	−0.03	−0.12	−0.19	−0.31	−0.47	−0.61	−0.68
20	↓	0.02	0.07	0.11	0.19	0.28	0.37	0.40
25	↓	−0.01	−0.02	−0.03	−0.05	−0.08	−0.10	−0.11

Table A15. Incremental X Body Axis Force Coefficient Due to Ground Effect

α, deg	$C_{X,GE}$ for normalized altitude, h/b, of—							
	0.025	0.05	0.1	0.2	0.25	0.5	1	1.5
−4	-3.62×10^{-2}	-3.25×10^{-2}	-2.42×10^{-2}	-1.26×10^{-2}	-0.72×10^{-2}	-0.41×10^{-2}	-0.09×10^{-2}	0
0	−3.89	−3.50	−2.71	−1.58	−1.02	−0.52	↓	↓
4	−3.31	−2.81	−2.10	−1.20	−0.75	−0.55	↓	↓
8	−1.09	−1.07	−1.00	−0.74	−0.51	−0.46	↓	↓
12	0.13	−0.08	−0.20	−0.27	−0.26	−0.33	−0.07	↓
16	2.09	1.28	0.33	−0.06	−0.05	0.04	−0.08	↓
20	0.24	−0.06	0.02	−0.11	0.34	0.34	−0.08	↓

Table A16. Incremental Pitching-Moment Coefficient Due to Ground Effect

α, deg	$C_{m,GE}$ for normalized altitude, h/b, of—							
	0.025	0.05	0.1	0.2	0.25	0.5	1	1.5
−4	2.07×10^{-1}	1.78×10^{-1}	1.31×10^{-1}	0.69×10^{-1}	0.36×10^{-1}	0.11×10^{-1}	0.07×10^{-1}	0
0	1.80	1.56	1.18	0.61	0.30	0.11	0.07	↓
4	1.56	1.35	0.97	0.48	0.21	0.05	0.03	↓
8	1.13	0.92	0.65	0.31	0.15	0.05	0.03	↓
12	0.54	0.44	0.30	0.14	0.10	0.05	0.03	↓
16	−0.47	−0.30	−0.17	−0.07	−0.06	0.00	0.00	↓
20	−1.23	−0.91	−0.53	−0.24	−0.14	−0.03	0.00	↓

Table A17. Incremental Z Body Axis Force Coefficient Due to Ground Effect

α, deg	$C_{Z,GE}$ for normalized altitude, h/b, of—							
	0.025	0.05	0.1	0.2	0.25	0.5	1	1.5
−4	2.96×10^{-1}	2.56×10^{-1}	1.98×10^{-1}	1.07×10^{-1}	0.63×10^{-1}	0.29×10^{-1}	0.06×10^{-1}	0
0	1.95	1.67	1.16	0.57	0.32	0.14	0.02	↓
4	0.87	0.62	0.41	0.21	0.14	0.04	0.00	↓
8	−0.69	−0.53	−0.28	−0.10	−0.10	−0.05	0.00	↓
12	−1.63	−1.30	−0.85	−0.38	−0.19	−0.10	−0.01	↓
16	−2.62	−2.11	−1.39	−0.65	−0.41	−0.23	−0.02	↓
20	−3.01	−2.42	−1.64	−0.81	−0.50	−0.30	−0.03	↓

REPORT DOCUMENTATION PAGE

Form Approved
OMB No. 0704-0188

Public reporting burden for this collection of information is estimated to average 1 hour per response, including the time for reviewing instructions, searching existing data sources, gathering and maintaining the data needed, and completing and reviewing the collection of information. Send comments regarding this burden estimate or any other aspect of this collection of information, including suggestions for reducing this burden, to Washington Headquarters Services, Directorate for Information Operations and Reports, 1215 Jefferson Davis Highway, Suite 1204, Arlington, VA 22202-4302, and to the Office of Management and Budget, Paperwork Reduction Project (0704-0188), Washington, DC 20503.

1. AGENCY USE ONLY *(Leave blank)*

2. REPORT DATE
August 1992

3. REPORT TYPE AND DATES COVERED
Technical Memorandum

4. TITLE AND SUBTITLE
Preliminary Subsonic Aerodynamic Model for Simulation Studies of the HL-20 Lifting Body

5. FUNDING NUMBERS
WU 505-64-40-01

6. AUTHOR(S)
E. Bruce Jackson and Christopher I. Cruz

7. PERFORMING ORGANIZATION NAME(S) AND ADDRESS(ES)
NASA Langley Research Center
Hampton, VA 23681-0001

8. PERFORMING ORGANIZATION REPORT NUMBER
L-16956

9. SPONSORING/MONITORING AGENCY NAME(S) AND ADDRESS(ES)
National Aeronautics and Space Administration
Washington, DC 20546-0001

10. SPONSORING/MONITORING AGENCY REPORT NUMBER
NASA TM-4302

11. SUPPLEMENTARY NOTES

12a. DISTRIBUTION/AVAILABILITY STATEMENT
Unclassified–Unlimited

Subject Category 08

12b. DISTRIBUTION CODE

13. ABSTRACT *(Maximum 200 words)*

A nonlinear, six-degree-of-freedom aerodynamic model for an early version of the HL-20 lifting body is described and compared with wind tunnel data upon which it is based. Polynomial functions describing most of the aerodynamic parameters are given and tables of these functions are presented. Techniques used to arrive at these functions are described. Basic aerodynamic coefficients were modeled as functions of angles of attack and sideslip. Vehicle lateral symmetry was assumed. Compressibility (Mach) effects were ignored. Control-surface effectiveness was assumed to vary linearly with angle of deflection and was assumed to be invariant with angle of sideslip. Dynamic derivatives were obtained from predictive aerodynamic codes. Landing-gear and ground effects were scaled from Space Shuttle data. The model described is provided to support pilot-in-the-loop simulation studies of the HL-20. By providing the data in tabular format, the model is suitable for the data interpolation architecture of many existing engineering simulation facilities. Because of the preliminary nature of the data, however, this model is not recommended for study of absolute performance of the HL-20.

14. SUBJECT TERMS
Lifting body; Flight control; Landing and approach; Lift-to-drag ratio; Flight dynamics

15. NUMBER OF PAGES
66

16. PRICE CODE
A04

17. SECURITY CLASSIFICATION OF REPORT
Unclassified

18. SECURITY CLASSIFICATION OF THIS PAGE
Unclassified

19. SECURITY CLASSIFICATION OF ABSTRACT

20. LIMITATION OF ABSTRACT